UNIVERSITY OF CASSINO
AND SOUTHERN LAZIO

Ph.D. in Methods, models and technologies for engineering

Curriculum: Mechanical Engineering

XXXII Cycle

Experimental Assessment of a Prototype Hollow Cone Spray Diesel Injector by Means of Spray and Engine Characterization

SSD: ING-IND/08

Coordinator
Chiar.mo Prof. Wilma Polini

Ph.D. Candidate
Roberto Ianniello

Supervisor
Chiar.mo Prof. Gustavo Fontana

Co-supervisor
Dr. Ing. Carlo Beatrice
Dr. Ing. Gabriele Di Blasio
Dr. Luigi Allocca

ABSTRACT

To my family

ACKNOWLEDGMENTS

I want to express my gratitude to several people that have provided me with immense support throughout this project. I would like to thank my supervisors Dr. Carlo Beatrice, and Dr. Luigi Allocca, they gave me the opportunity to conduct my research at Istituto Motori under his guidance and supervision, I am thankful for the opportunity to work on very interesting research projects in the field of advanced combustion engines. I am particularly thankful for their guidance and help for the past three years to Dr. Gabriele Di Blasio and Dr. Maurizio Lazzaro, especially for his discussions and support during the experiment activities and for all hours spent with me during all Ph.D. studies. Also, I would like to thank Professor Gustavo Fontana and Professor Enzo Galloni at Cassino University for the help and useful discussions related to the thermodynamic and combustion engines.

I would also like to thank all fellow colleagues at Istituto Motori, in particular, Alessandro Montanaro and Daniele Piazzullo.

A debt of gratitude is owed by the Istituto Motori technicians: A. Schiavone, R. Maniscalco, and A. Piccolo that supported the research activities with the installation of the mechanical and electronic systems.

Most importantly, I wish to extend thanks to my parents and my sister, for their love and continued the support throughout all my life and for encouraging me to follow my dream. Special thanks to Albino for all his support and comprehension. I thank Federica for her love, patience, understanding, and for putting up with me during this research.

The activities reported in the present thesis were performed in the framework of the MIUR project PON01_2238

ABSTRACT

The application of more efficient combustion concepts requires the advancement of fuel injection technologies. The injector nozzle is the most critical component of the whole injection system for its impact on the combustion process. It is characterized by the number of holes, diameter, internal shape, and opening angle. The reduction of the nozzle hole diameter seems the simplest way to promote the atomization process, but consequently, the number of holes should increase to keep constant the injected fuel mass. This logic has been applied to the development of a new generation injector. First, the tendency to increase the nozzle number and to reduce the diameter has led to the replacement of the nozzle with a circular plate. The vertical movement of the needle generates an annulus area for the fuel delivery on 360 degrees, so controlling the atomization as a function of the vertical plate position, capable of generating a hollow cone spray. Second, on the base of the obtained results, different configurations were introduced. These new configurations are characterized by a hybrid fuel injection concept, composed of preferential fuel jets, generated via a specific design of the internal nozzle geometry, and additional circle-shaped fuel injection, to use the air between the jets. An additional hollow cone nozzle injector was designed, characterized by a higher spray cone angle with respect to the first prototype.

The experimental investigation of all new configurations has been performed on a combustion vessel, to characterize the spray evolution in a quiescent ambient in engine-like conditions by means of optical diagnostic techniques, and on a single-cylinder engine to assess the injectors performances by varying the main control parameters (electrical command, nozzle tip protrusion, test point, and calibration parameters). A more in-depth investigation of the injector characteristics in different conditions has also been performed thanks to the hydraulic characterization on the hollow cone nozzle prototype. On the base of optical and fluid dynamic diagnostics, a CFD code was also validated in evaporative and non-evaporative conditions.

The optical analysis showed a high spray evaporation rate, and the aspect also emerged in the engine results. The hydraulic characterization by Bosch tube meter highlighted a high flow rate with small needle lift and reduced hydraulic delay, compared to conventional multi-hole. The numerical simulation allowed pointing out

a rapid breakup process immediately for the HCN injector. In general, the latest versions of hybrid injectors have achieved quite similar performances, in terms of spray penetration, compared to the conventional multi-hole nozzle, while guaranteeing a different fuel distribution.

Based on the engine results, the HCN multi-jets versions guarantee better performance in comparison to the HCN old version, but it has not yet reached a level as to be considered a valid alternative to MHN. The hybrid version of HCN, thanks to the increase of the number of jets, has the potential to improve the overall spray-combustion chamber interaction further and then the engine performance.

TABLE OF CONTENTS

ABSTRACT I
List of Publications VI
List of Figures VIII
List of Tables XV
Abbreviations XVI
INTRODUCTION 1
References 6
CHAPTER 1 Compression-Ignition Engine 7
1.1 Combustion-Engine Challenges 7
1.2 Conventional Diesel Combustion (CDC) 9
1.3 Low-Temperature Combustion (LTC) 11
1.3.1 Homogeneous Charge Compression Ignition (HCCI) 12
1.3.2 Reactivity Controlled Compression Ignition (RCCI) 12
1.3.3 Partially Premixed Combustion (PPC) 13
1.4 Emissions after-treatment vs. combustion concept 13
1.5 Injection System 14
1.5.1 Common-Rail Injection System 14
1.5.2 Injectors 16
1.5.3 Fuel Injector Technology 16
References 22
CHAPTER 2 Spray characteristics 25
2.1 Background 25
2.2 Spray Structure 26
2.2.1 Atomization Process 26
2.3 Cavitation 27
2.4 Measurement Parameters 28
2.5 Structure of Engine Spray 29
2.5.1 Full-Cone Spray 30
2.5.2 Hollow-Cone Spray 31
2.6 Spray Imaging Methods 32

2.6.1 Direct imaging method 32
2.6.2 Laser Absorption Scattering (LAS) Technique 33
2.6.3 Schlieren technique 36
References 40
CHAPTER 3 Experimental Setup 42
3.1 The prototype injectors 43
3.2 Spray characterization 45
3.3 Hydraulic Characterization 49
3.4 Single Cylinder Research Engine 51
3.4.1 Heat Release Analysis, efficiency, and energy balance. 53
3.4.2 Emissions Measurement System 55
3.5 Fuels 56
References 57
CHAPTER 4 Digital image processing 59
4.1 Software for digital image processing 60
4.2 State of the art 60
4.3 Segmentation model 62
4.3.1 Curvature and Total Variation Filters 62
4.3.2 Image Processing 63
References 86
CHAPTER 5 Hollow-Cone Nozzles Characterization 89
5.1 Introduction 89
5.2 Hydraulic characterization HCN 90
5.2.1 Supply Voltage Effect 91
5.2.2 Injection Rate Measurements 92
5.3 Spray Characterization 95
5.3.1 Voltage command effect 97
5.3.2 Nozzle Deterioration Effect 104
5.3.3 Injection Parameters Effect 106
5.4 Experimental and Numerical Comparison 115
5.4.1 The code 115
5.4.2 Numerical Results 117
5.5 HCN vs. MHN 122
References 125
CHAPTER 6 Engine Results 128
6.1 The first prototype “HCN” 128

6.2 Test methodology 131
6.3 Injection parameters analysis 136
6.4 HCN-J vs. MHN 139
6.5 Start of Injection 144
6.6 Rail pressure 147
6.7 Medium load analysis 152
References 155
CONCLUSIONS 156

LIST OF PUBLICATIONS

- *"Balancing Hydraulic Flow and Fuel Injection Parameters for Low Emission and High-Efficiency Automotive Diesel Engines"*
  Author(s): G. Di Blasio, C. Beatrice, R. Ianniello, F. C. Pesce, A. Vassallo, G. Belgiorno, G. Avolio
  Affiliated: Istituto Motori CNR, General Motors, Continental
  Event: 14th International Conference on Engines & Vehicles
- *"Key Fuel Injection System Features for Efficiency Improvement in Future Diesel Passenger Cars"*
  Author(s): G. Di Blasio, C. Beatrice, R. Ianniello, F. C. Pesce, A. Vassallo, G. Avolio
  Affiliated: Istituto Motori CNR, General Motors GPS - Torino, GM Global Propulsion Systems, Continental Corp
  Event: WCX SAE World Congress Experience 2019
- *"Combustion and Emission Characteristics of a Compression Ignition Engine Fuelled with Diesel-LPG Blends"*
  Author(s): R. Marialto, L. Sequino, G. Di Blasio, R. Ianniello, M. Cardone
  Affiliated: Istituto Motori CNR, Universita di Napoli
- *"Image Processing of Vaporizing GDI Sprays:a New Curvature-Based Approach"*
  Author(s): M. Lazzaro, R. Ianniello
  Affiliated: Istituto Motori CNR, Università di Cassino e del Lazio Meridionale
  Journal: Measurement Science and Technology, MST-105979.
- *"Numerical Analyses of Spray Development and Combustion Process with Diesel-Gasoline-Ethanol Mixtures in Compression-Ignition Engines"*
  Author(s): G. Fontana, E. Galloni, R. Ianniello, D. Lanni, C. Beatrice, G. Di Biasio
  Affiliated: Istituto Motori CNR, Università di Cassino e del Lazio Meridionale
  Event: AIP Conference Proceedings December 2019 2191.

- *"Outward-Opening Hollow-Cone Spray Characterization by Experimental and Numerical Approach in Evaporative and Non-Evaporative Conditions"*
  Author(s): A. Montanaro, M. Migliaccio, L. Allocca, C. Beatrice, V. Fraioli, R. Ianniello
  Affiliated: Istituto Motori CNR, Università di Cassino e del Lazio Meridionale
  Event: 13th International Conference on Engines & Vehicles, ICE17, 2017-24-0108.
- *"Outwardly Opening Hollow-Cone Diesel Spray Characterization under Different Ambient Conditions"*
  Author(s): A. Montanaro, L. Allocca, C. Beatrice, R. Ianniello
  Affiliated: Istituto Motori CNR, Università di Cassino e del Lazio Meridionale
  Event: International Powertrains, Fuels & Lubricants Meeting 2018
- *"Combined Experimental and Numerical Investigation of the ECN Spray G under Different Engine-Like Conditions"*
  Author(s): D. Paredi, T. Lucchini, G. D'Errico, A. Onorati, A. Montanaro, L. Allocca, R. Ianniello
  Affiliated: Istituto Motori CNR, POLIMI,
  Event: WCX SAE World Congress Experience 2018
- *"Fuel distribution of a GDI spray impacting on a heated wall: liquid and vapour phases"*
  Author(s): A. Montanaro, L. Allocca, R. Ianniello, G. Meccariello
  Affiliated: Istituto Motori CNR, Università di Cassino e del Lazio Meridionale
  Event: ICLASS 2018, 14th Triennial International Conference on Liquid Atomization and Spray Systems, Chicago, IL, USA.
- *"Acoustic and imaging correlations of a GDI single-hole spray"*
  Author(s): A. Montanaro, L. Allocca, R. Ianniello, D. Siano, M. Panza
  Affiliated: Istituto Motori CNR, Università di Cassino e del Lazio Meridionale
  Event: ICLASS 2018, 14th Triennial International Conference on Liquid Atomization and Spray Systems, Chicago, IL, USA.

LIST OF FIGURES

Figure 1.1 - Historical evolution of European emission limits for Diesel and Gasoline engines and some US references. 7
Figure 1.2 - Main UN agreements driving the EU CO_2 emission policy. 8
Figure 1.3 - Typical heat release rate identifying different conventional diesel combustion phases [2]. 10
Figure 1.4 - Schematic of a diesel flame with temperatures and chemistry[11]. 11
Figure 1.5 - Emission formation as a function of Φ and T. Combustion paths for HCCI, PPC, and conventional diesel combustion are indicated by the blue, green, and orange lines. The increased dilution of fuel with air in HCCI and PPC gives a higher combustion-zone heat capacity. This reduces T and Φ, and the emission-formation zones can be avoided [13]. 11
Figure 1.6 - Engine combustion research concepts compared to conventional SI and DICI. Blue indicates a reactive fuel like diesel, while orange indicates a none-reactive fuel like gasoline[14]. 13
Figure 1.7 - Simplistic overview of emissions after-treatment systems versus combustion concepts. 14
Figure 1.8 – Scheme of the common rail system [16]. 15
Figure 1.9 - Solenoid injector [15]. 18
Figure 1.10 - Piezoelectric injector. (a) Main and pilot-valve stages. (b) Pilot valve at opening of the needle. (c) Pilot valve at needle closure. (d) Nozzle enlargement [35]. 20
Figure 2.1 - Illustration of the spray formation process and the different spray regions. 27
Figure 2.2 - The influence of the internal nozzle design and pressure (increasing from left to right). Adapted from [4]. 28
Figure 2.3 - Break-up of a full-cone diesel spray. [9]. 30
Figure 2.4 - Spray development during injection (Stegemann J, Seebode J, Baltes J, Baumgarten C, Merker GP, 2002 [26]), P_{rail} = 70 MPa, P_{back} = 5 Mpa, Tair = 890 K . [9]. 31
Figure 2.5 - Mechanism of a primary breakup for a full-cone diesel spray. [9]. 31

Figure 2.6 - Hollow-cone diesel spray. Example: outward opening nozzle. [9]. 32
Figure 2.7 - Optical set-up for direct imaging of spray [10]..... 32
Figure 2.8 - Principle of LAS Technique. 33
Figure 2.9 - Extinction Images of p-Xylene Non-Evaporating Spray at Two Wavelengths λT: =532nm and λA=266nm. (Z is the axial distance from the nozzle tip) [12] 34
Figure 2.10 - Bouguer-Lambert-Beer's Law. 35
Figure 2.11 - Schlieren system, [14]..... 37
Figure 2.12 - Basic dimensions of Schlieren system, [14] 38
Figure 2.13 - Deflection of light beams through an area of circular symmetrically distributed variation of refraction index, [14]..... 39
Figure 3.1 – Spray pattern structure comparison. 43
Figure 3.2 - Spray delivering section. 44
Figure 3.3 – Needle-lift vs. supply voltage..... 45
Figure 3.4 - Optical high-pressure test chamber. 46
Figure 3.5 - Schematic of the nozzle and fuel temperature governor. 46
Figure 3.6 - Sketch of the optical set-up at the high-temperature condition. 47
Figure 3.7 - Optical layout for the Mie scattering measurements in two different configurations a) radial, b) axial, and the corresponding acquired image. 48
Figure 3.8 - AVL Injection Gauge Rate System. 50
Figure 3.9 - Single cylinder test cell layout. 52
Figure 3.10 - Sankey diagram of mean effective pressures [12]. 54
Figure 4.1 - Top: Schlieren (a) and Mie-scattering (b) images, acquired 720µs after SOI, iso-octane (P_{inj}=20MPa, T_{fuel}=363K) injected in nitrogen (ρ_{amb}=1.12kg/m^3, T_{amb}=573K). Bottom: Schlieren (c) and Mie-Scattering (d) background images. 64
Figure 4.2 - Scattering images processing algorithm. 64
Figure 4.3 - Image processing of Mie-scattering spray images. The background-corrected image Ic is shown in the first row. The second row displays the regularized image according to the MC filter. The third and fourth raw illustrates the iterative thresholding procedure. The final step of image binarization is shown in the last row..... 66
Figure 4.4 - (Top) Threshold values and mean values of the foreground classes obtained throughout the iterative thresholding process of image $I_{c,MC}$, in Figure 4.3. (Bottom) Intensity histograms of $I_{c,MC}$ (red bars), and I_6 (grey bars). The black dotted line indicates the final threshold value. 67

Figure 4.5 - Contours of the liquid phase of the spray obtained from its Mie-Scattering image. For comparison, in picture c, the contours have been superimposed to the corresponding Schlieren image..... 68
Figure 4.6 - Schlieren images processing algorithm..... 69
Figure 4.7 - Image processing of Schlieren spray images. The background-corrected image I_c is shown in the first row. The second row displays the regularized image according to the MC filter. The curvature enhanced image is shown in the third row, while the last row shows its sum with the regularized image. 72
Figure 4.8 - Image processing of Schlieren spray images. The first two pictures illustrate the iterative thresholding of the curvature enhanced image. The final step of image binarization is shown in the last row. 73
Figure 4.9 - Threshold values and mean values of the foreground classes obtained throughout the iterative thresholding process of image $Ic, MC + Ic, \kappa iMC$ in Figure 4.7 and Figure 4.8. (Bottom) Intensity histograms of $Ic, MC + Ic, \kappa iMC$ (red bars) and I_{36} (grey bars). The black dotted line indicates the final threshold value..... 74
Figure 4.10 - Boundaries of the vapor phase of the spray obtained from its Schlieren image..... 75
Figure 4.11 - Contours of the liquid phase obtained from Mie-scattering (yellow lines) and Schlieren (red lines) imaging superimposed to their raw images. Picture d: Comparison between the contours of liquid (blue line) and vapor (red line) phase obtained by Schlieren image..... 76
Figure 4.12 - Time evolution of Schlieren and Mie-scattering spray images and the corresponding vapor and liquid contours, under the ambient conditions. The first and second column shows the contours of the vapor phase (red lines) and the liquid phase (yellow lines) superimposed to the respective Schlieren and Mie-scattering raw images. The third column shows the Mie-scattering images in false colors with the corresponding liquid phase contours. In the last column, the latter is compared with the liquid phase contours (red lines) obtained from Schlieren images. 78
Figure 4.13 - Time evolution of Schlieren and Mie-scattering spray images and the corresponding vapor and liquid contours, under the conditions ρ_{amb}=1.12 kg/m^3 and T_{amb}=573 K The first and second column shows the contours of the vapor phase (red lines) and the liquid phase (yellow lines) superimposed to the respective Schlieren and Mie-scattering raw images. The third column shows the Mie-scattering images in false colors with the corresponding liquid phase

contours. The latter are compared in the last column with the liquid phase contours (red lines) obtained from Schlieren images. 79
Figure 4.14 - Time evolution of Schlieren and Mie-scattering spray images and the corresponding vapor and liquid contours, at high-density conditions. The first and second column shows the contours of the vapor phase (red lines) and the liquid phase (yellow lines) superimposed to the respective Schlieren and Mie-scattering raw images. The third column shows the Mie-scattering images in false colors with the corresponding liquid phase contours. In the last column, the latter is compared with the liquid phase contours (red lines) obtained from Schlieren images. 80
Figure 4.15 - Vapour phase boundaries of the spray, at the high-density condition and 720μs ASOI, obtained with (bottom) and without (top) applying the additional background correction. 81
Figure 4.16 - Thresholds T_l and T_{fin} and mean values of the foreground classes $\mu_{f,l}$ and $\mu_{f,fin}$ versus the time ASOI for Mie-scattering images. 82
Figure 4.17 - Maximum axial penetration (top), spray angle (middle), and spray area (bottom) of the liquid and vapor phases of the spray. 84
Figure 5.1 - Voltage command (black) and corresponding fuel injection rate (red) at the same p_{inj} (80MPa), ET (1.5ms), and p_{back} (5MPa), at different supply voltage 150V (a) and 110V (b). 92
Figure 5.2 - Rate of injection profiles at injection pressures of 30, 80, 120, and 160 MPa; energizing time of 1.25 ms, voltage command 150 V, and back-pressure 5 MPa. 93
Figure 5.3 - Total amount of injected fuel vs. time for different injection pressures and voltage command. 94
Figure 5.4 - Example background image schlieren modified. 96
Figure 5.5 - Image processing with outlines of liquid (Mie scattering on the left) and vapor (schlieren on the right) phases. Definition of axial (a) and radial (r) penetration. 96
Figure 5.6 - Image processing with outlines of liquid phase(Mie scattering) for both injectors HCN (left), HCN-J (center), and HCN-8J (right). Definition of axial (a) and radial (r) penetration. 97
Figure 5.7 - Liquid spray evolution for both configurations frontal (left) and lateral (right), p_{inj}: 80 MPa, T_{amb}: 298 K, at different voltage command. HCN (a), HCN-J (b), and HCN-8J (c) in the only frontal configuration. 100

Figure 5.8 - Comparison of spray radial penetration (a), axial penetration (b), the penetration ratio (c), and fuel injection rate (d) at different voltage commands for HCN. P_{inj} 80 MPa; ρ 14.8 kg/m^3; T_{amb} 298 K..... 101
Figure 5.9 – Comparison of spray radial penetration (a), axial penetration (b), the penetration ratio (c) at different voltage commands for HCN-J. P_{inj} 80 MPa; ρ 14.8 kg/m^3; T_{amb} 298 K..... 102
Figure 5.10 – Progressive numbering spray plumes..... 103
Figure 5.11 - Individual jet penetration profiles comparison at different voltage commands for HCN-J. P_{inj} 80 MPa; ρ 14.8 kg/m^3; T_{amb} 298 K..... 103
Figure 5.12 – Comparison of spray radial penetration at different voltage commands for HCN-8J. P_{inj} 80 MPa; ρ 14.8 kg/m3; T_{amb} 298 K. 104
Figure 5.13 - Spray comparison in different operating conditions clean(left) and dirty (right), at p_{inj}: 80 MPa, T_{amb}: 298 K, 150 V for HCN-8J..... 105
Figure 5.14 - Comparison of spray radial penetration at operating conditions for HCN-8J. P_{inj} 80 MPa; ρ 14.8 kg/m3; T_{amb} 298 K, and 150 V. 106
Figure 5.15 - Experimental Setup. 107
Figure 5.16 - Liquid spray evolution, p_{inj}: 80 MPa, T_{amb}: 298 K, 150 V..... 108
Figure 5.17 - Effect of injection duration on axial (top) and radial (bottom) liquid penetration at an injection pressure of 80 MPa. 109
Figure 5.18 - Liquid spray sequences for two injection pressures: 80.0 (left) and 120.0 MPa (right)..... 110
Figure 5.19 - Liquid axial and radial penetration for different injection pressures. 111
Figure 5.20 - Spray sequence under evaporative conditions, liquid, and vapor detection..... 111
Figure 5.21 - Effect of ambient temperature on liquid axial (top) and radial (bottom) penetration at an injection pressure of 80.0 MPa. 113
Figure 5.22 - Evaporative (left) and non-evaporative (right) liquid spray morphology. 113
Figure 5.23 - Axial (top) and radial (bottom) penetration profiles under evaporative conditions; liquid (blue curves) and vapor (red curves). 114
Figure 5.24 - Sensitivity analysis of the effect of initial drop diameter on drop diameter reduction and liquid TP. 117
Figure 5.25 - Frontal spray evolution acquired with schlieren images (left) compared with numerical spray images (right) under non-evaporative conditions. 118
Figure 5.26 - Comparison between experimental and numerical liquid TP for both the axial and radial components under non-evaporative conditions..... 119

Figure 5.27 - Evolution of air and droplets velocity distribution in a symmetry plane under non-evaporative conditions..... 119
Figure 5.28 - Frontal liquid mass fraction evolution acquired with Mie images (left) compared with numerical spray images (right) under evaporative conditions. 120
Figure 5.29 - Comparison between experimental and numerical liquid TP for both the axial and radial components under evaporative conditions..... 121
Figure 5.30 - Frontal vapor mass fraction evolution acquired with schlieren images (left) compared with numerical spray images (right) under evaporative conditions. 122
Figure 5.31 - Comparison between experimental and numerical vapor TP for both the axial and radial components under evaporative conditions..... 122
Figure 5.32 - Computed vapor mass fraction relative to residual liquid mass fraction for the HCN and MHN during the injection event. 123
Figure 5.33 – Comparison of the radial tip between prototypes and MHN..... 124
Figure 6.1 - Comparison of In-cylinder pressure and injection energizing pattern (left), Heat Release, and Heat Release Rate (right) at 1500 rpm at 4.2 bar of IMEP and HV 122V, for both injectors [1]. 129
Figure 6.2 - Specific emissions, COV, PRR, and MBF10-90% at 1500 rpm and 4.2 bar of IMEP for MHN and HCN (old version) [1]. 129
Figure 6.3 - Images of combustion processes in the optical engine at 1500 rpm and 3.3 bar of IMEP for HCN (old version) [1]. 131
Figure 6.4 - Engine map, selected part-load test points, and operating points of a vehicle with 1490 kg of inertial mass, equipped with the multi-cylinder engine over the NEDC. 132
Figure 6.5 - Comparison of tip protrusion without washer between HCN-J and MHN. 133
Figure 6.6 - Description of the Washer Thickness (WT) and Nozzle Tip Protrusion (NTP) concepts. 134
Figure 6.7 - Soot and isfc trends varying the injection washer thickness..... 136
Figure 6.8 - Charging voltage profile function of the injection current. 137
Figure 6.9 - HRR traces for two different injections' current profile..... 138
Figure 6.10 - Soot and isfc trends varying the charging voltage. 138
Figure 6.11 - Charging voltage profile varying the high voltage (HV)..... 139
Figure 6.12 - Comparison of in-cylinder pressure, injection energizing pattern, HRR at 1500 rpm, and 2 bar BMEP, for HCN-J and MHN. 140

Figure 6.13 - Specific emissions, efficiencies, COV, PRR, and MBF10-90% at 1500 rpm and 2 bar of BMEP for HCN-J and MHN. 141
Figure 6.14 - Images of the liquid spray evolution in the optical engine for HCN-J.(1500x2, #1 Table 6.2) [5]. 142
Figure 6.15 - Images of the evolution of the luminous flame in the optical engine for MHN and HCN-J. (1500x2, #1 Table 6.2) [5]. 142
Figure 6.16 – Emissions and efficiencies trace for all the test points. 143
Figure 6.17 - SoI variation effect on in-cylinder pressure, current injection profile and HRR versus crank angle at 1500 rpm and 2 (left),5 (right) bar of BMEP, No EGR. 145
Figure 6.18 - SoI variation effect on CA90-10 at 1500 rpm, and 2 (left), 5 (right) bar of BMEP, comparing to MHN reference calibration point. 146
Figure 6.19 - SoI variation effect on specific emissions at 1500 rpm, and 2 (left), 5 (right) bar of BMEP, comparing to MHN reference calibration point. 146
Figure 6.20 - Effect of the rail pressure variation on the specific emission for the test point 1500x2, without EGR, HC 110V. 147
Figure 6.21 - Effect of the rail pressure variation on the specific emission for the test point 1500x5, without EGR, HC 110V. 149
Figure 6.22 - Effect of the rail pressure variation on the in-cylinder pressure and heat release rate at 1500x5 for both injectors (HCN-J and HCN-8J). 149
Figure 6.23 - Effect of the rail pressure variation on the specific emission for the test point 2000x2, without EGR, HC 110V. 150
Figure 6.24 - Effect of the rail pressure variation on the specific emission for the test point 2000x5, without EGR, HC 110V. 151
Figure 6.25 - Effect of the rail pressure variation on the in-cylinder pressure and heat release rate at 2.0 and 5.0 of BMEP and 2000 rpm. 152
Figure 6.26 - Particulate emissions [FSN] for the three injectors compared. 152
Figure 6.27 – In-cylinder pressure and energizing current comparison at 2500x8 for both injectors (HCN-J and HCN-8J). 153
Figure 6.28 - Emissions comparison at 2500x8. 154

LIST OF TABLES

Table 3.1 – Experimental activities for different injector prototypes. 43
Table 3.2 - Optical setup for the Mie scattering measurements in two different configurations 48
Table 3.3 - Single Cylinder engine geometrical characteristics. 52
Table 3.4 - Fuel properties [11, 14, 15]. 56
Table 5.1 – Experimental conditions. 91
Table 5.2 - Injected fuel mass [mm^3/stroke] for different injection pressures, timing, and voltage command, 150 V (a), and 110 V (b). 94
Table 5.3 -Experimental conditions HCN. 95
Table 5.4 – Experimental condition. 115
Table 5.5 - Setup of spray sub-models for spray simulation. 116
Table 6.1 -Washer thickness vs. fuel outlet area protrusion. 133
Table 6.2 - Test point and main operating parameters. 134
Table 6.3 - Selected steady-state test points and engine calibration parameters of interest (Euro 5 diesel base calibration). 135
Table 6.4 - Parameters variation ranges for all parameters investigated mode at four key points at Partial Load. 135
Table 6.5 - Constraint values on the engine operating conditions adopted during the test campaign. 136

ABBREVIATIONS

$\dot{v}$	Instantaneous Volume Fuel Rate
a	Sound Speed in the Fluid
A/F	Air-Fuel Ratio
ALMR	Adaptive Local Mesh Refinement
A_{ps}	Cross-Section Piezo-Stack Actuator
A_{pv}	Cross-Section Pilot-Valve Stem
ASOI	After Start of Injection
A_{tube}	Area of the Tube Inner Section
bmep	Brake Mean Effective Pressure
CA50	Combustion Phasing
CAD	Crank Angle
CDC	Conventional Diesel Combustion
CFD	Computational Fluid Dynamics
CI	Compress Ignition
CO	Carbon monoxide
CO_2	Carbon Dioxide
COV_{imep}	Coefficient of Variation of Imep
CR	Common Rail
CRF	Centro Ricerche Fiat
DDM	Discrete Droplet Model
DIP	Digital Image Processing
DISI	Direct Injection Spark Ignition
ECU	Electrical Control Unit
EGR	Exaust Gas Recirculation
ET	Energizing Time
FBP	Flash-Boiling Point
FIS	Fuel Injection System
GC	Gaussian Curvature
GDI	Gasoline Direct Injection

HCN	Hollow-Cone Nozzle
HCN-J	Hollow-Cone Nozzle Jets
HR	Heat Release
HRR	Heat Release Rate
HW	Hardware
IAP Injector	Indirect-Acting Piezo Injector
ID	Ignition Delay
IM	Istituto Motori
IMEP	Indicated Mean Effective Pressure
ISFC	Indicated Specific Fuel Consumption
KH-RT	Kelvin-Helmholtz and Rayleigh-Taylor
L_{abs}	Absorption of Liquid Droplet
LAS	Laser Absorption Scattering Techinique
LRT	Likelihood Ratio Test Method
L_{sca}	Scattering of Liquid Droplet
MC	Mean Curvature
MCE	Multi-Cylinder Engine
mep	Mean Effective Pressure
MHC	Methane unburned hydrocarbon
MHN	Multi-Hole Nozzle
NO_x	Nitrogen Oxides
p_{back}	Backpressure
P_{brake}	Brake Power
p_{cc}	Pressure Control Chamber
p_{dc}	Pressure Delivery Chamber
pfp	Peak Firing Pressure
$P_{frict\text{-}loss}$	Friction Power Losses
P_{ind}	Indicated Power
p_{inj}	Injection Pressure
PM	Particulate Matter
$P_{pump\text{-}loss}$	Pumping Power Losses
$p_{pv,up}$	Upstream Pressure Chamber of the Pilot-Valve
PRR_{max}	Peak Pressure Rise Rate
p_{sac}	Pressure Chamber of the Sac
$p_{sac,up}$	Upstream Pressure Chamber of the Sac

$Q_{comb\text{-}loss}$	Combustion Loss
Q_{EGR}	EGR Heat Cooling Loss
Q_{Exh}	Exhaust Heat Loss
Q_{HT}	Radiation and convection heat transfer loss
q_{inj}	Total amount of injected fuel
RoI	Rate of Injection
SCE	Single Cylinder Engine
SI	Spark Ignition
SMD	Sauter Mean Diameter
SoC	Start of Combustion
SoI	Start of Ignition
T_{amb}	Ambient Temperature
TDC	Top Dead Centre
T_{fuel}	Fuel Temperature
THC	Total Unburned Hydrocarbon
t_{inj}	Injection Duration
T_{inj}	Injector Temperature
TP	Tip Penetration
TV	Total Variation
V	Total Injected Amount
V_{abs}	Absorption of Vapor
VGT	Variable Geometry Turbine
Δp_{gauge}	Pressure Change
η_{brake}	Brake Efficiency
η_{comb}	Combustion efficiency
η_{gross}	Gross efficiency
η_{net}	Net Indicated Efficiency
$\eta_{thermal}$	Thermal Conversion Efficiency
λ	Relative Air-fuel ratio
ρ	Fluid Density
ρ_{amb}	Ambient Density
ρ_{gas}	Chamber Density
Φ	Equivalence Ratio
I_0	Intensity Incident Light
I_t	Intensity Transmitted Light

Q_{ext}	Extinction Efficiency
λ_A	Wavelength of Absorption
λ_T	Wavelength of Transmission

INTRODUCTION

Background

The most important factor affecting the development of powertrains used in road vehicles is currently the emission of harmful exhaust compounds and how these emissions can be reduced.

The second most important factor is in reducing greenhouse gas emissions, particularly CO_2 emitted by motor vehicles, which is also a political priority due to CO_2's impact on global warming.

New European emission regulations, such as Euro 6d and new test methods (RDE and WLTP), are the main challenges for the automotive industry caused by political, socioeconomic, and technical factors. Air quality is very high on the political agenda, and pressure remains to limit and reduce greenhouse gas emissions from the road transport sector. In addition to limits becoming increasingly stringent, the list of parameters subject to legal limits is slowly expanding and, most importantly, these limits must be met under a wide range of conditions. In particular, the emission limits of particulate matter and nitrogen oxides have tightened and are being treated as a form of pollution with a significant negative impact on the environment [1].

The issues of harmful emissions, especially:

a) Nitrogen oxides (NOx) from vehicles powered by compression ignition engines (CI), which for vehicles meeting Euro 3, Euro 4, Euro 5 and Euro 6b standards, proved to be significantly greater in actual conditions of road use than in homologation laboratory measurements;
b) Particulate matter (whether quantified by mass PM, or number PN) in exhaust gases, not only from vehicles with CI engines, where the introduction of DPF filters has practically resolved this problem but also from vehicles with spark-ignition engines (SI), especially ones equipped with direct gasoline injection into the combustion chamber (GDI) that produce large amounts of particles of very small diameters, so-called nanoparticles, which are very harmful to living organisms;

c) Non-exhaust particulate emissions, originating from other components such as brakes and tires, as well as volatile compounds emitted from the materials in new vehicles (Vehicle Internal Air Quality);
d) Carbon dioxide (CO_2) and fuel consumption (which is also related to the global demand for fuel, energy security and plans for a decarbonized economy [2]) occurring in real-world driving conditions,

are becoming a priority for the automotive sector, especially within the largest markets of the European Union, Japan, China, India, and other Asian countries, South Korea, Brazil and the USA [3].

The new legislation on IC engines imposes even more stringent limits on emissions and CO_2 levels. In particular, the European emissions standard Euro 6 imposes a NOx reduction of about 50% with respect to the Euro 5 standard. While, the CO_2 limit in Europe for passenger cars will be cut from the present value of 130 g/km, for the average fleet, to 95 g/km by 2021 [4] and to 70g/km by 2025 [2].

In order to respect the legislation in terms of CO_2 and emissions, the OEM companies are hard-working on the development of new powertrain concept comparison aimed at the introduction of dedicated-advanced IC engine technologies capable of improving both the efficiency and emissions performance. The key technologies are listed below and divided according to the legislative and temporal objectives:

SHORT TERM DEVELOPMENT → to meet Euro 6d limits/requirements, WLTP, and RDE rules:

- "Rightsizing" of CI and SI engines;
- Diesel engines → adding SCR to ATS to all Light Duty-Vehicles (LDV);
- Gasoline DI → adding GPF to ATS to all LDV.

LONG-TERM DEVELOPMENT → beyond Euro 6d & to meet CO_2 requirements:

- Further "rightsizing" of SI DI engines;
- Alternative fuels development (HVO, DME, Ethanol, CNG/LPG);
- CNG fuelled SI engines;
- Hybridization (MHEV, PHEV);
- HCCI engines;
- Electric powertrain (BEV);
- Fuel cells (FCEV).

A new trend in engine design is "rightsizing", as well as an ongoing convergence of spark ignition and compression ignition engine technology, with differences now much smaller than in the past (turbocharging, direct injection, compression ratio).

In this regard, this study presents the development of a novel concept for advanced piezoelectric driven fuel injectors. The development belongs to a wider collaboration project between Istituto Motori and Centro Ricerche Fiat (FCA Research Centre).

The commercial piezoelectric fuel injectors, in general, thanks to the potential offered by piezoelectric actuators such as the rate of fuel injection and the response time of the injector, contribute to the efficiency of the system as well as the improvement of the combustion. Using the piezoelectric actuator, the Electronic Control Unit can manage a high number of multiple injections within a combustion cycle, allowing very efficient combustion to occur thanks also to the reduced delay time between the electric and the hydraulic command, with respect to conventional solenoid injector. An increase in combustion efficiency leads to cleaner exhaust, lower noise levels, and higher power output, which are all critical demands for the automotive industry [5].

Motivation

Within the last decade, the high-speed direct injection (HSDI) diesel engine has become a realistic alternative to the gasoline engine for modern passenger car applications. Excellent drivability and durability, together with the high economy, have led to its increasing popularity in the market place.

European legislation is set to impose a further restriction on the level of emissions that are permitted from diesel engines together with targets for fuel-efficiency. Therefore, the stringent emission legislation placed upon the modern diesel engine poses a challenge to engine designers. To satisfy these targets, the researchers have to develop new techniques and processes that can be integrated with existing engine sub-systems to reduce pollutant output. The fuel injection equipment is one such sub-system that has been found to lend itself to developments leading to improvement in engine performance and emission-quality and will continue to play a vital role in the development of improved diesel engines for the foreseeable future.

These benefits have been achieved by more sophisticated control of the fuel injection process and the use of higher injection pressures. Ultimately the nature of the combustion process is determined by the quality of the fuel spray and its distribution and mixing within the combustion chamber. Breakup and distribution of the spray are determined mainly by the in-cylinder conditions (air motion, density, and temperature), the injection pressure, nozzle design, and geometry. A need is therefore identified to study the temporal and spatial development of diesel sprays under realistic injection and in-cylinder conditions firstly, and secondly, the effects of different

injection regimes on the combustion process. Data obtained can be used to establish a link between injection and combustion processes, and indirectly be used in the development of models to be incorporated in CFD codes.

Objectives

The objective of this project, as previously discussed, is to assess the real potentialities of the injector that uses a piezoelectric actuator to directly control the process of fuel injection in a diesel engine. The tested injectors are outwardly opening nozzle injectors able to generate a hollow cone spray, which justifies the acronym HCN. For this reason, a complete characterization of the injectors was carried out in terms of spray evolution in a vessel combustion chamber, hydraulic characterization and tests with Single-Cylinder Engine (metal and if necessary optical) in order to be able to identify the optimal configuration (shape) and evaluate the potentialities with respect to the conventional solenoid injectors.

In the following thesis, a panoramic scenario of the results for the prototypes will be presented, and subsequently, the experimental activities carried out for the new prototypes will be illustrated. These results will be compared to those of a conventional multi-hole nozzle injector, which will be considered as a reference.

Detailed analysis of the experimental results will be provided to fully characterize the performance of the injectors in order to highlight the real potentialities of the new architecture.

The thesis can be broadly divided into two main groups: spray characterization and combustion studies. Studying non-combusting sprays allows the assessment of the location of diesel liquid and vapor. This information, which is crucial for correct combustion analysis, was obtained by several optical techniques: Schlieren and Mie-Scattering. Combustion studies were focused on the investigation of the engine performance and emissions formation.

Thesis Outline

A summary of the chapters that make up the thesis is provided in this section. The first part contains background information focused on diesel engine principals and the role of fuel injectors in establishing the efficiency and performance of the engine. The dynamics/physics of the spray is described in general in Chapter 2.

Chapter 3 provides a description of the test methodology and the facilities employed to characterize the new prototypes. Section 4 describes in detail the image processing, developed during the Ph.D. program. Chapter 5 and 6 elaborate on the experiments

conducted, provides the results, as well as an analysis of the overall characteristics of the injector prototypes. Several recommendations regarding future development and activities are also offered.

REFERENCES

[1] P. Bielaczyc and J. Woodburn, 'Trends in Automotive Emission Legislation: Impact on LD Engine Development, Fuels, Lubricants and Test Methods: a Global View, with a Focus on WLTP and RDE Regulations', *Emission Control Science and Technology*, vol. 5, no. 1, pp. 86–98, 2019.

[2] S. Neugebauer, 'Technological scenarios for the decarbonization of road transport', *Proceedings "Connectivity–key to future emission and consumption reduction*, 2018.

[3] T. Kobayashi, 'Outline and issues of RDE test in Japan', in *2nd Sino-EU Workshop on New Emissions Standards for Motor Vehicles*, 2018.

[4] E. Parliament and the C. of the E. Union, 'Regulation (EU) No 333/2014 of the European Parliament and of the Council of 11 March 2014 amending Regulation (EC) No 443/2009 to define the modalities for reaching the 2020 target to reduce CO2 emissions from new passenger cars', *Off J Eur Union*, vol. 103, no. 333, pp. 15–21, 2014.

[5] H. Bauer, *Automotive handbook*. Society of Automotive Engineers, 2000.

CHAPTER 1 COMPRESSION-IGNITION ENGINE

1.1 Combustion-Engine Challenges

The internal combustion engine has revolutionized transportation since the 19th century. Today, the world's vehicle population consists of more than one billion cars, with a yearly production of 95 million, of which the vast majority is propulsed by a combustion engine [1]. The reason for its persistent popularity is a combination of simplicity, durability, low power-to-weight ratio, high power controllability, and reasonable efficiency [2]. Engine research and development are mainly focused on legislation-enforced emission reduction and the aim to reduce fuel consumption. This is due to toxic local emissions [3, 4], and the fact that the transportation sector contributes to 23 % of global greenhouse gas emissions [5]. The historical evolution for European limits for Diesel and Gasoline engines are presented in Figure 1.1

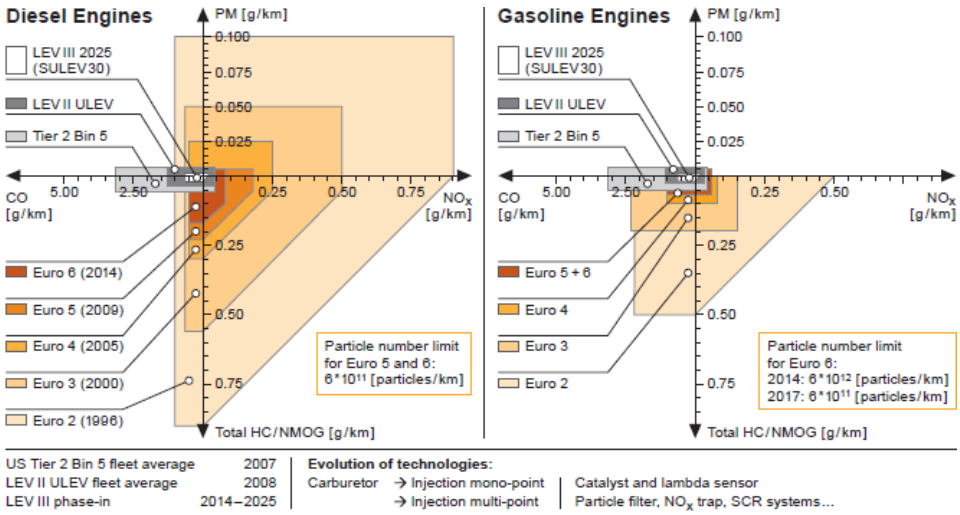

Figure 1.1 - Historical evolution of European emission limits for Diesel and Gasoline engines and some US references.

Emissions of CO, unburned hydrocarbons (HC), and particle number count are also regulated. The European Union maintains its focus on achieving the Greenhouse Gas

(GHG) emission reductions planned for the second commitment period of the Kyoto protocol for 2013 to 2020 with the target to achieve in 2020 20% of GHG reduction compared to the base year 1990. For the following years, the European Union committed within the Paris agreement (COP21) to a GHG reduction target for the period from 2021 to 2030. The commitment for 2030 is a reduction of 40% of GHG emissions compared to 1990, Figure 1.2. Finally, for 2050 the European Union set itself a target of net-zero greenhouse gas emissions.

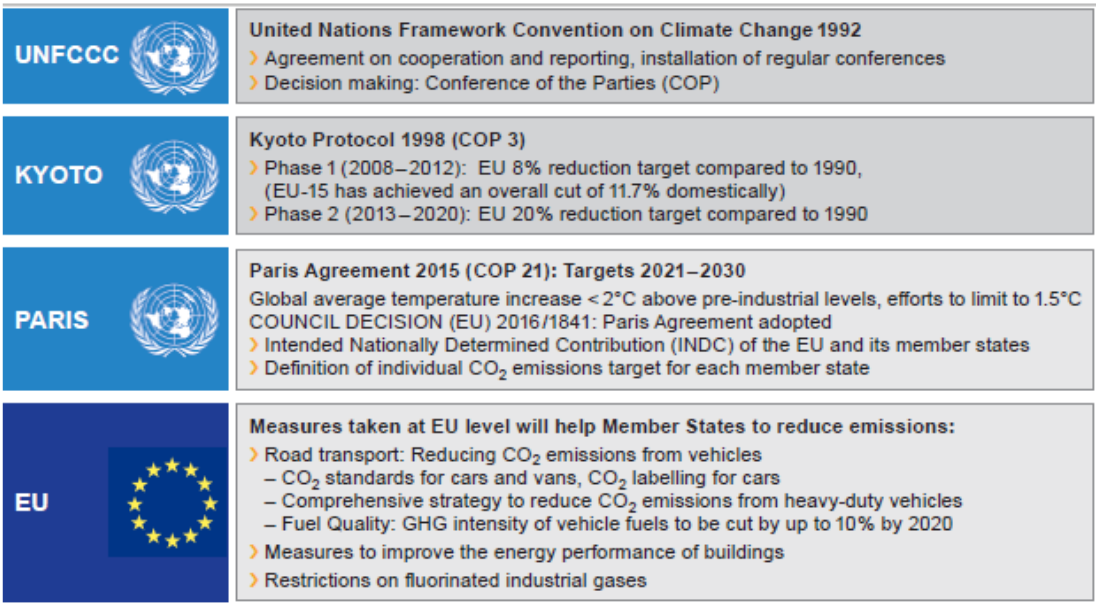

Figure 1.2 - Main UN agreements driving the EU CO_2 emission policy.

Battery-electric and fuel-cell vehicles are possible zero-emission alternatives to the internal combustion engine [6]. However, considering a large number of combustion engines on our roads today, mass production will probably continue for several years, especially in the heavy-duty sector [7]. In this scenario, technological combustion-engine advances in combination with hybridization, and the usage of biofuels could constitute a cost-effective path towards reduced local and global emissions [8, 9].

Engine-technology advances for cleaner combustion include high-pressure fuel-injection, exhaust-gas recirculation (EGR), and compression and cooling of inducted air [10]. Exhaust filters and catalysts are also necessary for the fulfillment of current legislation. The resulting engine complexity has led to an increase in the number of sensors and actuators, which has promoted the development of more advanced engine-control systems. Focus has also been directed towards the development of new, clean and efficient combustion concepts. In the current scenario, this thesis presents work

on the assessment of a new concept of injector, based on piezo-electric pintle type actuation.

This thesis investigates how the fuel injection could be used to optimize the combustion for efficient fulfillment of constraints on cylinder pressure, NOx emissions, and exhaust temperature. Such methods could also be used to improve the performance of conventional combustion concepts.

The following sections give a brief overview of fundamental engine principles and compare conventional diesel combustion with low-temperature combustion.

1.2 Conventional Diesel Combustion (CDC)

The following description of conventional diesel combustion (CDC) is based on the conceptual model presented by Dec [11]. Conventional diesel combustion is initiated by high-pressure fuel injection into a compressed, hot (~1000 K) air charge, close to TDC. The injected fuel propagates into the combustion chamber and forms a conical jet of fuel droplets.

The fuel jet becomes increasingly diluted with hot air and vaporizes as it expands. After a certain traveling distance along the jet axis (~20-25 mm), called the lift-off length, the fuel has vaporized completely. Chemical reactions are initiated all over the jet cross-section after further air entrainment. Initial reactions are followed by rapid, rich, premixed combustion, and the resulting temperature increase leads to the formation of soot due to an excess of fuel. Air entrainment continues as the reacting fuel travels along the spray axis, and a quasi-steady diffusion flame is formed along the jet periphery when stoichiometric conditions are reached. At this stage, the combustion rate is controlled by how fast the injected fuel is vaporized, mixed with air, and supplied to the diffusion flame. This type of combustion is therefore referred to as mixing control. The temperature reaches its maximum in the vicinity of the flame which causes nitrogen to oxidize and form harmful NOx emissions. The high temperature, in combination with the availability of oxygen, also results in soot oxidation, which gives the characteristic diesel-flame luminosity. Furthermore, these conditions lead to almost complete oxidation of CO and HC during the expansion stroke. Figure 1.3 shows the typical heat release rate (HRR) trace from conventional diesel combustion. The first phase, called ignition delay (ID), represents the period between the start of injection (SoI) and the start of combustion (SoC). After the ID period, a spontaneous auto-ignition process starts due to the high temperature and pressure of air-fuel mixture; this phase is called premixed combustion characterized

by very high heat release gradients [12]. After the premixed combustion phase, and during the injection process, the heat release rate is controlled by the rate at which the mixture becomes available for burning (mixing-controlled combustion phase). Finally, the heat release continues at a lower rate well into the expansion stroke (late combustion phase) [2].

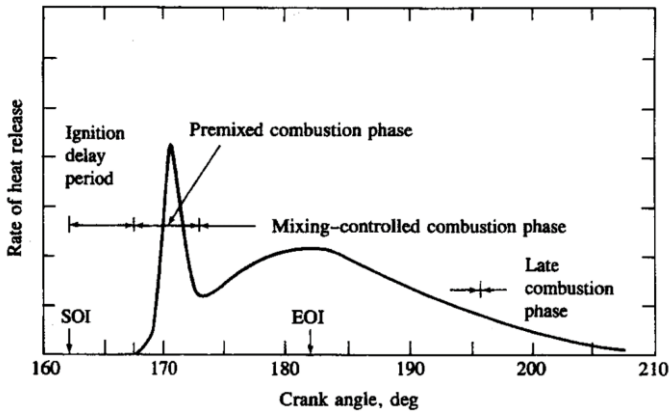

Figure 1.3 - Typical heat release rate identifying different conventional diesel combustion phases [2].

Another schematic representation of the diesel combustion was proposed by Dec [11]. The conceptual model, presented in Figure 1.4, describes the quasi-steady diesel spray; the single diesel fuel jet can be divided into several zones. On the left side, a liquid fuel penetrates in the combustion chamber from the nozzle, it mixes with the hot ambient air, and then the fuels start to vaporize, and a fuel-rich mixture zone establishes. The spray reaches its maximum liquid length. Auto-ignition occurs in the subsequent fuel-rich mixture zone, where it undergoes premixed combustion. It is pre-sources of soot formation inside the spray. Further downstream in the jet, the soot particles grow in size and concentration inside the diffusion flame due to a lack of oxygen. On the outer reaction zone of the diffusion flame, NO_X production occurs due to near stoichiometric conditions and high temperatures about 2700 K [11].

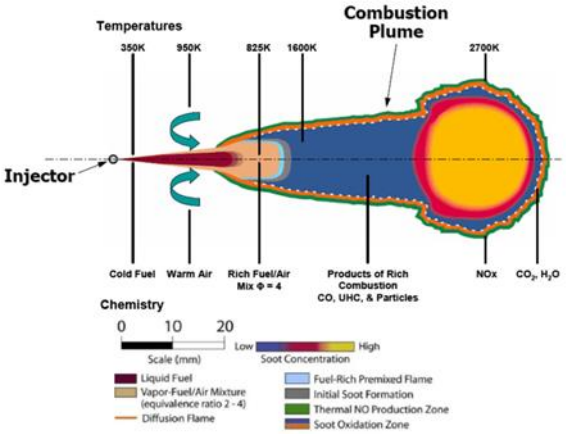

Figure 1.4 - Schematic of a diesel flame with temperatures and chemistry[11].

1.3 Low-Temperature Combustion (LTC)

Combustion concepts with improved paths have been under intense study during the past decades. Low-temperature combustion (LTC) concepts utilize enhanced fuel-air mixing to increase the combustion-zone heat capacity. The increased heat capacity lowers combustion temperatures and makes it possible to avoid the emission-formation regions in Fig. 1.6.

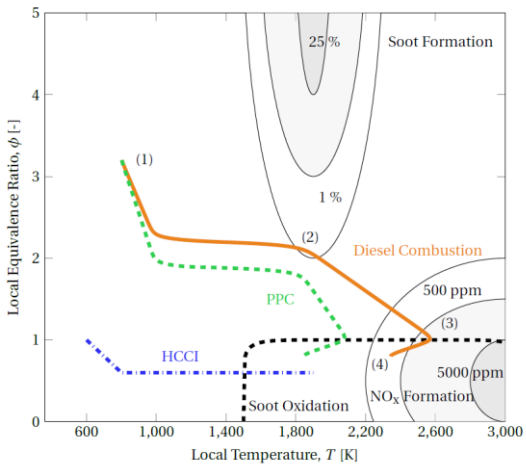

Figure 1.5 - Emission formation as a function of Φ and T. Combustion paths for HCCI, PPC, and conventional diesel combustion are indicated by the blue, green, and orange lines. The increased dilution of fuel with air in HCCI and PPC gives a higher combustion-zone heat capacity. This reduces T and Φ, and the emission-formation zones can be avoided [13].

HCCI, or ATAC as it originally was coined, was the first low-temperature combustion strategy for engines. Although HCCI has not been commercialized, it

provided extensive new insights to engine combustion that has led to the development of many other concepts. These include RCCI and PPC that are described below, but also PCCI, PPCI, GDCI, and many others that in common have low-temperature combustion and high dilution levels and, due to their similarities, are not described further. A characteristic feature of the new combustion principles is that they offer new opportunities for both existing and new alternative fuels. HCCI can be run on essentially any fuel by tailoring compression ratio and inlet temperature, RCCI uses two fuels with varying proportions while PPC runs efficiently on any liquid fuel by adjusting fuel injection and other parameters (Figure 2). PPC has also demonstrated excellent efficiency and very low emissions for naphtha, which has an octane rating of around 70, substantially a fuel with ignition properties in-between diesel and gasoline.

1.3.1 Homogeneous Charge Compression Ignition (HCCI)

The homogenous charge compression ignition (HCCI) principle is a comparatively new concept that has yet to find commercial success. The working principle is similar to that of the SI engine, in that the fuel and air are mixed before being inducted into the cylinder. The HCCI engine does not use any specific device to ignite the in-cylinder charge. Combustion starts simultaneously throughout the cylinder through auto-ignition by compressing the charge to sufficiently high pressures and temperatures. In regular operation, the HCCI engine needs dilution of the intake charge to limit the pressure rise rate during combustion. This leads to a low combustion temperature that is beneficial for efficiency and low soot and NOx emissions. The premixing and low combustion temperature do, however, lead to remarkably high emissions of CO and HC. By carefully adjusting the compression ratio and inlet temperature, almost any fuel can be used with HCCI. The challenges with controllability and low load have limited the use of HCCI to an ideal combustion research tool.

1.3.2 Reactivity Controlled Compression Ignition (RCCI)

RCCI uses two fuels with different reactivity (auto-ignition resistance) in different proportions to optimize the combustion behavior at different operating conditions. It is similar to the dual-fuel concept by using one fuel with high auto-ignition resistance premixed with air and one fuel with low auto-ignition resistance direct-injected. Unlike the dual fuel concept, RCCI uses dilution and low-temperature combustion, in a similar way to HCCI. Very high efficiencies have been reported, combined with emissions characteristics similar to HCCI.

1.3.3 Partially Premixed Combustion (PPC)

PPC can be seen as a concept combining principles from both DICI and HCCI. Typically, PPC is associated with a separation of the direct injection event and the auto-ignition combustion. By injecting the fuel at some point during the compression, combined with air dilution and high amounts of residual gases and fuel with some resistance to auto-ignition, fully premixed or fully heterogeneous conditions can be avoided. This leads to low emissions of soot, NOx, HC, and CO, together with very high efficiency. PPC exhibits substantial fuel flexibility with liquid fuels by tailoring the injection strategy towards the auto-ignition properties of the fuel. However, with low auto-ignition resistance of the fuel, sufficient premixing is challenging to achieve leading to increased emissions of soot. Gaseous fuels have not been investigated with PPC due to the anticipated difficulties associated with suitable direct injection of gas.

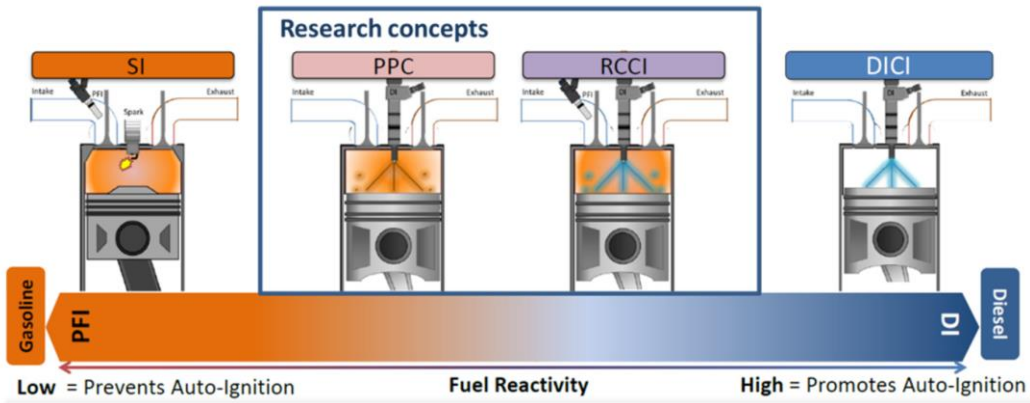

Figure 1.6 - Engine combustion research concepts compared to conventional SI and DICI. Blue indicates a reactive fuel like diesel, while orange indicates a none-reactive fuel like gasoline[14].

1.4 Emissions after-treatment vs. combustion concept

Nitrous oxides (NOx), hydrocarbons (HC), carbon monoxide (CO), and soot or particulate matter (PM) are known as regulated emissions. The emissions legislation is increasingly becoming stricter. Most markets in the world require vehicles with emissions after-treatment systems (EATS), while in the US, Europe, Japan, and some other places, the demands require advanced EATS to meet the regulations.

DICI engines emit less HC and CO but high amounts of NOx and soot. To meet the latest and strict regulations, US 10 and EURO VI for heavy-duty vehicles, such as buses and trucks, advanced and expensive EATS are required (Figure 1.7). EURO 6 for cars is not as strict and more straightforward NOx reduction and particulate filters used.

Lean burn engines may get away with only an oxidizing catalytic converter (OC or DOC) to reduce CO and HC, but in some markets, selective catalytic reduction (SCR) is needed to reduce NOx. Emerging combustion concepts, as RCCI and PPC, are designed to operate without the need for expensive EATS. RCCI may get away with only DOC, while PPC shows the overall best emissions performance. Low load CO and HC emissions are, however, still too high from PPC to be EURO VI compliant. A DOC might be needed.

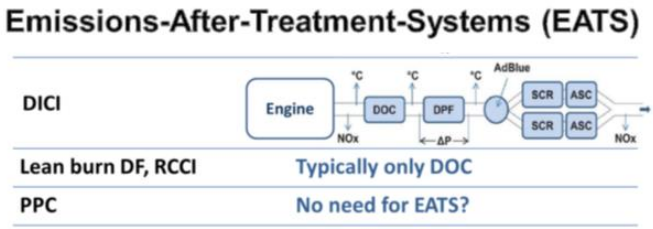

Figure 1.7 - Simplistic overview of emissions after-treatment systems versus combustion concepts.

Future regulations may prove challenging to meet for DICI engines and may require adaption of RCCI and PPC strategies.

1.5 Injection System

The injection system, as a critical component of the diesel engine, has been developed into many techniques. In particular, in the following section, it will be illustrated the standard injection system adopted in the modern CI engine. As a more advanced injecting technique, the common rail injection system can work out of the limitation of the camshaft, unlike the mechanical injection system, which involves numerous problems such as it can only make injection at certain cam angles and precise control over the injection is difficult as well. A separate electrical pump drives the common rail injection system, the pump continually works and supplies fuel at constant pressure to the common rail, an intermediate fuel reservoir. Electrical valves control injectors in the CR injection system. Such a design makes the CR injection system possible to achieve flexible injections.

1.5.1 Common-Rail Injection System

The Common Rail (CR) injection system is a state of art technology for the CI engine, and it is one of the most advanced solutions in order to optimize the combustion processes. It can provide a very flexible way of injection due to the

application of an electrical injector, as the electrical actuation valve (solenoid or piezoelectric) can activate faster and more precise than the mechanical injectors. On the other hand, the unique design of the CR system makes its fuel supply and injection sections utterly independent of each other.

Also, with various electronic sensors, the system can monitor the engine's real-time performance parameters in all loading conditions. The parameters, including RPM, cylinder pressure, temperature, fuel flow rate, etc. By sending those parameters into a microprocessor, the common rail system can adjust the injection timing, injection rate, and fuel pressure, ensuring the engine always working in the optimal condition [15].

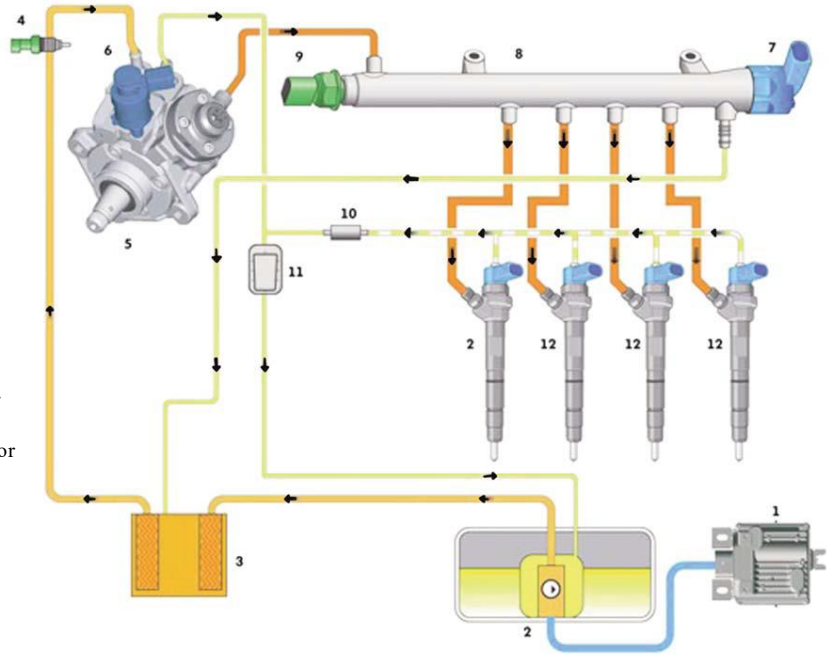

Figure 1.8 – Scheme of the common rail system [16].

A typical common rail system works as follows: a fuel supply pump firstly supplies fuel at low pressure to the high-pressure pump, from which the fuel is pressurized. Both of the fuel supply pump and the pressurized pump are electrically driven; they continuously work to transport fuel at the designed pressure to the common rail.

The common rail is an intermediate reservoir that can collect the fuel from pumps and maintain it at a high-pressure level.

Electrical-controlled Injectors in the CR system derive fuel from the rail, injecting fuel spray when they receive a command signal from the Electronic Control Unit (ECU).

The common rail injection system can control the fuel injection rate and realize flexible injection precisely. Two components are playing a crucial role in enabling this feature, which is the common rail and the solenoid injector.

1.5.2 Injectors

The injector is a complex and critical component in the injection system. It receives the high-pressure fuel from the common rail and injects the fuel through its injection holes (nozzle) into the combustion chamber. The injection holes are made very tiny to atomize the fuel into fine droplets when the fuel is penetrating the cylinder chamber.

Many variables affect the performance of fuel injectors: the start of injection, injection duration, and pressure, direction, and the number of injection jets (nozzle type). The start of injection is the point at which the injection of fuel into the combustion chamber starts. Proper timing of this point is essential and is done in degrees of crankshaft rotation relative to the crankshaft Top Dead Center (TDC). This point directly affects the emission generation. For instance, the NOx and hydrocarbon emissions are lowest when the start of injection is closest to the Top Dead Center [17].

The start-of-delivery parameter indicates the delivery of fuel from the fuel injection pump to the fuel injector. Injection lag is defined as the time from the start of fuel delivery to start of injection, and ignition lag is the time from the start of injection to start of ignition. The injection lag and ignition lag are delays that the fuel injection system has to compensate for by adjusting the start of delivery and injection in response to engine speed, load, and temperature [17].

1.5.3 Fuel Injector Technology

First and second-generation Common Rail (CR) systems have been based on solenoid-equipped injectors [18–21]. Most CR electro-injectors on the market still have a needle that is driven by solenoid coil energy. The first disadvantage of this technology is the relatively high electric power that is necessary [22], although the energy that is spent on the electric actuation of the injectors generally has a trivial impact on vehicle fuel consumption. CR systems equipped with solenoid-driven injectors also suffer from critical drawbacks concerning high-pressure capacity [23], due to the remarkable leakage of fuel that occurs through the pilot-valve. Solenoid driven injectors are above all affected by a relatively weak dynamic response [24]. The solenoid force arises at a distance, and its intensity is minimum when the air gap between the magnet and the pilot-valve armature is maximum, that is, at the start of the energizing time. Furthermore, the force on the pilot-valve increases with the square

of the current to the solenoid, and the exponential increase in the current needs about 80–100 μs before it can move the pilot-valve [22–25].

Several studies have been carried out in order to find a way of overcoming these solenoid-injector drawbacks. These studies can be subdivided into the two following main technical approaches. The first is related to the development of advanced solenoid injectors. It is possible to realize high-speed solenoids, which feature a faster dynamic response than conventional ones, by optimizing some of the magnetic and electric circuit parameters [26]. Furthermore, voltages of up to 80 V can be applied to drive the solenoid in order to obtain a sharp current rise, which in turn minimizes the needle valve opening delay [27].

The second main approach in the design of advanced CR injectors is related to the application of piezo-actuators as prime movers. The converse piezoelectric effect is used [28]. An applied electric field produces an extension of the piezoelectric material that actuates either the pilot-valve (indirect-acting piezo injectors – IAP injectors) or the needle valve directly (direct-acting piezo injectors). The main advantage of the piezo-driven injector is the enhanced dynamic response [29, 30]: a piezo-stack can generate forces of 800 N [27], while conventional solenoid systems usually show lower values than 100 N [31]. This makes it possible for the direct-acting injector concept to be also used in diesel engines [32] and, for indirect-acting injectors, makes it possible for the injected flow-rate to increase rapidly at the initial injection stage. The reduction in the Nozzle Opening Delay (NOD) of piezo driver injectors, with respect to solenoid ones, can range from 100 to 150 μs. The time required by the needle to reach the highest position from the closed state is significantly reduced (by up to 50%) compared to solenoid injectors [30, 33]. The time required to close the nozzle, that is, the Nozzle Closure Delay (NCD), is also less than that of piezo-injectors [33]: the average velocity of the needle during the down-stroke is about 0.7 m/s, whereas it reduces to 0.5 m/s in solenoid injectors.

In short, piezo-injectors seem to offer more interesting opportunities for optimizing current diesel combustion [34], and this is why they have gained so much attention in the scientific community. However, the current acting piezo and solenoid injectors do not only differ as far as the driving system of the pilot valve is concerned; they often show remarkable differences in the hydraulic layout and mechanical setup.

To better understand the real potentialities of the piezo-driver injector, in the following paragraph will describe the operating principle for both actuating systems.

1.1.1.1 Solenoid Injector

In this section, the operating principles of a typical solenoid fuel injector with a hydraulic servo-circuit that works with the common-rail system are described. Figure 1.9 shows the operation stages of the injector. The working principle of electrical injectors is depicted as follows:

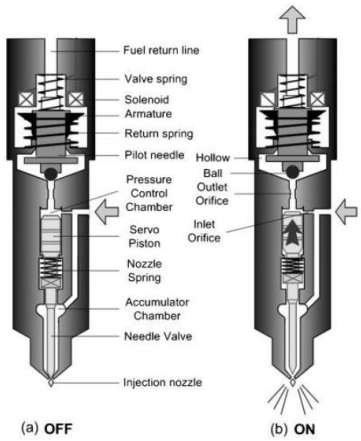

Figure 1.9 - Solenoid injector [15].

Before the solenoid is activated, the control valve is closed, fuel enters the injector through the inlet orifice, as shown in Figure 1.9a. From which the fuel flow is divided into two paths, one part of fuel stays at the pressure control chamber located at the upper end of the servo piston, another part of fuel goes down to the accumulation chamber, located in the middle of the needle valve. In this condition, the control chamber and the accumulator chamber were connected through orifices to the common rail. Because there was no pressure difference between the pressure control chamber and the accumulator chamber, while the area of servo piston is larger than the area of needle valve, the resultant hydraulic force is acting downward, closing the needle valve.

The injection process is depicted in Figure 1.9b. Feeding a command voltage to the solenoid for a given duration induced a magnetic force. Magnate force from the solenoid pulls the armature, together with the ball valve, upward. Subsequently, the pressure in the pressure control chamber decreased as fuel in the chamber drained into the fuel return line. In the meantime, the fuel pressure in the accumulation chamber remains high, thus lifting the needle valve. Consequently, fuel starts to flow through the nozzle holes.

When the injection is over, the voltage in the solenoid, together with the magnate force dissipated, the control valve closed. The fuel pressure in the pressure control chamber then increases to rail pressure again. Thus the pressure difference along with the needle valve together with the needle spring pushes the needle valve downwards, closing the valve and stop the injection process [15].

1.1.1.2 Piezo-electric Injector

The schematic of the piezo-injector is reported in Figure 1.10 and can be used to comprehend the injector operating principle. The main feature of the injector is the presence of a control chamber (Figure 1.10a), which is supplied by fuel through a calibrated hole (Z in Figure 1.10a). When the piezo-stack is not activated, the pressure value, pcc, in the control chamber approaches the rail pressure level, and the hydraulic force acting at the rear of the needle, plus the needle-spring preload, overcome the force due to the pressure p_{dc} ($\approx p_{nom}$) acting on the shoulder of the needle in the delivery chamber (Figure 1.10a) and part of the needle tip in the upstream chamber of the sac. As a result, the needle is pressed into its seat, and it seals off the passage of the high-pressure fuel to the combustion chamber via the sac. As the electric current to the injector is supplied by the electronic control unit (ECU), some of the charges are stored in the piezo-stack, and this induces the axial elongation of the piezo-material. This elongation is converted into the displacement of the pilot valve through a hydraulic amplifier. The amplification factor of the piezo-stack elongation depends on the ratio (>1) of the cross-section (A^{ps}) of the upper piston entering the amplifier (piezo-stack actuator) to the cross-section (A_{pv}) of the lower piston leaving the amplifier (pilot-valve stem). The descent of the pilot valve closes off the bypass (Figure 1.10b) and makes hole A operative (Figure 1.10) for the discharge. This connects the control chamber to the tank through a return pipe and allows the control chamber to be emptied. The pressure, p_{cc}, decreases, as does the hydraulic force, which acts at the rear of the needle. As soon as the force due to the difference between the delivery-, sac- and control-chamber pressures prevail over the needle-spring pre-load, the needle moves upwards, and some fuel is admitted, through the injection holes, into the engine cylinder. When the piezo stack is discharged, the piezo-stack actuator withdraws, the fuel pressure in the hydraulic-amplifier chamber falls, the pilot valve is forced upwards by the spring that acts on it and there is a renewed buildup of pressure in the control chamber, which is caused by the fuel flowing in from holes Z and A (Figure 1.10c). The bypass (Figure 1.10a) is in fact now open and some fuel can flow from the delivery chamber to the pilot-valve up-stream chamber and, finally, from this chamber to the

control chamber through-hole A. Therefore, unlike solenoid injectors, the A-hole in piezo-injectors can work not only as a fuel discharger but also as a fuel supplier, as the Z hole. This is why such a hole is also referred to as the A/Z orifice in the piezo-injector context. The flow throttling at the valve-seat restricted passage, which is present downstream from the bypass exit to the pilot-valve upstream chamber, was modeled through a restriction, the flow-area of which depended on the value of the pi-lot-valve lift. Nevertheless, the primary source of the flow-dissipation in the bypass is the calibrated orifice, which simulates the restriction at one of the bypass extremities.

As far as the fuel path to the engine cylinder is concerned, the nozzle-feeding pipe conveys the oil from the injector inlet to the delivery chamber. The latter is then connected to the upstream chamber of the sac through an annular passage. The needle valve lift regulates access to the sac (restriction R4 in Figure 1.10d) and to the injection holes (restriction R5 in Figure 1.10d).

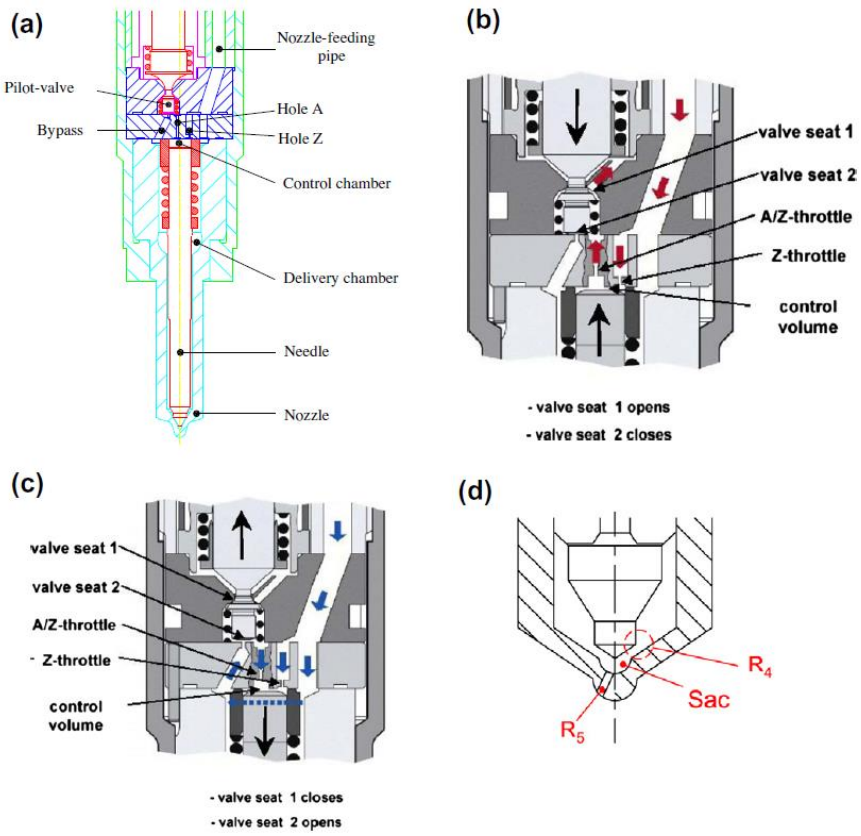

Figure 1.10 - Piezoelectric injector. (a) Main and pilot-valve stages. (b) Pilot valve at opening of the needle. (c) Pilot valve at needle closure. (d) Nozzle enlargement [35].

The mobile elements, that is, the needle- and pilot-valves, were modeled as harmonic oscillators according to mass-damper spring models: both the stiffness and damping of the basement were taken into account. The fuel pressures in the delivery chamber (p_{dc}), in the upstream chamber of the sac ($p_{sac,up}$), and the sac (p_{sac}) induce opening forces on the needle, whereas pcc gives rise to a closure force on the needle. The intensity of the hydraulic closure force on the pilot valve depends on the value of the pressure in the upstream chamber of the pilot-valve ($p_{pv,up}$). The fact that the fuel pressure acts enclosure is the reason for the reduced static leakage that is experienced through the pilot-valve when it is closed. On the other hand, the high-pressure of the fuel in most solenoid injectors tend to open the pilot valve, and static leakage therefore increases. Hence, it is the differences in the design of the hydraulics of the pilot valve that is responsible for the discrepancies that can be observed in the static leakages between solenoid and piezo injectors. The application of a pressure-balanced pilot-valve to solenoid injectors reduces their static leakages significantly [35].

REFERENCES

[1] D. Sperling and D. Gordon, *Two billion cars: driving toward sustainability*. Oxford University Press, 2010.

[2] J. B. Heywood, 'Internal combustion engine fundamentals', 1988.

[3] A. J. Haagen-Smit, 'Chemistry and physiology of Los Angeles smog', *Industrial & Engineering Chemistry*, vol. 44, no. 6, pp. 1342–1346, 1952.

[4] E. Sher, *Handbook of air pollution from internal combustion engines: pollutant formation and control*. Academic Press, 1998.

[5] C. W. Team, R. K. Pachauri, and L. Meyer, 'IPCC, 2014: climate change 2014: synthesis report. Contribution of Working Groups I', *II and III to the Fifth Assessment Report of the intergovernmental panel on Climate Change. IPCC, Geneva, Switzerland*, vol. 151, 2014.

[6] M. Contestabile, G. Offer, R. Slade, F. Jaeger, and M. Thoennes, 'Battery electric vehicles, hydrogen fuel cells and biofuels. Which will be the winner?', *Energy & Environmental Science*, vol. 4, no. 10, pp. 3754–3772, 2011.

[7] A. C. Askin, G. E. Barter, T. H. West, and D. K. Manley, 'The heavy-duty vehicle future in the United States: A parametric analysis of technology and policy tradeoffs', *Energy Policy*, vol. 81, pp. 1–13, 2015.

[8] P. Enkvist, T. Nauclér, and J. Rosander, 'A cost curve for greenhouse gas reduction', *McKinsey Quarterly*, vol. 1, p. 34, 2007.

[9] T. B. Johansson *et al.*, 'Fossilfrihet p\a a väg', *Stockholm, Sweden: Ministry of Enterprise, SOU*, vol. 2013, p. 84, 2013.

[10] W. Majewski and M. Khair, 'Diesel emissions and their control: SAE International', *ISBN-13*, pp. 978–0, 2006.

[11] J. E. Dec, 'A conceptual model of Dl Diesel combustion based on laser-sheet imaging', *SAE transactions*, pp. 1319–1348, 1997.

[12] B. Marshall, 'Diesel Fuel Injection | Howstuffworks.'

[13] S. Kook, C. Bae, P. C. Miles, D. Choi, and L. M. Pickett, 'The influence of charge dilution and injection timing on low-temperature diesel combustion and emissions', *SAE transactions*, pp. 1575–1595, 2005.

[14] S. Curran, Z. Gao, J. Szybist, and R. Wagner, 'Fuel effects on RCCI combustion: Performance and drive cycle considerations', in *presentation, CRC Workshop on advanced fuels and engine efficiency*, 2014.

[15] J. Zeng, 'Modelling and Simulation of the Diesel Engine Injection Systems', 2019.

[16] Y. Lu, C. Zhao, Z. Zuo, F. Zhang, and S. Zhang, 'Research on the common rail pressure overshoot of opposed-piston two-stroke diesel engines', *Energies*, vol. 10, no. 4, p. 571, 2017.

[17] P. Bouchilloux, R. Le Letty, N. Lhermet, G. Patient, F. Claeyssen, and M. Lang, 'Application of amplified piezoelectric actuators to the construction of gas valves', in *Smart Structures and Materials 2003: Industrial and Commercial Applications of Smart Structures Technologies*, 2003, vol. 5054, pp. 309–319.

[18] M. Miyaki, H. Fujisawa, A. Masuda, and Y. Yamamoto, 'Development of new electronically controlled fuel injection system ECD-U2 for diesel engines', SAE Technical Paper, 1991.

[19] A. Kato *et al.*, 'Influence of a fast injection rate common rail injector for the spray and combustion characteristics of diesel engine', SAE Technical Paper, 2011.

[20] G. Stumpp and M. Ricco, 'Common rail-an attractive fuel injection system for passenger car DI diesel engines', SAE Technical Paper, 1996.

[21] M. Baratta, A. E. Catania, and A. Ferrari, 'Hydraulic circuit design rules to remove the dependence of the injected fuel amount on dwell time in multijet CR systems', *Journal of fluids engineering*, vol. 130, no. 12, p. 121104, 2008.

[22] J. Lee and K. Min, 'Effects of needle response on spray characteristics in high pressure injector driven by piezo actuator for common-rail injection system', *Journal of mechanical science and technology*, vol. 19, no. 5, pp. 1194–1205, 2005.

[23] H. K. Suh, S. W. Park, and C. S. Lee, 'Effect of piezo-driven injection system on the macroscopic and microscopic atomization characteristics of diesel fuel spray', *Fuel*, vol. 86, no. 17–18, pp. 2833–2845, 2007.

[24] P. Walzer, 'Future power plants for cars', SAE Technical Paper, 2001.

[25] G. Bianchi, P. Pelloni, F. Filicori, and G. Vannini, 'Optimization of the solenoid valve behavior in common-rail injection systems', *SAE transactions*, pp. 2130–2139, 2000.

[26] H. Tomishima, T. Matsumoto, M. Oki, and K. Nagata, 'The advanced diesel common rail system for achieving a good balance between ecology and economy', SAE Technical Paper, 2008.

[27] B. Oh, S. Oh, K. Lee, and M. Sunwoo, 'Development of an injector driver for piezo actuated common rail injectors', SAE Technical Paper, 2007.

[28] C. J. Taylor and G. N. Washington, 'Comprehensive piezoceramic actuator review', in *Smart Structures and Materials 2002: Smart Structures and Integrated Systems*, 2002, vol. 4701, pp. 443–454.

[29] C. Taylor and G. Washington, 'The Application of Piezoceramic Actuation to Direct Fuel Injection', SAE Technical Paper, 2003.

[30] C. Fettes and A. Leipertz, 'Potentials of a piezo-driven passenger car common rail system to meet future emission legislations-an evaluation by means of in-cylinder analysis of injection and combustion', SAE Technical Paper, 2001.

[31] A. E. Catania, A. Ferrari, and M. Manno, 'Development and application of a complete multijet common-rail injection-system mathematical model for hydrodynamic analysis and diagnostics', *Journal of Engineering for Gas Turbines and Power*, vol. 130, no. 6, p. 062809, 2008.

[32] A. Ferrari and A. Mittica, 'FEM modeling of the piezoelectric driving system in the design of direct-acting diesel injectors', *Applied Energy*, vol. 99, pp. 471–483, 2012.

[33] K. Lee, B. Oh, and M. Sunwoo, 'Development of a Programmable Driver for Solenoid-type 2-way-valve Common-rail Injectors', in *International Pacific Conference on Automotive Engineering-IPC-13*, 2005, pp. 349–354.

[34] K. Koyanagi, H. Öing, G. Renner, and R. Maly, 'Optimizing common rail-injection by optical diagnostics in a transparent production type diesel engine', SAE Technical Paper, 1999.

[35] A. Ferrari, A. Mittica, and E. Spessa, 'Benefits of hydraulic layout over driving system in piezo-injectors and proposal of a new-concept CR injector with an integrated Minirail', *Applied energy*, vol. 103, pp. 243–255, 2013.

CHAPTER 2 SPRAY CHARACTERISTICS

This chapter provides a brief introduction to the spray formation process, with a primary focus on sprays generated using high-pressure liquid injection strategies. The modern view of the physical processes governing liquid atomization is presented, and the essential measurement parameters which are relevant for the characterization of spray systems are discussed.

2.1 Background

A spray is defined as a system containing individual liquid droplets that evolve in a surrounding gaseous medium [1]. The applications of these systems are numerous, including areas such as field treatment with pesticides within agriculture, inhalation of drugs within medical therapy, delivery of fuel for combustion purposes, spray painting [2]. The spray characteristics strived after each application depends on the specific need. For instance, the drug-carrying droplets inhaled in the treatment of asthma must be made sufficiently small to penetrate through the throat and bronchial passageways to finally deposit on the surface of the lungs, but large enough to avoid immediate expiration of the medicine. Regardless of the application, it can be stated that the efficiency of the process relies on the control of the spray formation.

The most significant application of liquid sprays, and also the area in which most research has been conducted, concerns the delivery of fuel in internal combustion (IC) engines, e.g., diesel engines. In such cases, the liquid is issued with high pressure through a narrow orifice into the combustion chamber where it, due to turbulence and instabilities, disintegrates into fine droplets which vaporize and eventually burn. This process is referred to as the atomization of the liquid. Despite decades of scientific efforts and thorough investigations, the physics governing this transition between liquid and vapor is not fully understood. One of the main reasons for this lack of understanding is due to a large number of the droplet and irregular liquid ligaments generated near the nozzle outlet, making the region almost impenetrable to light. It is problematic since the majority of diagnostic tools available for spray studies today are based on laser radiation (or non-chromatic radiation). Laser-based diagnostics are

preferable over techniques based on physical probes because of their non-intrusive nature. Furthermore, by using pulsed lasers, measurements can be performed on time scale short enough to freeze the flow of the atomizing liquid in time, which is of fundamental essence for the understanding of dynamic transient spray behavior. Some of the most commonly applied spray diagnostics will be described in the following paragraph (Spray Imaging Methods).

2.2 Spray Structure

Because of the limited knowledge of the atomization process, various views on the spray structure can be found in the literature. However, a common aspect is to divide the overall structure into two parts; the region close to the orifice and the downstream region. The former is frequently referred to like the dense spray region, while the latter is recurrently denoted the dilute spray region[1] [3]. The names stem from the fact that a dense cloud of droplets is commonly formed near the nozzle outlet, while further downstream, this cloud has dispersed and become diluted. From an engineering point of view, this classification is useful and serves its purpose. However, from an optical diagnostic point of view, this terminology may render some confusion since the dense region of some sprays can be optically dilute and vice versa. In an attempt to avoid such confusion, the terms spray formation region and spray regions will be used throughout this thesis instead. These terms aim to distinguish between optical characteristics and spray phenomena.

2.2.1 Atomization Process

Figure 2.1 illustrates the conceptual model of the spray formation used throughout this thesis. The spray production can be generalized by three steps; (1) the ejection of liquid into a gaseous medium, (2) the so-called primary breakup mechanism, which is followed by (3) the secondary breakup mechanism [1]. For high-pressure injection systems, the formation of droplets was historically explained by the presence of an intact liquid core that extended far downstream of the nozzle. In the boundary layer of the liquid core, liquid ligaments and large droplets were stripped off and sequentially broken up into finer droplets. Although the presence of an intact liquid core (at high injection pressures) is still somewhat debated, the modern view of the process is that

[1] The terms near-field region and far-field region are also frequently used.

the liquid jet undergoes atomization almost directly as it emerges from the nozzle outlet, and remains intact, at most, only a few nozzle diameters [3].

The spray formation region constitutes the initial formation of isolated liquid elements as well as their subsequent fragmentation into smaller droplets. The initial creation of liquid ligaments is thought to be initiated by deformations in the interface between the liquid core and the surrounding gas, caused by turbulence or variations in the liquid flow velocity. With time these deformations grow, eventually leading to the ejection of an isolated liquid body - the primary breakup. Collisions between these ligaments as well as coalescence (merging) may occur, but sequentially they disintegrate until stable isolated spherical droplets are formed - the secondary breakup process. The remainder (downstream region) of the spray constitutes the spray region.

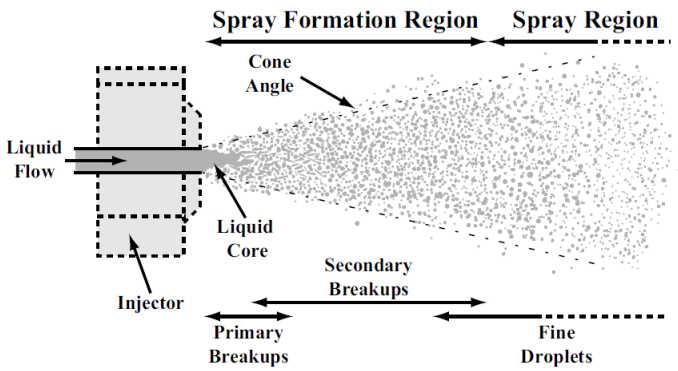

Figure 2.1 - Illustration of the spray formation process and the different spray regions.

2.3 Cavitation

One possible explanation for the onset of the disturbances causing the initial rupture of the liquid core is the creation of vapor cavities in the internal flow. This phenomenon is known as cavitation and is strongly coupled to the injection pressure and the interior design of the nozzle. The internal geometry of high-pressure cylindrical jets consists, in general, of a tube with an inner diameter D in which the fuel is delivered. The liquid is then forced through a cylindrical tube with a diameter d, where d<D, and of length L. If the transition between the pipes is sharp, the liquid will be subjected to a rapid change in pressure. Should the pressure drop below the vapor pressure of the liquid, gas will be formed. Figure 2.2 illustrates how the creation of these cavities depends on the geometrical design of the nozzle and the injection pressure. These measurements, which were performed by Hiroyasu et al.[4], cavitation was not observed for a short (L/d = 0) or rounded-inlet nozzle (Figure 2.2 a) and b)), regardless of the operating condition. Cavitation first appeared when sharp-inlet nozzles with adequately large L

were employed (dashed lines in Figure 2.2 c)). The authors further demonstrated that the extension of these cavities increased with pressure, as shown in Figure 2.2 d), leading to improved atomization. However, when the cavitating region expanded further, a significant reduction in the atomization efficiency was noted (Figure 2.2 e)). This behavior was called super-cavitation and occurred when the cavity extends over the entire inlet tube, leading to reduced wall friction and, consequently, reduced turbulence of the emerging liquid [4].

The influence of the internal geometry on atomization has spurred the development and visualization of transparent nozzles, and similar findings as those presented in Figure 2.2 can be found in the literature (see [1] and references therein). However, exactly how cavitation affects the sequential breakup process is still not fully understood, partly due to the experimental challenges associated with measurements in the spray formation region.

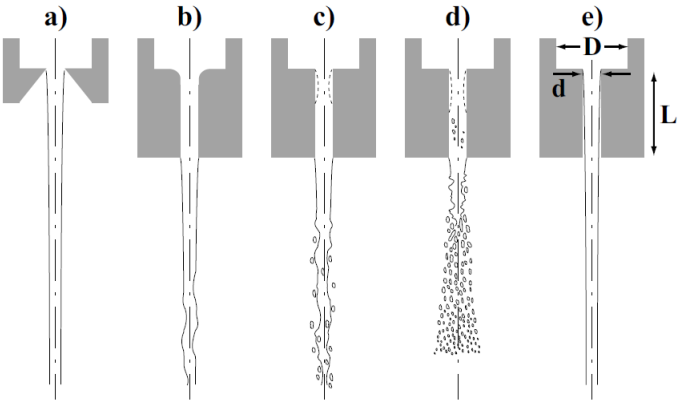

Figure 2.2 - The influence of the internal nozzle design and pressure (increasing from left to right). Adapted from [4].

2.4 Measurement Parameters

To quantify the end performance and overall effectiveness of an atomizing spray system, the most important parameters to experimentally measure are [1]:

- Droplet-size distribution
- Droplet-velocity distribution
- Droplet density (number per unit volume)
- Spatial distribution of droplets
- Droplet temperature

These, in turn, depend on a variety of factors such as injection pressure, ambient density, liquid viscosity, air motion and turbulence, the internal geometry of the

nozzle, orifice diameter, temporal profile of the pressure, etc. [3]. Various techniques to measure some of the desired parameters are provided in the following paragraphs (Spray Imaging Methods). However, it should be pointed out that only a few of these quantities can be readily accessed, even in the spray region, due to issues caused by light scattering and/or absorption. To avoid these experimental difficulties yet still be able to compare different measurement cases and operating conditions quantitatively, a common routine is to observe variations in more easily attainable spray parameters. The most common is the cone angle (Φc) and liquid penetration length (Lp).

The cone angle, also referred to as the spray angle, defines the (average) spreading of the liquid. Experimental evidence indicates that Φc is highly coupled to the injection pressure and internal design of the nozzle [5]. It should, however, be pointed out that the results obtained using different optical techniques are not always directly comparable [6].

The liquid penetration length is a measure of the distance (from the injector) the liquid-phase propagates before complete vaporization has occurred. This length is especially crucial for in-cylinder engine applications because the entrainment of air into the jet is mainly taking place during this passage. The liquid penetration length thus influences the fuel/air mixing and, consequently, the subsequent combustion. However, over-penetration leading to wall impingement is highly undesired as it can render elevated levels of unburned hydrocarbons in the exhaust gas (and, in extreme cases, wash off the lubricating oil film on the cylinder liner). It has been demonstrated experimentally that Lp is highly sensitive to the orifice diameter [7]. By decreasing the outlet dimension, the penetration of liquid reduces linearly. The determination of Lp, as well as the angle of the cone, are determined through the application of an intensity threshold on the recorded image. The main uncertainty associated with their determination concerns the choice of the threshold value, especially when the boundary between the two phases is indistinct, for this reason, code is usually implemented for processing that allows it to be determined objectively. In CHAPTER 4, the algorithm adopted will be described in detail. Also, different camera systems have different characteristics (sensitivity, resolution, gain-curves, etc.), which should be taken into account in the evaluation of them.

2.5 Structure of Engine Spray

Optical diagnostics have played an essential role in the understanding of the diesel combustion process. One example is the work performed by John Dec [8], who

gathered information by applying various laser-based techniques on a diesel spray. The investigations led to a new conceptual model for the diesel combustion process.

The main obstacle when attempting to employ laser diagnostics for the study of diesel sprays is the high concentration of droplets produced in the process, in particular near the nozzle. This makes it difficult for photons to penetrate the central region of the spray. For this reason, almost no information can be found in the literature describing the physical processes occurring in the interior of a diesel spray (core).

There are different technical methods of achieving atomization. Below, some atomization techniques will illustrate, the most used in the automotive field. Essentially, all that is needed is a force such as high pressure or an enormous shear force from the high relative velocity between the liquid to be atomized and the surrounding air or gas to overcome the surface tension of the liquid.

2.5.1 Full-Cone Spray

A schematic description of a full-cone high-pressure spray is given in Figure 2.3, [9]. The graphic shows the lower part of an injection nozzle with a needle, sac hole, and injection hole. Modern injectors for passenger cars have hole diameters of about 180 m and less, while the length of the injection holes is about 1 mm.

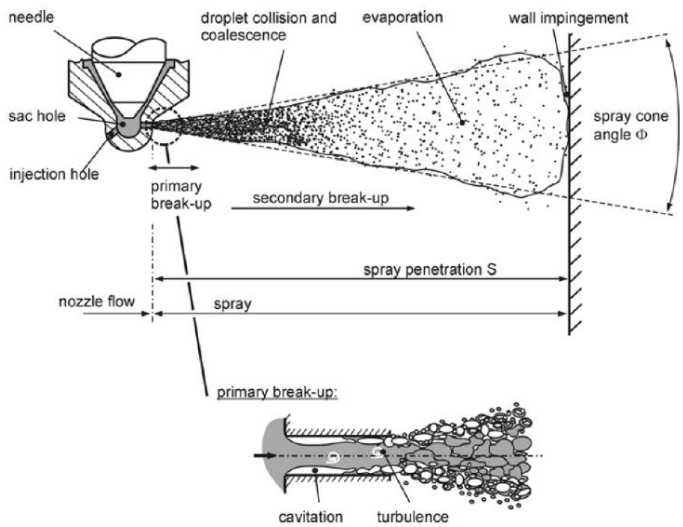

Figure 2.3 - Break-up of a full-cone diesel spray. [9]

Today, injection pressures of up to 300 MPa are used. The liquid enters the combustion chamber with velocities of 500 m/s and more, and the jet breaks up according to the mechanisms of the atomization regime. Immediately after leaving the nozzle hole, the jet starts to break up into a conical spray. This first break-up of the

liquid is called primary break-up and results in large ligaments and droplets that form the dense spray near the nozzle. In the case of high-pressure injection, cavitation, and turbulence, which are generated inside the injection holes, are the main break-up mechanisms. The subsequent break-up processes of already existing droplets into smaller ones are called secondary break-up and are due to aerodynamic forces caused by the relative velocity between droplets and surrounding gas [9].

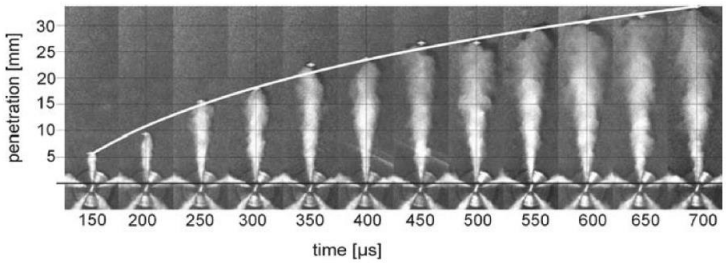

Figure 2.4 - Spray development during injection (Stegemann J, Seebode J, Baltes J, Baumgarten C, Merker GP, 2002 [26]), P_{rail} = 70 MPa, P_{back} = 5 Mpa, Tair = 890 K . [9].

In the following, the mechanisms of the primary breakup of high-pressure full-cone sprays shall be described through the figure. The primary breakup is the first disintegration of the coherent liquid into ligaments and massive drops. Figure 2.5summarizes possible break-up mechanisms.

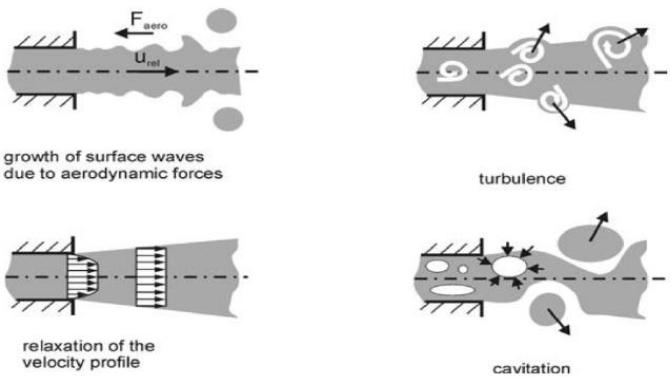

Figure 2.5 - Mechanism of a primary breakup for a full-cone diesel spray. [9].

2.5.2 Hollow-Cone Spray

To achieve maximum dispersion of the liquid at moderate injection pressures and low ambient pressures, hollow-cone sprays are usually used. Hollow-cone sprays are typically characterized by small droplet diameters, adequate fuel-air mixing, reduced penetration, and consequently high atomization efficiencies. These sprays are used in conventional gasoline engines, where the fuel is injected into the manifold, and indirect

injection, spark-ignited (DISI) engines [9]. This technique is the basis of the development of a prototype injector, developed within a project between CNR-IM and FCA research center (CRF), for CI engines. This new technology is the subject of this research project through a complete characterization in terms of spray evolution, hydraulical and engine performance, and emissions.

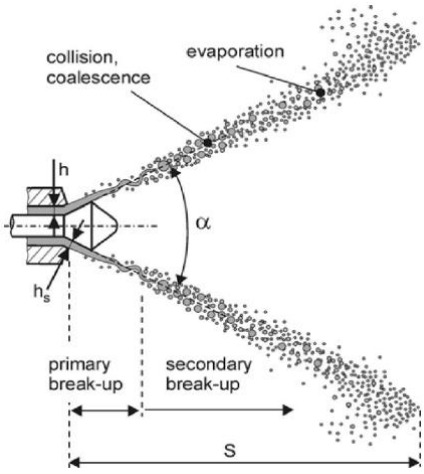

Figure 2.6 - Hollow-cone diesel spray. Example: outward opening nozzle. [9].

2.6 Spray Imaging Methods

2.6.1 Direct imaging method

Direct imaging methods [10] attempt to image droplets or particles in a plane and determine the size or other parameters by analyzing the recorded images (from photographic film or CCD camera). A laser sheet illuminates a jet of spray, and particle images are collected orthogonal to the illuminating sheet Figure 2.7. The main advantages of direct imaging methods are that they require relatively inexpensive equipment, and the optical path arrangement is easy to set-up. However, imaging methods can be problematic when analyzing dense sprays: focus issues, image overlap, and particle tracking difficulties can affect measurements, aspect already discussed before.

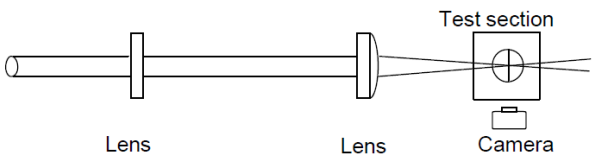

Figure 2.7 - Optical set-up for direct imaging of spray [10].

2.6.2 Laser Absorption Scattering (LAS) Technique

The dual-wavelength laser absorption scattering technique has the advantages of less sensitive to the ambient temperature in the heated-state constant volume vessel and none influence by either the water vapor or oxygen quenching. Figure 2.8 shows the principle of the LAS.

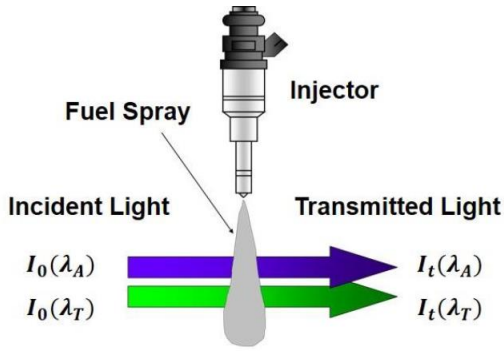

Figure 2.8 - Principle of LAS Technique.

The two wavelengths of absorption and transparent light (λ_A and λ_T) with the intensity of I_0 pass through the spray area. Due to the extinction of the liquid droplet and vapor, the intensity of those two bands become the transmitted intensity, denoted by I_T.

The extinction of the absorption wavelength, represented by $\log(I_0/I_t)_{\lambda_A}$, as described in Eq. (2.1), is attributed to the absorption of vapor $\log(I_0/I_t)_{V_{abs}}$ and liquid droplet $\log(I_0/I_t)_{L_{abs}}$, as well as the scattering of the liquid droplet $\log(I_0/I_t)_{L_{sca}}$. Likewise, the extinction of the visible wavelength, denoted by $\log(I_0/I_t)_{\lambda_T}$, only involves the scattering of the liquid droplet $\log(I_0/I_t)_{L_{abs}}$, as expressed in Eq. (2.2).

$$\log\left(\frac{I_0}{I_t}\right)_{\lambda_A} = \log\left(\frac{I_0}{I_t}\right)_{L_{sca}} + \log\left(\frac{I_0}{I_t}\right)_{L_{abs}} + \log\left(\frac{I_0}{I_t}\right)_{V_{abs}} \tag{2.1}$$

$$\log\left(\frac{I_0}{I_t}\right)_{\lambda_T} = \log\left(\frac{I_0}{I_t}\right)_{L_{sca}} \tag{2.2}$$

Due to the high-pressure direct injection, the liquid absorption of droplets is seemed so small that the second right item in Eq. (2.1) can be neglected. In consideration of the theory from Bohren [11], the limiting value of efficiency for extinction approaches to 2 if the droplet size parameter is sufficiently large, hence the scattering extinction

from a liquid droplet in both the absorption and visible wavelength are the same. To verify the deductions above, the previous study using swirl injector showed the imaging results of absorption and visible wavelength under the non-evaporating spray of p-xylene as shown in Figure 2.9. Non-evaporating spray only includes liquid droplets. At both Z=10mm and 30mm, the extinction at the visible and absorption wavelengths (λ_T=532nm and λ_A=266nm) shows the nearly same distribution and value, which means two significant facts that it is reasonable to neglect the absorption of liquid droplets in 266nm wavelength and that the droplets scattering in both two wavelengths are nearly the same.

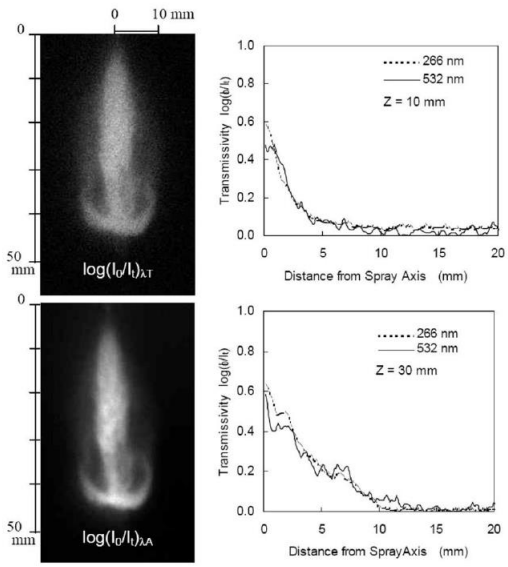

Figure 2.9 - Extinction Images of p-Xylene Non-Evaporating Spray at Two Wavelengths λ_T: =532nm and λ_A=266nm. (Z is the axial distance from the nozzle tip) [12]

Therefore, by substituting Eq. (2.2) into Eq. (2.1), the equations express the extinction of vapor, and the droplet can be shown as follow, respectively.

$$\log\left(\frac{I_0}{I_t}\right)_{V_{abs}} = \log\left(\frac{I_0}{I_t}\right)_{\lambda_A} - \log\left(\frac{I_0}{I_t}\right)_{\lambda_T} \tag{2.3}$$

$$\log\left(\frac{I_0}{I_t}\right)_{L_{sca}} = \log\left(\frac{I_0}{I_t}\right)_{\lambda_T} \tag{2.4}$$

The extinction of vapor $\log\left(I_0 / I_t\right)_{V_{abs}}$ corresponds to the light absorption theory (Lamber-Beer Law). While the extinction of liquid droplets is based on the light scattering theory (Bouguer-Lamber-Beer Law). Consequently, the fuel vapor concentration can be quantitatively calculated by this way that the extinction of the

absorption wavelength removes that of the visible wavelength. In this study, a second harmonic wavelength of 532nm (visible wavelength) and fourth harmonic wavelength of 266nm (absorption wavelength) were used as the source of the incident light to illuminate the spray in the LAS experiment.

Light Scattering Theory of Liquid Droplet

The acquisition of liquid concentration is dependent on the Law of Bouguer-Lambert-Beer. As Fig.2.9 shown, when the incident light traverses thought the field with homogenous liquid particles, the light extinction of the light path element dl can be expressed as follows.

$$\frac{dI}{I} = -\beta \cdot dl \tag{2.5}$$

Therefore, the initial intensity of incident light becomes the transmitted light with the intensity of I_t, as the light passes through the whole length l. The total extinction is described as:

$$\frac{I_t}{I_0} = \exp\left(-\int_0^\infty \beta \cdot dl\right) \tag{2.6}$$

$$\beta = \int_0^\infty R(m, D, \lambda, \theta) \cdot Q_{ext}(m, D, \lambda) \cdot \frac{\pi}{4} \cdot D^2 \cdot n \cdot f(D) \cdot dD \tag{2.7}$$

Where R is the ratio of the droplet optical thickness at the two wavelengths, θ is the half-angle corrected by the droplets scattering direction. Q_{ext} is the extinction efficiency, which is much dependent on the refractive index and size parameter. m and D are the refraction rate and diameter of the droplet, respectively. λ is the incident wavelength. n is the droplet number. Furthermore, the $f(D)$ is a distribution function of the liquid droplet.

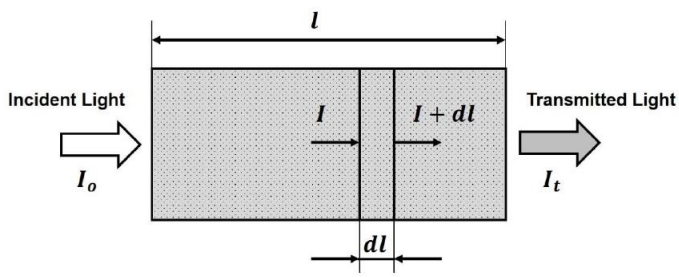

Figure 2.10 - Bouguer-Lambert-Beer's Law.

For the optical coefficient of liquid scattering R, it is determined by the correlation of the scattering light collection and optical lens. It is well known that given the

refractive index of a spherical particle, the extinction efficiency Q_{ext} can be calculated with Mie theory. The previous study has proven that regardless of the absorption, the total extinction of a cloud of particles approaches the limiting value 2 if the particles are sufficiently large [11]. Also, the fuel similar to gasoline properties, such as p-Xylene, was verified that the Q_{ext} reached 2 with the droplet size over 5μm at 266 and 532nm wavelengths [13]. For n-heptane, the size of liquid droplet mostly falls into the range of 5∼100μm, which is in agreement with the total extinction Q_{ext}=2. Therefore, the effect of the extinction error of visible and absorption wavelength on the vapor concentration measurement is limited. According to the Eqs. (2.6) and (2.7), the total extinction of scattering can be simplified as:

$$\frac{I_t}{I_0} = \exp\left[-R \cdot E_{ext} \int_0^l \int_0^\infty \frac{\pi}{4} D^2 \cdot n \cdot f(D) \cdot dD \cdot dl\right] \tag{2.8}$$

2.6.3 Schlieren technique

Schlieren techniques [14] are photographic techniques using an external light-source. The light source is, in general, just a small light point that is expanded optically to form a parallel beam through the test-section (Figure 2.11). If some object is blocking the beam as it passes through the test-section, this will create a shadow that can be recorded photographically. (This is known as the “shadow-graph” technique.)

The more advanced Schlieren techniques use some light stop placed in the focal point of a second lens. It removes the real shadow picture, but if there are some directional changes to the fight as it trav-els through the test section, the areas in which such directional changes occur will be recorded. The light will change direction whenever it passes through areas with a different light-refraction index. The differences in light- refraction index might be due to different gas density or gas-composition.

As with direct photography, the Schlieren techniques result in images of the spray. Images give an overall view of the flow-field and can be used to find regions where more detailed investigations should be performed. It is the reason why many researchers complement other techniques with Schlieren images.

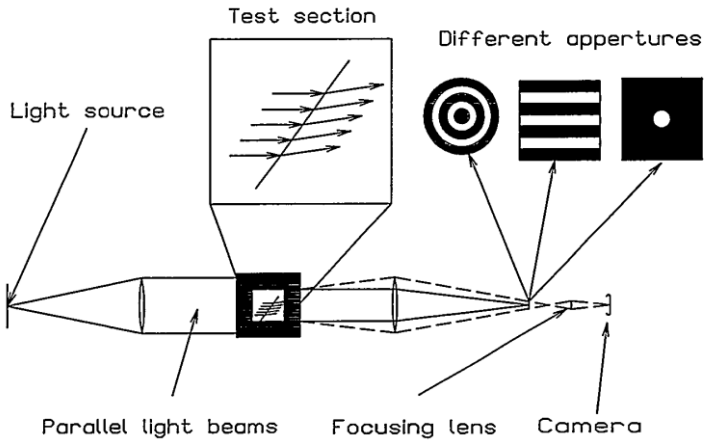

Figure 2.11 - Schlieren system, [14]

In most spray-related use of Schlieren techniques, only the outline of the spray is investigated. However, by making relatively minor adjustments to the system, it is possible to quantify some properties internal to the spray. Kamimoto [15] describes how such a system makes it possible to estimate local SMD of the droplets in a spray based on light absorption.

When using a Schlieren system for measurements internal to the spray, it is essential to remember that it is a "line of sight" averaging method. Unless it is known over what length of the light-path the deflection has been achieved, it is impossible to measure intrinsic properties. This makes it challenging to use Schlieren techniques for detailed analyses of turbulent flows.

The technique also requires optical access through the test section, which means that it is difficult to use in a research engine. However, through the use of see-through pistons and a mirror-like underside of the cylinder head, the techniques have been used even in running research engines.

Schlieren technique details

A basic Schlieren system consists of a light source with an exit diameter of the light beam D. The light is collimated by a lens L1, with a focal length of *f1*. The collimated light travels through the test section with a diameter of A and hits the second lens L2. The focal length of L2 is *f2*. This lens generates an image of the light source in its focal point; the diameter of this point is d. Any Schlieren aperture has to be located on this point. After the Schlieren aperture, the light travels through a focusing lens, L3, having a focal length *f3*. Finally, the light hits the focal plane. The diameter of the image is called a. Figure 2.12 shows the basic dimensions of the system [16].

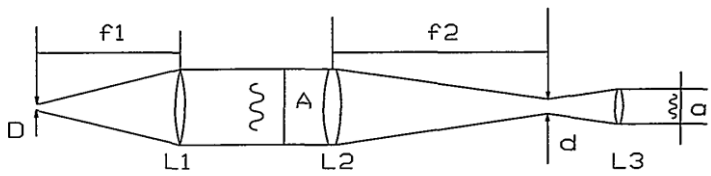

Figure 2.12 - Basic dimensions of Schlieren system, [14]

An essential property of the system is the diameter, d, of the light source image. The smaller this diameter, the more sensitive the system can be made. However, a more significant value of d can be used to increase the working range of the system. If the lenses used in the system were to be optically perfect, the light source image diameter could be calculated from:

$$d = \frac{f_2}{f_1} D \tag{1.1}$$

However, the lenses are never entirely, and there is a limit to how small values of d can be achieved.

Angular deflection of light beams

Figure 2.13 illustrates the deflection of the collimated light-beams as they travel through a test-section where the light refraction index is different from that of the surroundings. The illustration is made to clarify the phenomenon, so the deflection angle and the displacement of the light path are greatly exaggerated.

In mathematical terms, the light path can be described as follows [17] in the general three-dimensional case:

$$\begin{aligned} \frac{\partial^2 x}{\partial z^2} &= \frac{1}{n}\frac{\partial n}{dx} \\ \frac{\partial^2 y}{\partial z^2} &= \frac{1}{n}\frac{\partial n}{\partial y} \end{aligned} \tag{1.2}$$

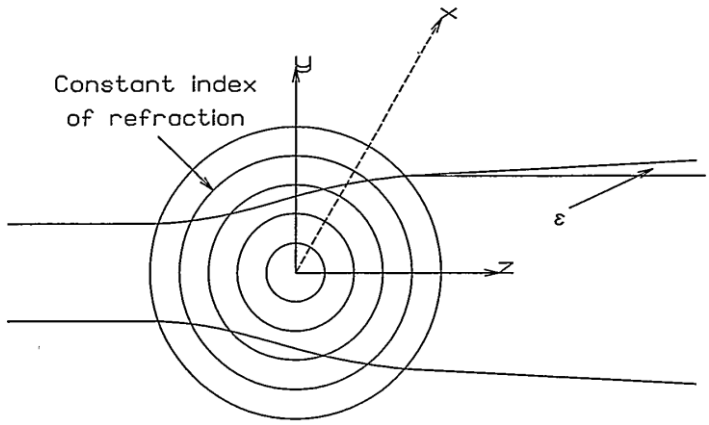

Figure 2.13 - Deflection of light beams through an area of circular symmetrically distributed variation of refraction index, [14]

Where n is the index of refraction, and x, y, and z are the spatial coordinates, as indicated in Figure 2.13. The total angular deflection in the *xz* and *yz* planes is called ε'_x and ε'_y respectively and can be described by:

$$\varepsilon'_x = \int \frac{1}{n}\frac{\partial n}{\partial x} dz$$
$$\varepsilon'_x = \int \frac{1}{n}\frac{\partial n}{\partial y} dz \qquad (1.3)$$

The area around the test-section has the light refraction index n_0, and the Snell's law can be applied to the light-beams as they leave the test-section:

$$n\sin(\varepsilon') = n_0 \sin(\varepsilon) \qquad (1.4)$$

The angle of deflection as the light leaves the test-section and continues through the rest of the Schlieren system will therefore be:

$$\varepsilon_x = \frac{1}{n_0}\int \frac{\partial n}{\partial x} dz$$
$$\varepsilon_y = \frac{1}{n_0}\int \frac{\partial n}{\partial y} dz \qquad (1.5)$$

Using a carefully designed Schlieren system, it is possible to measure the angular deflection of the beam in either direction. If the spatial variation of the light refraction index is known to be symmetrical, an estimate of its distribution can be made. Alternatively, in other words, given x, y, and that n follow a symmetrical distribution, n (x, y) can be calculated.

REFERENCES

[1] C. Dumouchel, 'On the experimental investigation on primary atomization of liquid streams', *Experiments in fluids*, vol. 45, no. 3, pp. 371–422, 2008.

[2] N. Chigier, 'An assessment of spray technology', *Atomization and Sprays*, vol. 3, no. 4, 1993.

[3] G. J. Smallwood and O. L. Gulder, 'Views on the structure of transient diesel sprays', *Atomization and sprays*, vol. 10, no. 3–5, 2000.

[4] H. Hiroyasu, 'Break-up length of a liquid jet and internal flow in a nozzle', in *Proc. 5th. ICLASS*, 1991, pp. 275–282.

[5] T. Ohrn, D. W. Senser, and A. H. Lefebvre, 'Geometrical effects on discharge coefficients for plain-orifice atomizers', *Atomization and Sprays*, vol. 1, no. 2, 1991.

[6] I. Carvalho, M. Heitor, and D. Santos, 'Liquid film disintegration regimes and proposed correlations', *International journal of multiphase flow*, vol. 28, no. 5, pp. 773–789, 2002.

[7] D. L. Siebers, 'Liquid-phase fuel penetration in diesel sprays', *SAE transactions*, pp. 1205–1227, 1998.

[8] J. E. Dec, 'A conceptual model of Dl Diesel combustion based on laser-sheet imaging', *SAE transactions*, pp. 1319–1348, 1997.

[9] C. Baumgarten, *Mixture formation in internal combustion engines*. Springer Science & Business Media, 2006.

[10] L. Julien, 'Characteristics of diesel sprays at high temperatures and pressures', PhD Thesis, Ph. D. thesis, The University of Brighton, United Kingdom, 2006.

[11] C. F. Bohren and D. R. Huffman, *Absorption and scattering of light by small particles*. John Wiley & Sons, 2008.

[12] M. Yamakawa, D. Takaki, T. Li, Y. Zhang, and K. Nishida, 'Quantitative measurement of liquid and vapor phase concentration distributions in a DI gasoline spray by the laser absorption scattering (LAS) technique', *SAE Transactions*, pp. 2194–2206, 2002.

[13] K. Sato, T. Tadokoro, K. Nishida, H. Yokohata, and M. Yamakawa, 'SC3-3: Mixture Formation Process of Wall-Impinging Spray by DI Gasoline Injector:

Comparison between Experiment and CFD Calculation (SC: Spray and Spray Combustion, General Session Papers)', in *The Proceedings of the International symposium on diagnostics and modeling of combustion in internal combustion engines 2008.7*, 2008, pp. 437–444.

[14] H. Paulsen, 'A study of transient jet and spray using a Shlieren method and digital image processing', *Dr. ing. thesis. University of Trondheim, Norwegian Institute of Technology (NTH), Division of Marine Engineering*, 1995.

[15] T. Kamimoto, H. Yokota, and H. Kobayashi, 'A new technique for the measurement of Sauter mean diameter of droplets in unsteady dense sprays', *SAE Transactions*, pp. 397–408, 1989.

[16] W. Thomas and others, 'SPSE handbook of photographic science and engineering', 1973.

[17] T. Ø. Ask, 'Ignition and Flame Growth in Lean Gas-air Mixtures: An Experimental Study with a Schlieren System', PhD Thesis, Department of Marine Engineering, Norwegian Institute of Technology …, 1992.

CHAPTER 3 EXPERIMENTAL SETUP

This chapter reports an overview of the experimental setups used for conducting the research activities presented. First of all, the objects of the research's study will be illustrated, the injector prototypes. After, the activities and the configurations adopted to carry out a complete characterization are shown.

The injectors used for the research activities are characterized by a piezoelectric control actuation and have different shapes: the first has a traditional hollow-cone shape, the second two, similar to the traditional multi-hole, characterized by 5 and 8 jets, which one with the difference of having a circular crown between the jets (5 jets). A high-pressure constant volume vessel was used to characterize the prototypes. Also, a hydraulic characterization of the hollow-cone nozzle injector was carried out through the Bosch's tube; therefore, the operating principle and methodology will be illustrated. Since the same piezoelectric actuation was used, it was considered appropriate to characterize only one prototype.

Concerning the engine tests, they were carried out with the prototypes and compared to the multi-hole prototype injector. In this section, a brief description of the heat release and engine efficiency analysis and additional information regarding the engine from gaseous analyzers and emissions will be discussed. In the end, the fuel's properties tested in this research project. During the discussion, in particular, in the analysis of engine performance, a further version of the hollow-cone will be presented, developed previously with a smaller cone angle, which was not very suitable for diesel combustion, and the results will be illustrated in the following chapters.

Concerning the fuel injection system control, a Labview program (through Compact-RIO hardware) was implemented to manage the injection pattern parameters such as ET, a number of injections, d_{well} time, voltage supply, and the pressure control on pump and common-rail.

Due to the difficulty in implementing and managing a prototype injector, some tests were not conducted. The following table (Table 3.1) summarizes the research activities performed in order to obtain a complete characterization of the prototypes.

Table 3.1 – Experimental activities for different injector prototypes.

Injector	Spray characterization	Hydraulic characterization	Engine test
MHN (Ref.)	X		X
HCN	X	X	
HCN-J	X		X
HCN-8J	X		X
HCN (old version)	X	X	X

3.1 The prototype injectors

The injectors used in research activities represent a prototype application; they are composed of a piezoelectric actuator and a "pintle type" pulverizer, and from it are named "Pintle Nozzle Injectors".

The tested injectors are outwardly opening nozzle injectors able to generate a hollow cone spray like that produced in some GDI injectors [1]. The maximum injection pressure is 1600 bar, about three times higher than the typical gasoline hollow cone injector. A straightforward scheme of the geometrical configurations of the prototypes, compared with conventional MHN, is reported in Figure 3.1. The architecture used is the same for both injectors, therefore also the main mechanical characteristics: the needle seat diameter is 3.5mm, and the maximum needle lift is 30μm.

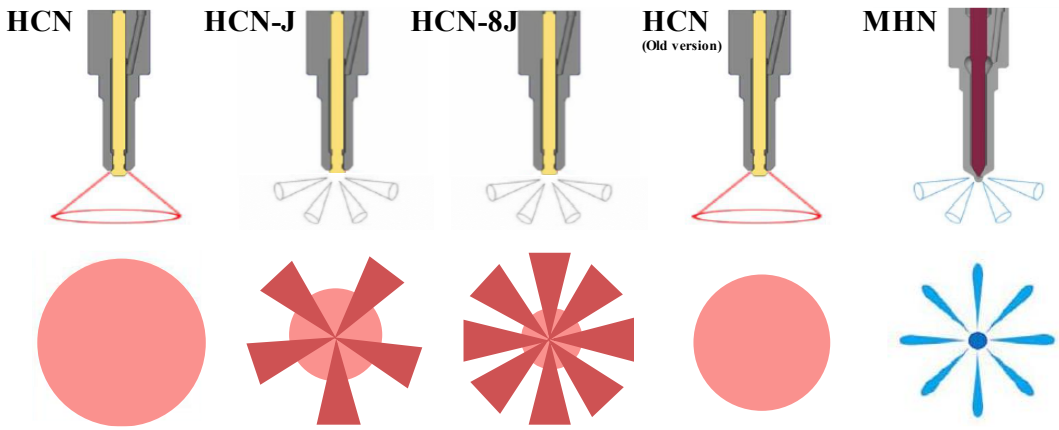

Figure 3.1 – Spray pattern structure comparison.

As already discussed in the introduction, this project carried out in collaboration with the CRF was aimed to develop a prototype injector suitable for compress ignition

combustion. The first injector designed with this architecture is an HCN; in Figure 3.1 is called with HCN (old version). Based on the experimental activities carried out (spray characterization and engine tests), many changes were made to the shape in terms of the number of jets and spray cone angle. Starting from the same structure, in fact, different pintles were developed, illustrated in Figure 3.1. Below the shapes will be illustrated.

The HCN and HCN-old version generate a hollow cone spray; the second and third characterized with five (HCN-J) and eight guidings (HCN-8J) walls on the pintle added to generate compact jets as a multi-hole nozzle; moreover, they are also characterized from a conical liquid sheet, as shown in Figure 3.1. The main peculiar characteristics of the prototypes consist of:

- Needle direct piezo actuation;
- Operation with high flow rate and small needle lift (≈10÷40 μm) → ≈3/4 times higher than a standard Multi-Hole with 7 holes;
- Precise control of the needle lift and the injection event (capable of actual rate shaping injection);
- Max p_{inj} of about 160 MPa;
- p_{inj} available just upstream the spray delivering section (Figure 3.2);
- Outwardly needle designed for a spray cone angle of 145° (HCN, HCN-J) and 100° (HCN-8J, HCN-old version)

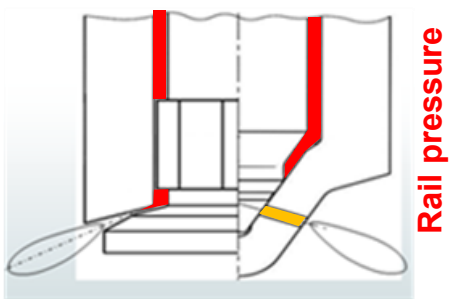

Figure 3.2 - Spray delivering section.

For the pintle type nozzles, the circumferential area depends linearly with the needle lift. In turn, it depends on the supply voltage; the trend is reported in Figure 3.3. For some dozens of microns of the needle lift, the discharge area is well more extensive than that of a classical MHN. E.g., for a needle disk diameter of 3.5 mm and a needle lift of 24 μm, the discharge area is of 0.263 mm^2, while for a seven holes injector with a hole diameter of 141 μm the discharge area is 0.109 mm^2.

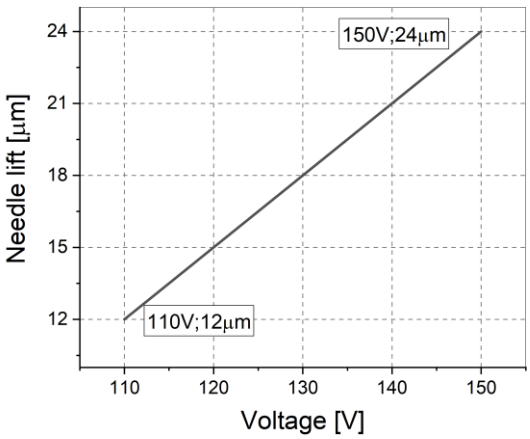

Figure 3.3 – Needle-lift vs. supply voltage.

The piezo-actuators enhances the injection stability and drift compared to the solenoid technology shortening also the intervals among single injection events from 0.3 ms (solenoid) to 0.1 ms (piezo) [2]. It permits greater flexibility of the injection pattern in terms of the number and duration of the events compared to solenoid actuators.

3.2 Spray characterization

The prototypes spray characterization was performed in a constant volume combustion vessel, optically accessible by three quartz windows, 80 mm in diameter, allowing the admittance to the investigated area. A fourth one was used for housing the injector holder. The injector was in a holder, including a jacket for the temperature control of the nozzle nose and connected to a chiller for fluxing a cooling liquid. The fuel is supplied through a common rail, heated by electrical resistance, with the temperature-controlled by a J-type thermocouple located in the rail.

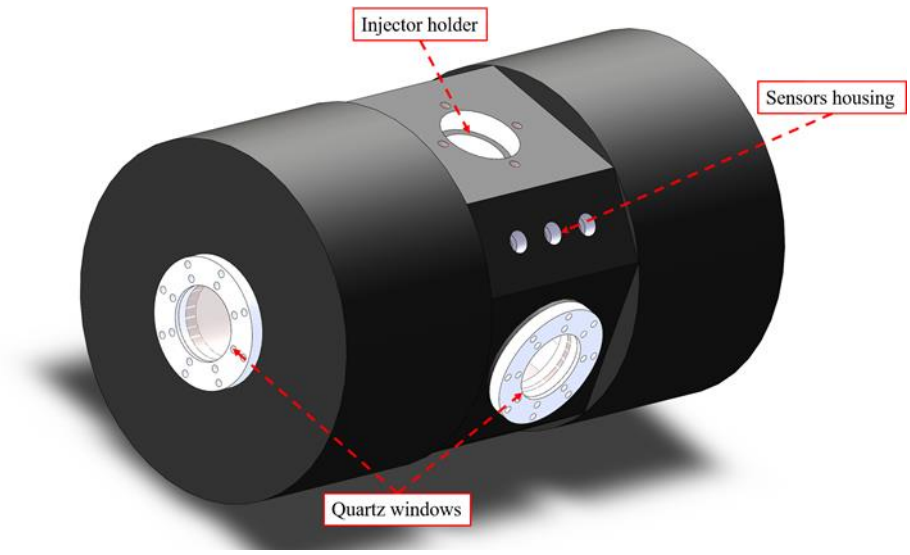

Figure 3.4 - Optical high-pressure test chamber.

A governor achieved the nozzle and fuel temperature management via a remote computer using a homemade software. Previous calibration of liquid temperature for the jacket and the nozzle nose was carried out using a customized injector equipped with a thin thermocouple located close to the fuel exit and allotted along a groove on the injector body.

A cooling cup surrounding the injector mount was used to control the injector temperature. Both the injector and the fuel temperature [T_{fuel}] was kept at 363 K. A mapping of the injector temperature, in order to determine the conformity between the set point of the fluid and the effective nozzle temperatures, reveled a correspondence of ± 1 °C.

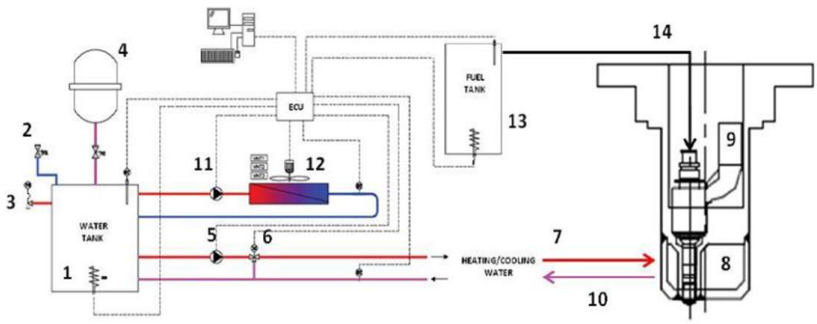

Figure 3.5 - Schematic of the nozzle and fuel temperature governor.

The vessel was kept at ambient temperature in nitrogen or hexafluoride gas at atmospheric backpressure, and there was no combustion during the tests while a vacuum pump realized the sub-atmospheric experimental conditions down to 0.03

MPa. A pneumatic high-pressure injection system pressurized the fluid up to 300 MPa and fed the fluid to the injector. No rotating organs were on the apparatus, and an external TTL signals draw the injector.

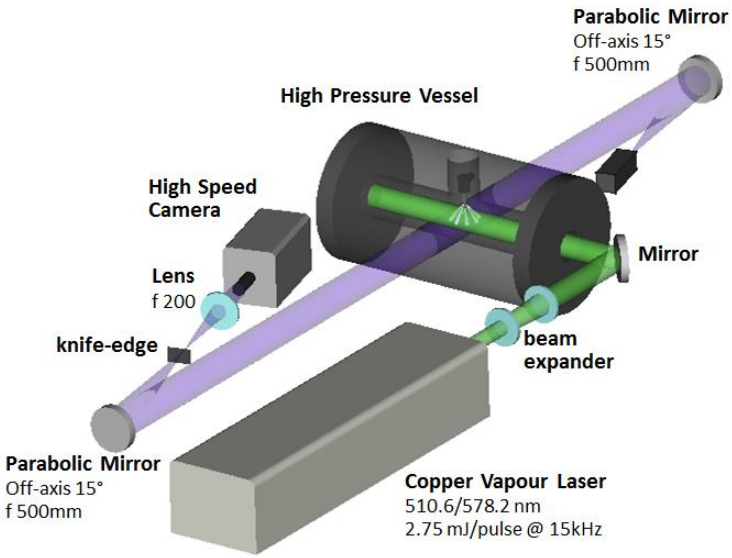

Figure 3.6 - Sketch of the optical set-up at the high-temperature condition.

The spray evolution was characterized using two optical techniques, schlieren, and Mie scattering. Schlieren images take into account of both liquid and vapor fraction of the spray, while the scattered light is mainly due to the liquid fraction. A sketch of the optical set-up is shown in Figure 3.6. The Schlieren set-up was arranged according to the typical Z-folded type, using two 15° off-axis parabolic mirrors (4 inches diameter, 508 mm PFL). The light source was a pulsed blue Led (Omicron LEDMOD V2 - 455nm/450mW), with the pulse length set at 6μs. The knife-edge was placed horizontally. A copper vapor laser (Oxford-CU15A) was the scattering light source, placed at 90° to the collecting optics. The laser can operate up to 15kHz, with a maximum pulse energy of about 2mJ and a pulse duration of about 60ns. The laser beam was expanded and collimated to illuminate the whole spray. The images of the spray were acquired using a high-speed C-Mos camera (Photron FASTCAM SA4), at a rate of 45000 frames per second (fps) with an image window of 384x192 pixels. The camera was equipped with a 90 mm objective, f 1:2.8.

In order to obtain a complete spray characterization, at standard temperature conditions, a different configuration was used for both injectors, using only the Mie-scattering technique. The spray has been characterized in both developed directions,

axial, and radial. The following figure shows the different experimental layout and the optical setup.

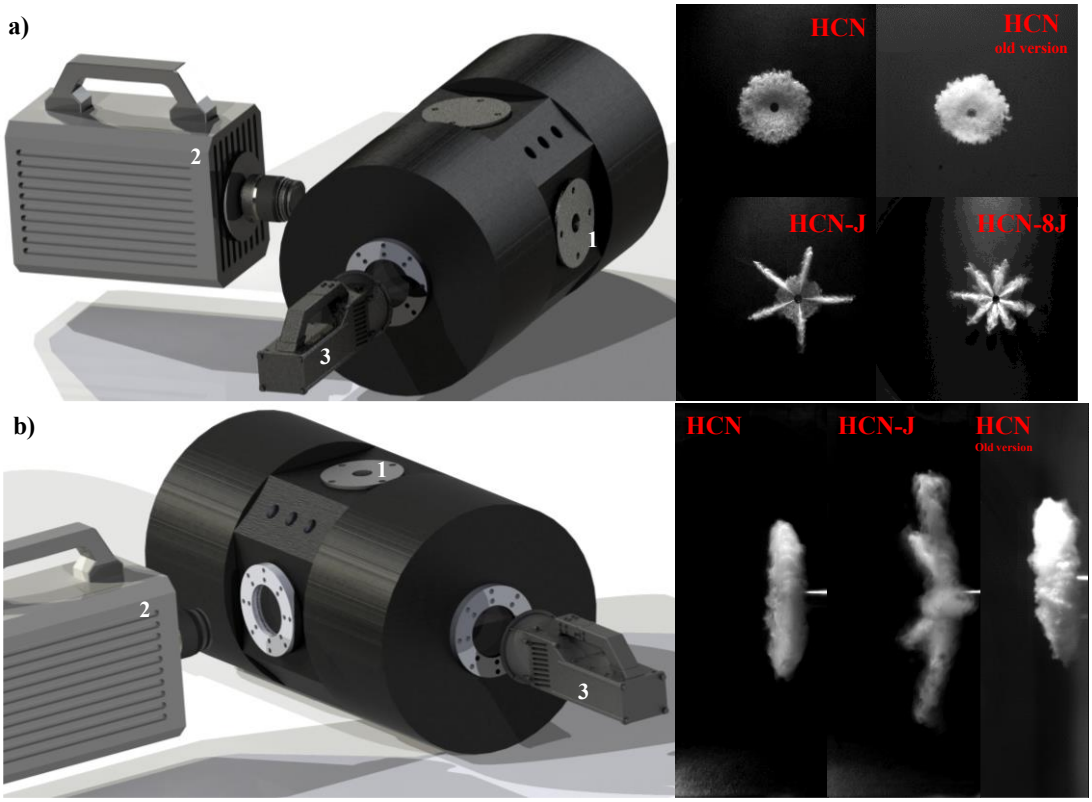

Figure 3.7 - Optical layout for the Mie scattering measurements in two different configurations a) radial, b) axial, and the corresponding acquired image.

Table 3.2 - Optical setup for the Mie scattering measurements in two different configurations

Injector	**Configuration**	**Rate [fps]**	**Shutter [µs]**	**Dimension**	**Cal. factor [p/mm]**
HCN	Radial	30000	8,37	320x320	1,85
	Axial	18000	8,46	256x656	4,6
HCN-J	Radial	30000	8,37	320x320	1,9
	Axial	18000	8,46	256x656	4,6
HCN-8J	Radial	30000	8,37	320x320	1,8

As shown in the figure, only the HCN-8J was not characterized laterally, since it was not considered necessary. The images were processed through a customized procedure developed in MATLAB (chapter 4) to better outline the contours of the liquid phase and the vapor/atomized zone

3.3 Hydraulic Characterization

Several techniques can be applied for the measurement of the injection hydraulic behavior, such as momentum flux [3, 4], Zeuch's [5, 6], and Bosch's method [7]. With the momentum flux method, the impingement force of the spray on a surface is estimated through a force sensor. Considering the fluid at the nozzle-exit in liquid-phase flowing through the pipe area with a constant velocity, the instantaneous values of momentum and mass rate can be easily estimated [8]. This method is widely used for investigating the properties of diesel sprays because it can provide information about every single jet composing the spray and cavitation area. Looking at the DISI nozzles, the use of this technique is limited by the spray configuration, due to the low opening of the cone-angle, it is impossible to limit the impact of fuel on the sensitive surface to a single jet.

Using Zeuch's method, the spray is injected in a closed, fixed-volume chamber filled with the same injected fluid. In the measuring chamber, the pressure level before the injection event is constant. The fuel delivering in the control volume induces a pressure variation proportional to the instantaneous injection rate [7, 8].

Similarly to the Zeuch method, the Bosch method consists of an injection into a fuel-filled measuring chamber with specific backpressure[7, 9]. Downstream a tube, with adequately designed length and cross-area, reduces the back-pressure signal oscillations [10] and the interference with the returning shock wave. The discharged fuel produces a pressure increase inside the tube, proportional to the amount of the fuel mass.

Figure 3.8 shows the AVL injection rate meter used for the experimental tests. Specifically, the Bosch Tube Gauge Rate System collects the single shot through the detection of the pressure increase induced by the entering fluid in the control volume. The control volume is a small chamber located immediately downstream of the nozzle, equipped with a transducer, which detects the instantaneous changes in pressure due to the fuel introduction. The used pressure transducer is GM12D-AVL. The detected electrical signal is amplified by a charge amplifier AVL 3057-V01. The measurement resolution is determined by the time base of the transducer-amplifier system. Downstream the control volume, a hydraulic tube filled with fuel lowers the pressure oscillations and delay the return back.

The tube has a total length L of 12 m, 4 mm inner diameter. This inside diameter determines the magnitude of the pressure waves. The length of the measuring tube

affects the attenuation efficiency of the device and the measurable injection frequency. Longer is the tube later being the shock wave reflection (period 2L/a, where a is the sound speed in the fuel).

Figure 3.8 - AVL Injection Gauge Rate System.

The size of the orifice determines which part of the fuel transported with the pressure wave is reflected and which part enters the follower tube. If the orifice is too large, most of the transported fuel passes through the orifice, and a negative pressure wave is reflected in the measuring tube. At the end of the duct, a calibrated control valve regulates the pressure in the pipe, keeping constant the pressure to avoid cavitation effects by draining the excess of fuel generated by incoming new fuel.

The instantaneous fuel-injected mass is proportional to the pressure variation through parameters related to the geometry and the chemical-physical characteristics of the fuel, as reported in formula 3.1:

$$\dot{v} = \frac{\Delta p_{gauge} A_{tube}}{a\rho} 10^5 \tag{3.9}$$

where $\dot{v}$ is the instantaneous volume fuel rate [mm^3/s], Δp_{gauge} [bar] is the pressure change, A_{tube} is the area of the tube inner section [mm^2], a is the sound speed in the fluid [m/s], ρ is the fluid density [kg/m^3]. Once the flow rate has been estimated, the total injected amount in the period [$t_{i\text{-}inj}$, $t_{f\text{-}inj}$] is:

$$V = \int_{t_{i-inj}}^{t_{f-inj}} \dot{v} dt \tag{3.10}$$

The results obtained by the fuel injection meter have been compared with the weight of the fluid averaged on 1000 shots, collected at the valve exhaust, by a high precision balance (OHAUS Explorer 410GX1) having a precision of 0.001 g.

3.4 Single Cylinder Research Engine

The different injectors configurations were tested on a proper build single-cylinder compression ignition engine testbed. The combustion architecture is representative of the Euro 5 light-duty diesel technology. Indeed, the combustion architecture (connecting rod, piston, cylinder head, etc.) derives from production series engines but has been modified to run in single-cylinder mode. Fuel, cooling, and lubrication systems are decoupled from the engine allowing greater flexibility of their control parameter. Intake and exhaust gas lines are adequately designed to realize accurate controls of the boost and backpressure variables.

In order to make the results representative of the reference multi-cylinder engine (MCE), the boundary conditions or the control variables of the auxiliary systems (boost, EGR, oil cooling, water cooling, fuel cooling) are set as those of the reference multi-cylinder engine.

Auxiliary systems for boost, cooling, lubrication, etc., are not directly coupled to the engine, thus permitting the complete flexibility for the control of these parameters without influencing the load conditions. The boosted air is provided and controlled by an external air compressor. This approach offers great flexibility in operating conditions. As a result, the combustion characteristics are comparable to those of the reference engine, making the outputs transferable to the real multi-cylinder engine.

The engine calibration parameters (injections, intake throttle valve, EGR valve, VGT, etc.), pressure, temperature signals, and pollutant emissions are monitored, controlled, and acquired through National Instruments HW platform and LabVIEW® software.

The diesel fuel measurements are realized by employing a gravimetric balance (AVL 733). For the air measurement, two different air mass flow meters are installed in order to have higher accuracy, depending on the operating range: Emerson Coriolis (0-150 kg/h) and ABB thermal (0-400 kg/h) mass flow meter. The test cell layout is depicted in Figure 3.9, while Table 3.3 describes the main engine characteristics.

Table 3.3 - Single Cylinder engine geometrical characteristics.

Displaced volume	477.5 cc
Stroke	90 mm
Bore	82 mm
Compression ratio	15.5
Number of Valves	4
Diesel Injection System	Common rail (max inj. pressure=1800 bar)
Diesel Injector	Piezoelectric injectors
	Solenoid 7 holes micro-sac

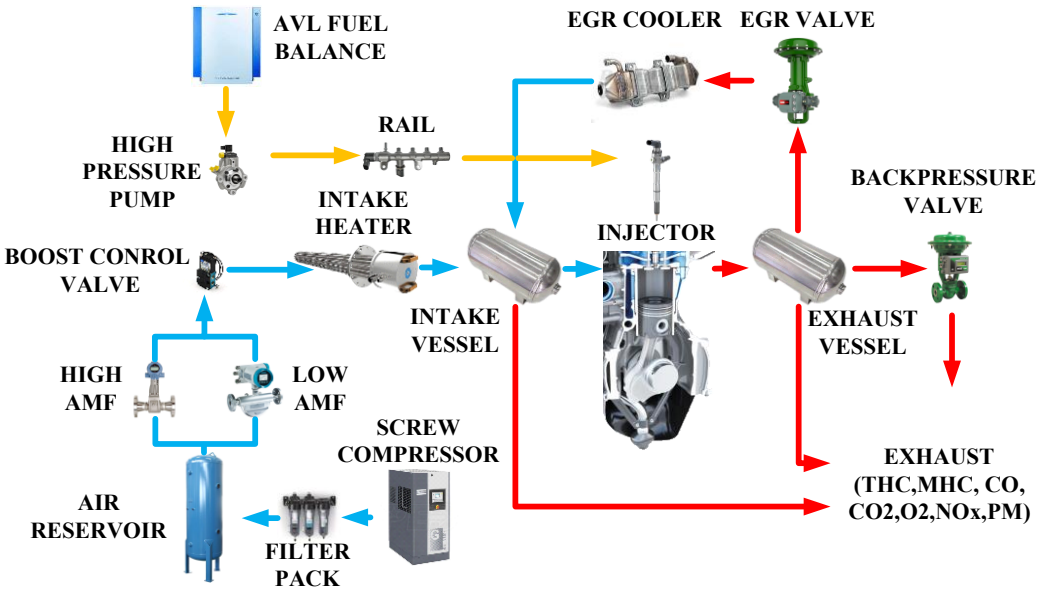

Figure 3.9 - Single cylinder test cell layout.

The indicated pressures are measured through a Kistler 6125B flush-mounted piezo-quartz transducer, fitted inside the head glow plug hole, and acquired with a resolution of 0.1 CAD. The averaged pressure signal, for the calculation of the indicated mean effective pressure (IMEP) and the apparent heat release (HR) and heat release rate (HRR), are averaged over 128 consecutive cycles. The emitted smoke is measured using the AVL 415S smoke-meter. The engine-out gaseous emissions in terms of THC, MHC, NO_x, CO, CO_2, and O_2 are measured using an integrated emissions test bench.

3.4.1 Heat Release Analysis, efficiency, and energy balance.

The combustion analysis is realized by calculating the heat release (HR) and the heat release rate (HRR) based on the in-cylinder pressure. The in-cylinder pressure is detected fitting piezoelectric pressure sensors into the cylinder head. The pressure signals and the crank angle position of the crankshaft were synchronized utilizing high-resolution encoders (0.1 CAD).

The heat release analysis is based on the first law of thermodynamics, as reported by Heywood [11]. The heat release rate is calculated based on the cylinder pressure measurement, adopting the ideal gas law and the mass conversation law, using Equation 3.3, which does not consider the heat transfer losses since it is calculated in real-time while running the engine.

$$\frac{\partial Q}{\partial \theta} = \frac{\gamma}{\gamma - 1} p \frac{\partial V}{\partial \theta} + \frac{1}{\gamma - 1} V \frac{\partial V}{\partial \theta} \tag{3.11}$$

Where p and V are vectors representing the in-cylinder pressure and the calculated volume. γ is the specific heat ratio of air. While the heat release rate is an excellent tool to present the combustion process and trends, it is important to consider the accuracy of the calculated heat release rate due to the tuning factors.

Some of the fuel chemical energy is converted into mechanical through the internal combustion engine. The flow of energy of internal combustion engines is reported from the Sankey diagram [12] in Figure 3.10. The flow of energy through each of these stages and the energy losses are described in the text below the figure, both presented as mean effective pressure (MEP), which is defined as the work or energy per cycle normalized by the engine's displacement volume [12].

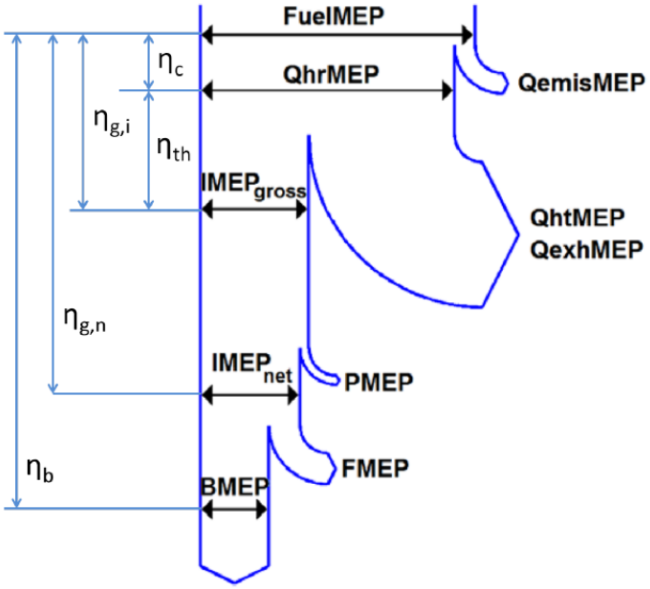

Figure 3.10 - Sankey diagram of mean effective pressures [12].

The experimental campaign was performed on a single-cylinder engine, while the friction losses were calculated on the base of internal available experimental data on a multi-cylinder engine [13].

The energy balance calculated applying the first law of thermodynamics on the engine is considered:

$$\dot{m}LHV = P_{brake} - P_{frict-loss} - P_{pump-loss} - \dot{Q}_{HT} - \dot{Q}_{EGR} - \dot{Q}_{Exh} - \dot{Q}_{comb-loss} \quad (3.12)$$

The $\dot{m}_f$ and LHV_f are the fuel mass flow rate and fuel lower heating value, respectively. The P_{brake}, $P_{frict-loss}$ and $P_{pump-loss}$ are the brake power, friction, and pumping power losses, respectively. The engine heat losses can be divided into four contributes: combustion loss ($\dot{Q}_{comb-loss}$), exhaust heat loss ($\dot{Q}_{Exh}$), EGR heat cooling loss ($\dot{Q}_{EGR}$) and heat transfer loss ($\dot{Q}_{HT}$) from the radiation and convection (cylinder head, cylinder liner, exhaust cylinder port, oil, and water cooling). Each term is calculated following the equations reported in Heywood [11].

The EGR loss due to the presence of the heat exchanger is calculated as:

$$\dot{Q}_{EGR} = \dot{m}_{EGR} \frac{c_{p_{IN}} + c_{p_{OUT}}}{2} \left(T_{IN-cooler} - T_{OUT-cooler} \right) \quad (3.13)$$

The exhaust loss $\dot{Q}_{Exh}$ is calculated considering the heat transfer to the ambient. The $\dot{Q}_{Exh}$ can be divided into two parts: from the exhaust manifold to the low-pressure EGR split ($\dot{Q}^{I}_{Exh}$) and from the EGR split to the ambient ($\dot{Q}^{II}_{Exh}$).

$$\dot{Q}_{Exh} = \dot{Q}^{I}_{Exh} + \dot{Q}^{II}_{Exh} \tag{3.14}$$

$$\dot{Q}^{I}_{Exh} = \left(\dot{m}_{air} + \dot{m}_{EGR} + \dot{m}_{f}\right)\frac{c_{p_{Exh}} + c_{p_{after_turbo}}}{2}\left(T_{Exh} - T_{after_turbo}\right) \tag{3.15}$$

$$\dot{Q}^{II}_{Exh} = \left(\dot{m}_{air} + \dot{m}_{f}\right)\frac{c_{p_{amb}} + c_{p_{after_turbo}}}{2}\left(T_{after_turbo} - T_{amb}\right) \tag{3.16}$$

The $c_{p_{exh}}$, $c_{p_{after\,turbo}}$, and $c_{p_{amb}}$ are calculated starting from the intake and exhaust gaseous composition exhaust after the turbo and ambient temperature, respectively, using the JANAF table reported in [11]. Thus, applying the first law of thermodynamics, it is possible to calculate the heat transfer ($\dot{Q}_{HT}$) as the difference of the other addends.

The following relations (3.9-10) were used for the calculation of the indicated specific fuel consumption (ISFC), as well as the fuel (η_{fuel}), thermodynamic ($\eta_{thermal}$) and combustion (η_{comb}) efficiencies:

$$ISFC = \frac{\dot{m}_{f}}{P_{ind}} \tag{3.17}$$

$$\eta_{fuel} = \frac{1}{ISFC \cdot LHV} = \eta_{comb} \cdot \eta_{thermal} \tag{3.18}$$

The indicated specific emissions are calculated as the mass flow rate of pollutant (X) per unit of net indicated power (P_{ind}) output:

$$isX = \frac{\dot{m}_{X}}{P_{ind}}\left[\frac{g}{kWh}\right] \tag{3.19}$$

3.4.2 Emissions Measurement System

The engine out gas emissions and soot mass were measured through dedicated measurement systems. Each analyzer was calibrated using a dedicated reference gas before every set of tests. After a stabilization phase of about 10 minutes, the emissions data were acquired in continuous mode for 2 minutes for each operating point.

The engine-out gaseous emissions in terms of THC, MHC, NO_x, CO, CO_2, and O_2 are measured using an integrated emissions test bench. In particular, the THC and MHC are detected utilizing flame ionization detectors (ABB and Emerson respectively), the NO_x employing a chemiluminescence detector (Ecophysics CLD700), CO and CO_2 through nondispersive infrared detectors (Emerson) and the O_2 through a paramagnetic sensor (Emerson). The emitted smoke is measured employing the AVL 415S smoke-meter.

The EGR fraction was measured starting from the CO_2 concentration volume concentration of the intake and exhaust following the equation:

$$EGR = \frac{CO_{2_{intake}}}{CO_{2_{exhaust}}} \tag{3.20}$$

3.5 Fuels

Several fuels have been used for the test campaign. For the hydraulic and spray characterization, it was used n-heptane, thanks to its much lower boiling point compared to commercial diesel. The use of n-heptane allows us to evaluate the spray behavior in evaporation conditions at room temperature, as well as to validate the numeric codes due to known thermodynamic properties. The engine test, instead, was used commercial diesel. The fuel characteristics are listed in Table 3.4.

Table 3.4 - Fuel properties [11, 14, 15].

Feature	Diesel (NO FAME)	N-heptane
Density [kg/m^3] STP	836.7	679.5
Cetane number [-]	56.2	100
FAME content [%vol]	0.49	
FBP [°C]	362.3	98.5
LHV [MJ/kg]	42.95	44.56
Auto-Ignition [°C]		220
A/F$_{stoich}$ [-]	14.7	15.15
H/C [-]	1.858	2.28
Kin. Viscosity [mm^2/sec]	2.892	0.928-0.511

For the hydraulic characterization, the n-heptane was treated with 400ppm of lubricity additive, Infenium R655, in order to guarantee adequate lubrication of the high-pressure fuel pump as well as the rest of the fuel injection system, which is not adapted to work with low viscosity fuels.

REFERENCES

[1] J. Nouri, M. Hamid, Y. Yan, and C. Arcoumanis, 'Spray characterization of a piezo pintle-type injector for gasoline direct injection engines', in *Journal of Physics: Conference Series*, 2007, vol. 85, p. 012037.

[2] A. Magno, E. Mancaruso, L. Sequino, and B. Vaglieco, 'Analysis of spray evolution from both piezo and solenoid injectors in single cylinder research engine', in *ILASS-2013, 25th European Conference on Liquid Atomization and Spray Systems, at Chania, Greece*, 2013.

[3] Y. Takagi, 'A new era in spark-ignition engines featuring high-pressure direct injection', in *Symposium (international) on combustion*, 1998, vol. 27, pp. 2055–2068.

[4] F. Zhao, M.-C. Lai, and D. L. Harrington, 'Automotive spark-ignited direct-injection gasoline engines', *Progress in energy and combustion science*, vol. 25, no. 5, pp. 437–562, 1999.

[5] Z. Han, R. D. Reitz, J. Yang, and R. W. Anderson, 'Effects of injection timing on air-fuel mixing in a direct-injection spark-ignition engine', *SAE transactions*, pp. 848–860, 1997.

[6] A. C. Alkidas, 'Combustion advancements in gasoline engines', *Energy Conversion and Management*, vol. 48, no. 11, pp. 2751–2761, 2007.

[7] G. R. Bower and D. E. Foster, 'A Comparison of the Bosch and Zudch Rate of Injection Meters', WISCONSIN UNIV-MADISON ENGINE RESEARCH CENTER, 1991.

[8] B. Jiang, X. Pan, F. Liu, C. Wang, and X. Feng, 'Experimental Investigation on Fuel Spray Optimization in Gasoline Direct Injection Engine', in *Proceedings of the FISITA 2012 World Automotive Congress*, 2013, pp. 45–53.

[9] W. Hentschel, 'Optical diagnostics for combustion process development of direct-injection gasoline engines', *Proceedings of the combustion institute*, vol. 28, no. 1, pp. 1119–1135, 2000.

[10] M. Drake and D. Haworth, 'Advanced gasoline engine development using optical diagnostics and numerical modeling', *Proceedings of the Combustion Institute*, vol. 31, no. 1, pp. 99–124, 2007.

[11] J. B. Heywood, 'Internal combustion engine fundamentals', 1988.

[12] M. Shen, *Particulate matter emissions from partially premixed combustion with diesel, gasoline and ethanol*. Division of Combustion Engines, Department of Energy Sciences, Lund University, 2016.

[13] G. Di Blasio, G. Belgiorno, C. Beatrice, V. Fraioli, and M. Migliaccio, 'Experimental evaluation of compression ratio influence on the performance of a dual-fuel methane-diesel light-duty engine', *SAE International Journal of Engines*, vol. 8, no. 5, pp. 2253–2267, 2015.

[14] S. R. Turns and others, *An introduction to combustion*, vol. 499. McGraw-hill New York, 1996.

[15] I. Glassman, R. A. Yetter, and N. G. Glumac, *Combustion*. Academic press, 2014.

CHAPTER 4 DIGITAL IMAGE PROCESSING

Reference: "Image processing of vaporizing GDI sprays: a new curvature-based approach"[2].

The only quantity directly measured using any black and white photo-graphic technique is the light-intensity. However, if the relationship between light-intensity and other parameters are known, much more information can be acquired from an image. This calls for a new set of tools that have not yet been much used in engine research.

Digital image processing (DIP) is a field of research that got started when jour-nalists needed some way of transferring images from one place to another using ordinary telephone fines in the 1920s [1]. Since the 1960s, the tech-niques have been used extensively for military purposes, in space research, and medical science. Moreover, since the 1980's some use of digital image pro-cessing have been made in engine-related research. Some of the possibilities available using DIP are similar to what can be done using a traditional dark-room technique, with the main difference being that the result can be seen immediately on the computer screen. Other possibilities reach far beyond what can be done with photographic film.

An image in DIP terms can be viewed as a matrix of data containing information about a small part of the image. Each element of this matrix is usually referred to as a "pixel". Furthermore, the information stored in each pixel is either the fighting intensity, if it is a black and white image, or the intensity of the primary colors (red, green, and blue if it is a color image. Usually, the number of possible pixel values is limited to what can be stored in one Byte on the computer used (or one byte each for red, green, and blue for color images). This means that only 256 individual shades of gray, or 16.7 million colors can be represented. It is beyond what the human eye can distinguish between and thus is enough for the most traditional use of images.

[2] https://doi.org/10.1088/1361-6501/aa9301

4.1 Software for digital image processing

Even though there exists a large selection of commercial software for DIP, it is this writer's view that these are, in general, more suited for artistic work than for scientific research. The reason for this is that when one is looking for data that goes beyond just considering an image as a picture, access to each pixel is necessary, and this makes access to the source code a crucial necessity.

For this reason, a code was implemented, which allowed the spray segmentation objectively and in detail in order to characterize the jet through macroscopic parameters. For clarity, images of GDI sprays will be used in the chapter, since having many operating conditions in terms of chamber temperature and pressure (air density), it has allowed validation on a wide field of analysis. This code has also been validated for diesel spray, as will be illustrated in the spray characterization chapter.

4.2 State of the art

Whatever the optical technique used, the fundamental step in the analysis of a spray image is its segmentation, to properly separate the spray image foreground from the background. Literature offers a multitude of segmentation methods, highlighting their potentialities and application limits [2]. As regards automotive sprays, both diesel and GDI, several approaches have been proposed so far to determine the right intensity threshold value that can identify all the image pixels belonging to the spray, whether it is the liquid or the vapor phase. In this field, it is a collective experience of how challenging it is to find the "optimal" segmentation method, because of the transient nature of sprays and the most varied experimental conditions. The well-known Otsu's method [3], for example, is a global thresholding method that provides quite reliable results if the image intensity histogram meets the requirements of proper bimodal distribution. The Likelihood Ratio Test Method (LRT), introduced by Pastor et al. [3, 4] for the segmentation of liquid diesel spray images, follows a more refined statistical approach, which overcomes some limitations of the Otsu's method [6]. Kronhjort and Wåhlin [7] investigated liquid diesel spray images under different experimental configurations and background noise. They proposed to evaluate the optimum threshold using the second-order derivative of the image histogram and operating just on the background pixels. The method was applied to effectively segment both scattering and Schlieren spray images [7–10]. It is worth noting that almost all the methods proposed so far in the literature can rarely avoid pre- and post-processing procedures to "clean" the spray contours from noise fluctuations. Therefore, images

are subjected to more or less strict filtering procedures and/or morphological processing (erosion, dilation, filling, etc.), and sometimes also adjustments of the image intensity (brightness, contrast, gamma correction), before achieving a reliable result.

With the above description, we intended to provide just a brief overview of commonly used spray image threshold approaches. In any case, whatever the segmentation method used, its effectiveness depends to a large extent from the signal to noise ratio of the image. It proves challenging to unambiguously discern the contours of a spray from the background in a noisy image [11, 12]. At the outer edges of the liquid phase of a spray, the scattering volume reduces, and the droplet concentration rapidly drops; hence, the intensity values of the scattering image blurs with the background. It is even more so true towards the end of the injection of vaporizing sprays, where the small residual droplets are highly dispersed in the environment, and the scattering signal progressively vanishes. Under these conditions, it is quite problematic outlining the liquid spray contours, if any. Therefore, before applying any segmentation method, image filtering is recommended. Optimal filtering should suppress or profoundly smooth noise and, at the same time, preserve the edges of the spray image. The filtering methods commonly used consist of convolving the image with a proper filter kernel (mean, median, Gaussian, Wiener, etc.), and such smoothing procedures likely alter the contours of the spray image, compromising to a certain extent the result of the segmentation process. However, it should be emphasized that such procedures could be necessary under harsh experimental conditions, such as those achieved in pre-burn combustion vessels [12, 13].

Variational methods, which play a pivotal role in the whole field of image processing [14, 15], can help us in the optimal filtering of spray images. Their diffusion in this field was probably hampered by their inherent mathematical complexity and the required computational effort. In this scenario, the remarkable work of Gong and Sbalzarini [16, 17] has overcome such computational constraints. They developed a filter-based approach to reduce variational energies, containing generic data-fitting terms, based on reducing just the regularization part of the variational energy. In their work, they presented fast discrete filters for regularizers based on Gaussian curvature, mean curvature, and total variation.

The analysis of the vapor phase of a spray in schlieren images is even more complicated. The intensity oscillations induced by the vapor gradients are comparable to the intensity values of the image background, also characterized by strong schlieren oscillations due to thermal gradients. In this case, the preliminary step of the

segmentation process should consist of a proper background correction, aimed to smooth as much as possible the image background. Subsequently, a selective image enhancement, restricted to the schlieren texture of the vapor phase, could greatly simplify the detection of the spray contours. This has been achieved in this paper by exploiting the principal curvatures of the schlieren image surface. This approach allows unambiguously distinguishing the contours of the spray vapor phase with an impressive detail level, thus providing a remarkable step forward in the process of segmentation of schlieren images of vaporizing spray.

In this article, we propose a new procedure for the segmentation of spray images, using variational methods for their filtering and implementing a method, having some original features, for the thresholding of scattering and Schlieren images. The segmentation procedure has been implemented in MATLAB. Its potentialities have been evaluated in the analysis of Schlieren and Mie-Scattering images of spray under engine-like operating conditions in a constant volume vessel.

4.3 Segmentation model

4.3.1 Curvature and Total Variation Filters

In the following, the approach of the variational method is briefly described, illustrating the features of the unique solution provided by Gong and Sbalzarini [16, 17].

The variational approach aims to find a minimizing function $\widehat{I_F}$ to an energy functional $\mathcal{E}(I_F) = \mathcal{E}_{\Phi_0}(I_F, I) + \lambda\mathcal{E}_{\Phi_1}(I_F, I)$ where I is the input image, and I_F is the regularized image. The energy functional is expressed as a linear combination of the data-fitting energy $\mathcal{E}_{\Phi_0}(I_F, I)$ and the regularization energy $\mathcal{E}_{\Phi_1}(I_F, I)$, weighted by the regularization parameter λ. The data-fitting term (a norm or divergence [19]) measures how I_F fits the image I. The L^2 norm, for example, corresponds to the classical least-squares criterion. The regularization term, instead, formalizes prior knowledge about I_F. Gong and Sbalzarini have provided a rapid approximate solution to the problem. Their approach was based on reducing just the regularization part of the variational energy while guaranteeing non-increasing total energy. They presented fast discrete filters for regularizers based on Gaussian curvature (GC), mean curvature (MC), and total variation (TV). The GC prior assumes that the regularized image I_F is a developable surface, MC assumes that it defines a minimal surface, and TV assumes that the image is a piecewise constant function. Interpreting I_F and I as geometric

surfaces over the bi-dimensional (x, y) image domain, the curvature can be computed by taking their partial derivatives.

The meaningful properties of the GC, MC, and TV filters can be summarized as follows:

- They do not need the gradient of the energy and can, therefore, handle generic data-fitting terms.
- They do not assume the differentiability of the signal. Therefore, edges are preserved.
- They have linear algorithmic complexity in the number of image pixels and only require as much memory as the image, plus 17 numbers.

It seems almost useless to point out that its edge-preserving characteristic should make this approach a powerful tool in the segmentation process of spray images.

The authors have implemented the filters algorithms in MATLAB, Java, and C++. The software and source code are publicly available from the MOSAIC Group's web site [20]

4.3.2 Image Processing

This section describes the image processing method. The algorithm steps are detailed regarding Schlieren/Mie-scattering images of a vaporizing spray of iso-octane, at a pressure of 20 MPa, and a temperature of 363K injected in a Nitrogen environment at a temperature of 573K and density of 1.12 kg/m^3. The spray images shown in Figure 4.1 were acquired at 720μs ASOI. The background images are also shown.

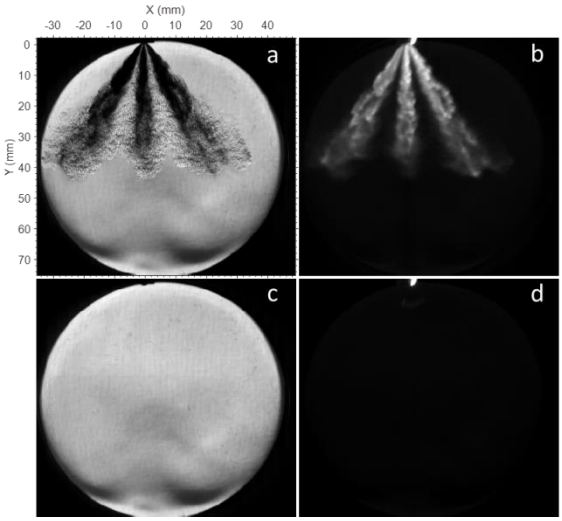

Figure 4.1 - Top: Schlieren (a) and Mie-scattering (b) images, acquired 720µs after SOI, iso-octane (P_{inj}=20MPa, T_{fuel}=363K) injected in nitrogen (ρ_{amb}=1.12kg/m^3, T_{amb}=573K). Bottom: Schlieren (c) and Mie-Scattering (d) background images.

The processing method of Mie-scattering images is first described.

- *Mie-scattering Images*

The segmentation procedure of scattering images is relatively straightforward. The algorithm, whose flowchart is schematically shown in Figure 4.2, is described below:

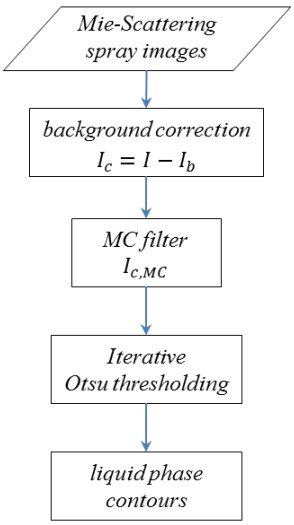

Figure 4.2 - Scattering images processing algorithm.

Background correction: before being processed, each scattering image is first corrected for the background by subtracting the image immediately preceding the fuel injection. The corrected image I_c is shown in the first row of Figure 4.3. The diagrams

on the right show the intensity profiles along the horizontal (x) and vertical (y) cross-sections of I_c indicated by the dotted red lines.

Image regularization: the corrected image is then regularized with the fast discrete filter based on minimizing the mean curvature, clipping any negative values, and obtaining the filtered image $I_{c,MC}$. The results are shown in the second row of Figure 4.3. The horizontal and vertical intensity profiles of $I_{c,MC}$ are shown on the right. As a comparison, the corresponding intensity profiles of I_c are also shown. We can see how this step effectively filters out any residual noise, preserving the sharp edges of the parent image. Even GC and TV filters could be used, but the MC filter seems to give better results for our applications.

Image segmentation: the segmentation of the image is then performed following the well-established thresholding method of Otsu [3]. The method classifies the image in the foreground and background pixels, assuming that the intensities of the two classes are distributed according to a bi-modal histogram, and finding the optimum threshold by maximizing the between-class variance. However, the method works properly if the histogram is bi-modal, showing two well defined and distinct peaks. A scattering image of a spray usually does not fulfill such requirements during all its development, and a simple application of the method tends to overestimate the threshold value and disregard significant parts of the outer edges of the spray [5]. To overcome such constraints, recursive schemes have been suggested that propose to re-threshold the pixels between the mean values of the two classes [6, 12]. We tested this approach in different experimental conditions, but the threshold value quickly decreased, thus overestimating the image foreground. Therefore, we followed a slightly different approach, applying the Otsu's method (graytresh function in MATLAB) iteratively to a new image I_i obtained by clipping the previous one I_{i-1} at the mean value $\mu_{f,i-1}$ of its foreground class, as indicated in equation 1:

$$\begin{cases} I_i = I_{i-1} \leftrightarrow I_{i-1} < \mu_{f,i-1} \\ I_i = \mu_{f,i-1} \leftrightarrow \mu_{f,i-1} < I_{i-1} \end{cases} \tag{4.21}$$

where the subscripts indicate the iteration number. In this case, for Mie-scattering images, the iteration was stopped when two consecutive threshold values differ by less than 10%, adopting this stopping criterion throughout all the tests in this work. The images in the third and fourth row of Figure 4 give a snapshot of the iterative process. The image I_2 is obtained using the mean value $\mu_{f,1}$=0.354 obtained from the threshold processing of $I_{c,MC}=I_1$. Thresholding I_2, we obtain a new threshold value T_2=0.145 and mean value of the foreground class $\mu_{f,2}$=0.275. The image I_6 is the last one to be

thresholded, before the process stops, giving the final threshold value 0.090 that will be used to segment the spray image. Finally, the image processing of Mie-Scattering images ends with their binarization and extraction of the spray boundaries, as shown in the last row of Figure 4.

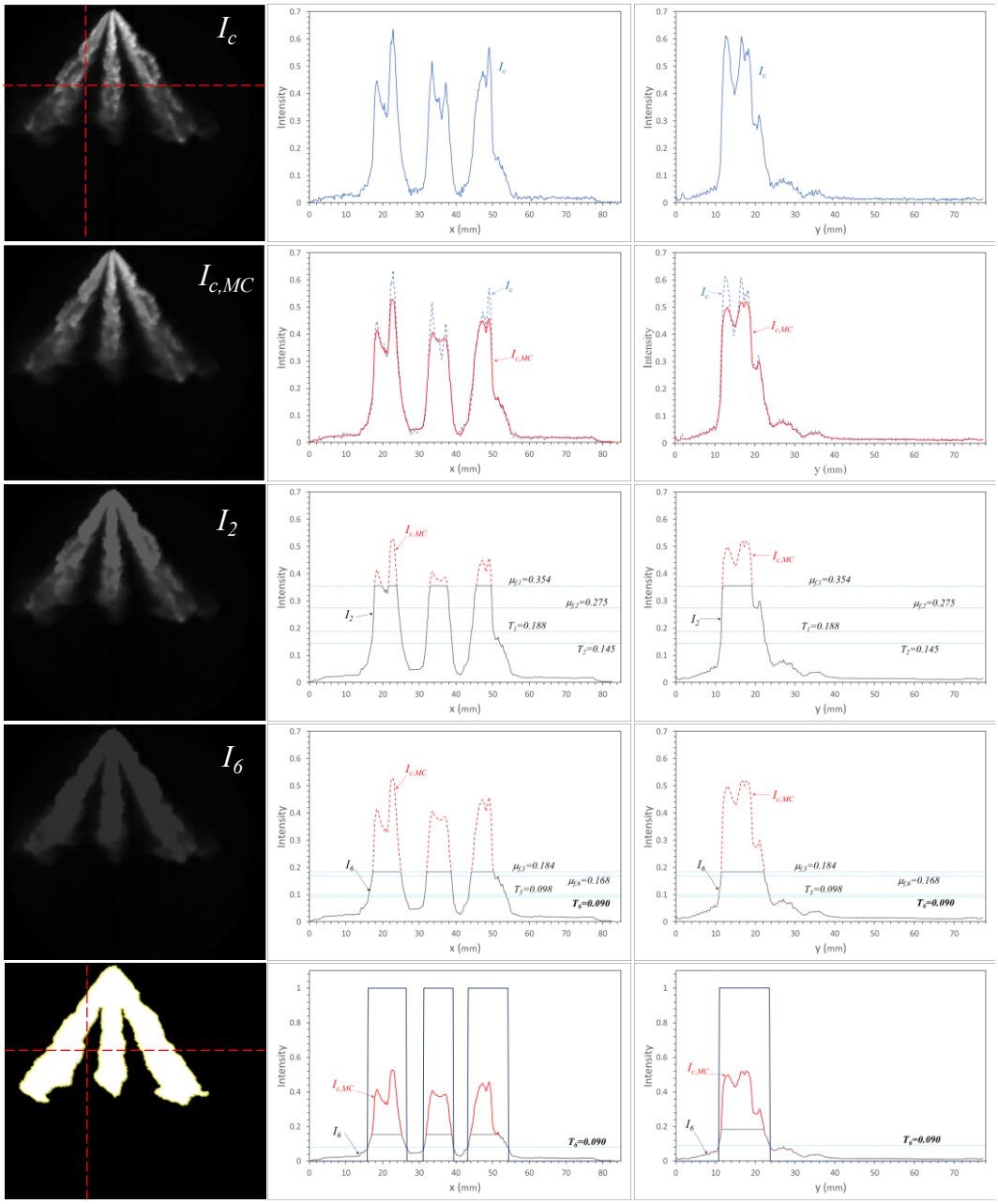

Figure 4.3 - Image processing of Mie-scattering spray images. The background-corrected image Ic is shown in the first row. The second row displays the regularized image according to the MC filter. The third and fourth raw illustrates the iterative thresholding procedure. The final step of image binarization is shown in the last row.

The threshold values and the mean values of the foreground classes obtained throughout the iterative thresholding process are shown in Figure 4.4. The intensity histograms of $I_{c,MC}$ (red bars) and I_6 (grey bars) are also shown in the log-scale diagram at the bottom. The black dotted line indicates the final threshold value.

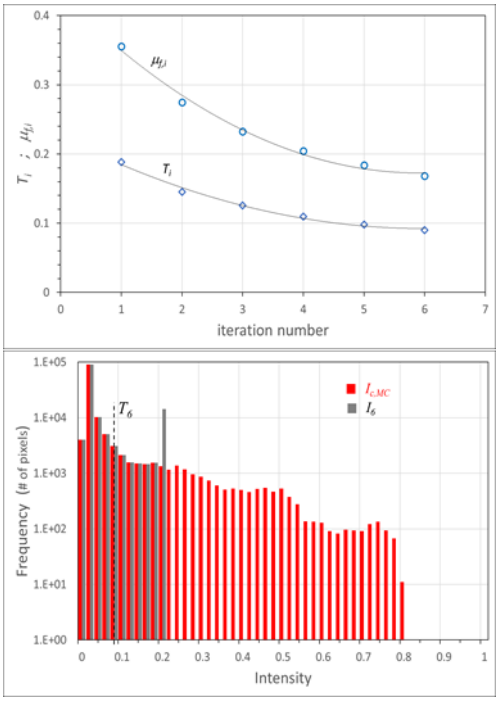

Figure 4.4 - (Top) Threshold values and mean values of the foreground classes obtained throughout the iterative thresholding process of image $I_{c,MC}$, in Figure 4.3. (Bottom) Intensity histograms of $I_{c,MC}$ (red bars), and I_6 (grey bars). The black dotted line indicates the final threshold value.

Finally, the spray contours, superimposed to its scattering image, are shown in the top and middle pictures a and b in Figure 4.5. The image in false colors helps to evaluate the result of the segmentation process. As a comparison, the spray contours were also superimposed on the corresponding schlieren image in picture c at the bottom.

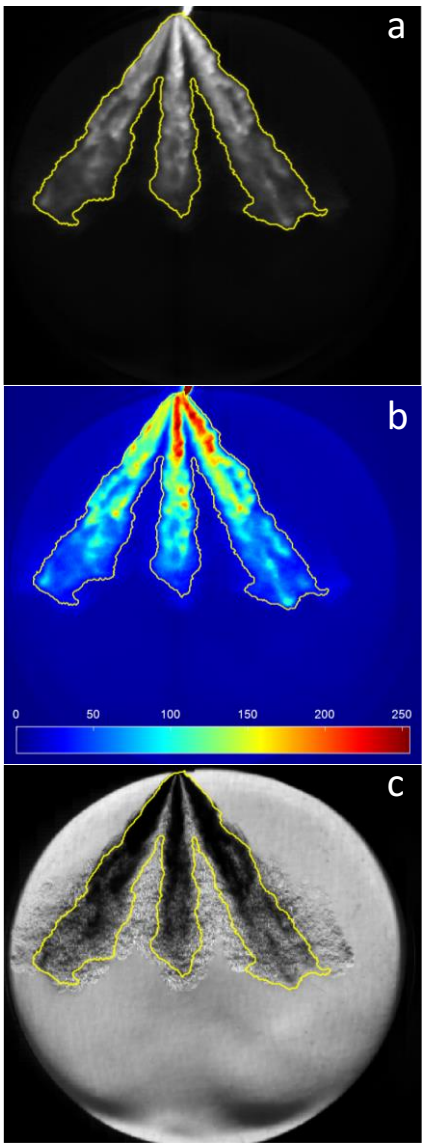

Figure 4.5 - Contours of the liquid phase of the spray obtained from its Mie-Scattering image. For comparison, in picture c, the contours have been superimposed to the corresponding Schlieren image.

As is well known, it is relatively problematic to judge the goodness of a segmentation procedure for liquid spray images [5, 11]. However, the above results seem to demonstrate the validity of the proposed method. The iterative process converges uniformly towards a reliable threshold value that takes into account almost the entire liquid phase of the spray. We want to point out that the spray contours shown in the figure are those obtained only from the process described above without any additional morphological processing (erosion, dilation, filling, etc.), or image intensity adjustments (brightness, contrast, gamma correction).

- *Schlieren Images*

The extraction of the vapor contours of a spray from its schlieren image is more challenging than to the liquid in the Mie-scattering image. The vapor phase and background intensity values are comparable, and it becomes difficult to define a precise contour of the spray vapor phase. We want to emphasize that the genesis of this work was precisely the quest for a reliable and objective method to highlight the vapor phase of a spray. Surface curvature helps us in such a task. The surface curvature as a measure of image texture has been investigated in digital image processing, where the principal curvatures of images and their linear combinations were used to infer their textural features [21]. In our processing method, the schlieren texture of the spray image has been enhanced by computing the mean of the absolute values of the principal curvatures κ_1 and κ_2 [22], as shown in equation 4.2:

$$\left|\overline{k_l}\right| = \frac{C\left(\left|k_1\right| + \left|k_2\right|\right)}{2} \tag{4.22}$$

where C (>0) is a correction factor, which depends on the experimental conditions and the intensity range of the spray image. The procedure is described in the following (Figure 4.6).

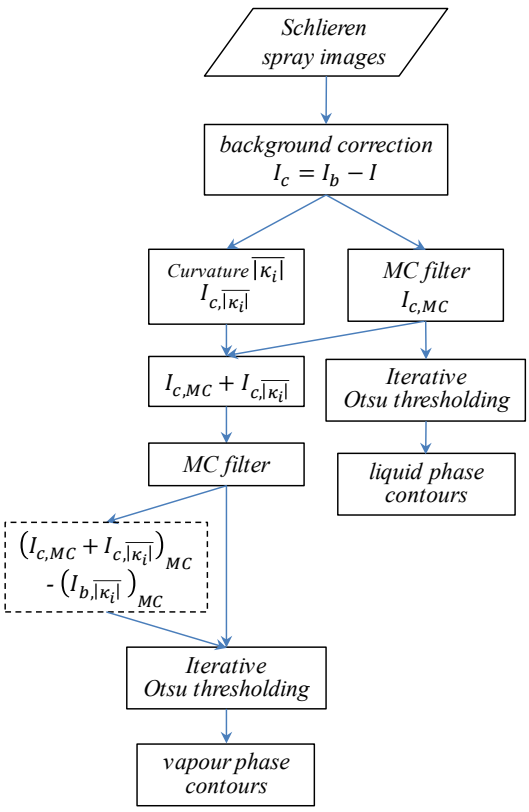

Figure 4.6 - Schlieren images processing algorithm.

Background correction: the spray image is first corrected for the background. Because of favorable experimental conditions and a slowly changing background, it was sufficient to subtract each spray image from the background image acquired just before the fuel injection. By contrast, under severe experimental conditions, such as those found in high density and temperature environments, a dynamic background correction [13, 22]may be necessary. The corrected image I_c is shown in the first row of Figure 4.7. The diagrams on the right show the intensity profiles along the horizontal and vertical cross-sections of I_c indicated by the dotted red lines. The Schlieren intensity oscillations are visible, being more extensive along the vertical direction because of the horizontal alignment of the knife edge.

Image regularization: I_c is then processed with the MC filter, smoothing the schlieren texture and obtaining the filtered image $I_{c,MC}$, which is shown in the second row of the figure.

Schlieren texture enhancement: the schlieren texture in I_c is enhanced, as described above. The principal curvatures κ_1 and κ_2 of I_c are computed as follows [22]:

$$k_1 = H - \sqrt{H^2 - K} \tag{4.23}$$

$$k_2 = H + \sqrt{H^2 - K} \tag{4.24}$$

where

$$K = k_1 k_2 = \frac{I_{xx} I_{yy} - I_{xy}^2}{\left(1 + I_x^2 + I_y^2\right)} \tag{4.25}$$

is the Gaussian curvature of I_c, and

$$H = \frac{k_1 + k_2}{2} = \frac{\left(1 + I_y^2\right) I_{xx} - 2 I_x I_y I_{xy} + \left(1 + I_x^2\right) I_{yy}}{2\left(1 + I_x^2 + I_y^2\right)^{\frac{3}{2}}} \tag{4.26}$$

is its mean curvature. The partial derivatives of the image intensities were calculated with the *gradient* function of MATLAB, using the image resolution in mm as the spacing between points. The correction factor was 1. The curvature enhanced image $I_{c,\overline{|\kappa_l|}}$ is shown in the third row of Figure 4.7. It evidences the considerable increase in the intensity of the schlieren texture due to the vapor phase of the spray compared to the liquid core of the jets. Then $I_{c,MC}$ and $I_{c,\overline{|\kappa_l|}}$ are summed, and the resulting image, zeroing any negative values, is filtered with the MC filter before being subjected to the segmentation step. The image $\left(I_{c,MC} + I_{c,\overline{|\kappa_l|}}\right)_{MC}$ so obtained is shown in the fourth row of Figure 4.7. It can appreciate how the schlieren texture, due to vapor

density gradients, is extracted out of the image background and the elusive boundaries of the vapor phase are replaced with net and well-defined edges.

The last row of Figure 4.7 illustrates an additional step of the segmentation procedure, indicated with a dotted line in the flowchart of Figure 4.6 and whose application should be assessed case by case with respect to the experimental conditions. Under harsh conditions of high gas temperature and density, the segmentation of the spray image close to the vessel surfaces could be slightly altered by the deep schlieren oscillations of intensity induced by strong thermal gradients, and the simple background correction may not be enough to guarantee a reliable result. In this case, we correct the image $\left(I_{c,MC} + I_{c,\overline{|\kappa_l|}}\right)_{MC}$ by subtracting the enhanced curvature and filtered image of the background $\left(I_{b,\overline{|\kappa_l|}}\right)_{MC}$, before proceeding to its thresholding, as clearly illustrated in the figure. We can appreciate the selective correction of the image close to the vessel surfaces. In effect, we subtract an uneven offset to the image that selectively suppresses the background noise. We applied this additional background correction in the segmentation of Schlieren spray images at the standard conditions, obtaining more than satisfying results, as it will be shown in the results section.

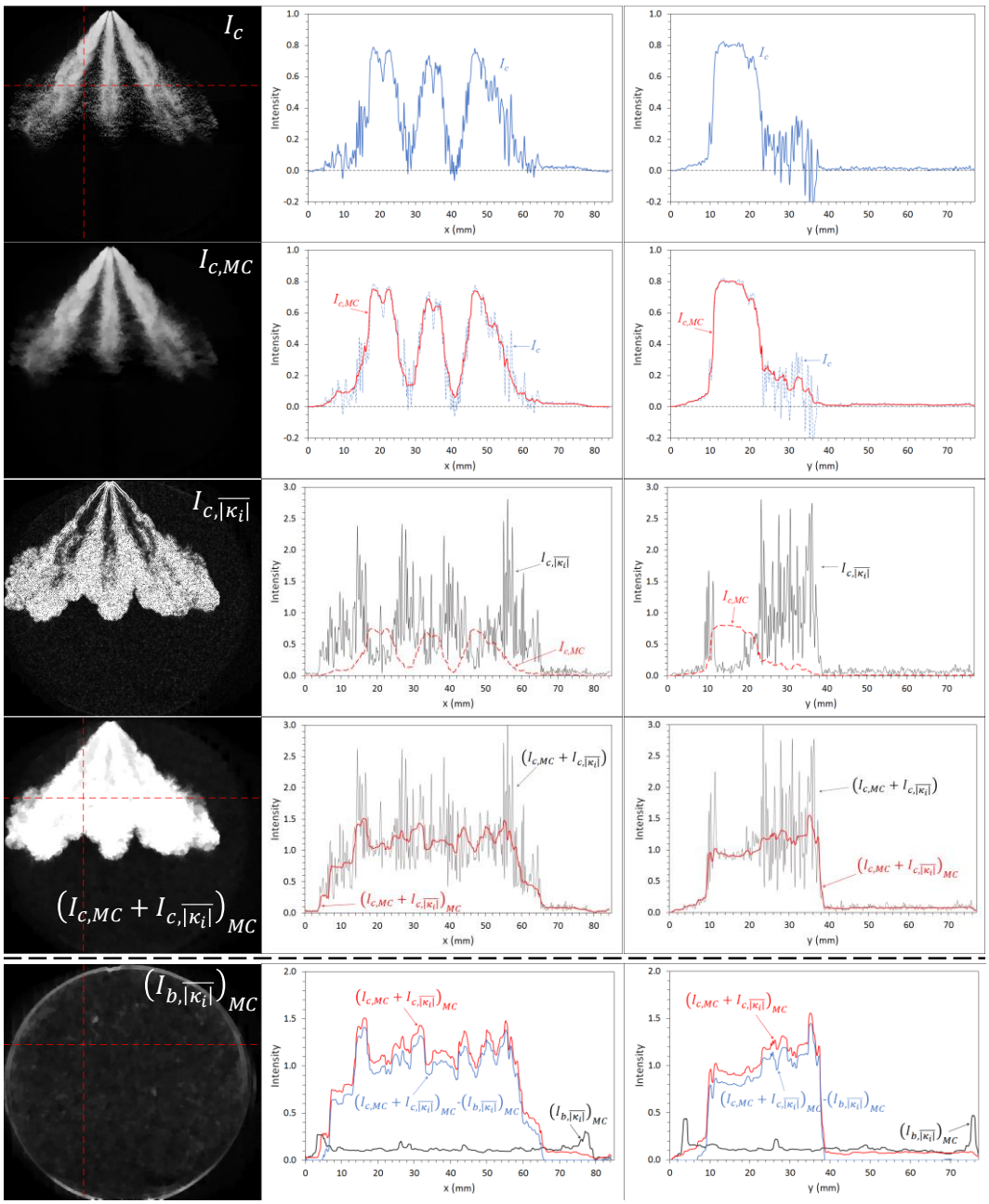

Figure 4.7 - Image processing of Schlieren spray images. The background-corrected image I_c is shown in the first row. The second row displays the regularized image according to the MC filter. The curvature enhanced image is shown in the third row, while the last row shows its sum with the regularized image.

Image segmentation: The image obtained in the previous step is clipped to 1 and thresholded iteratively to get the contours of the spray vapor phase. The iterative process, illustrated in Figure 4.8, was stopped when two consecutive threshold values differ by less than 1.0%. The image I_2 in the first row is obtained using the mean value

$\mu_{f,1}$=0.948 obtained from the threshold processing of $\left(I_{c,MC} + I_{c,\overline{|\kappa_l|}}\right)_{MC}$=$I_1$. Thresholding I_2, we obtain a new threshold value T_2=0.486 and mean value of the foreground class $\mu_{f,2}$=0.915. The image I_{36} in the second row is the last one to be thresholded, before the process stops, giving the final threshold value 0.298 that will be used to segment the spray image. Finally, the image processing of Schlieren images ends with their binarization and extraction of the vapor phase spray boundaries, as shown in the last row of Figure 4.8.

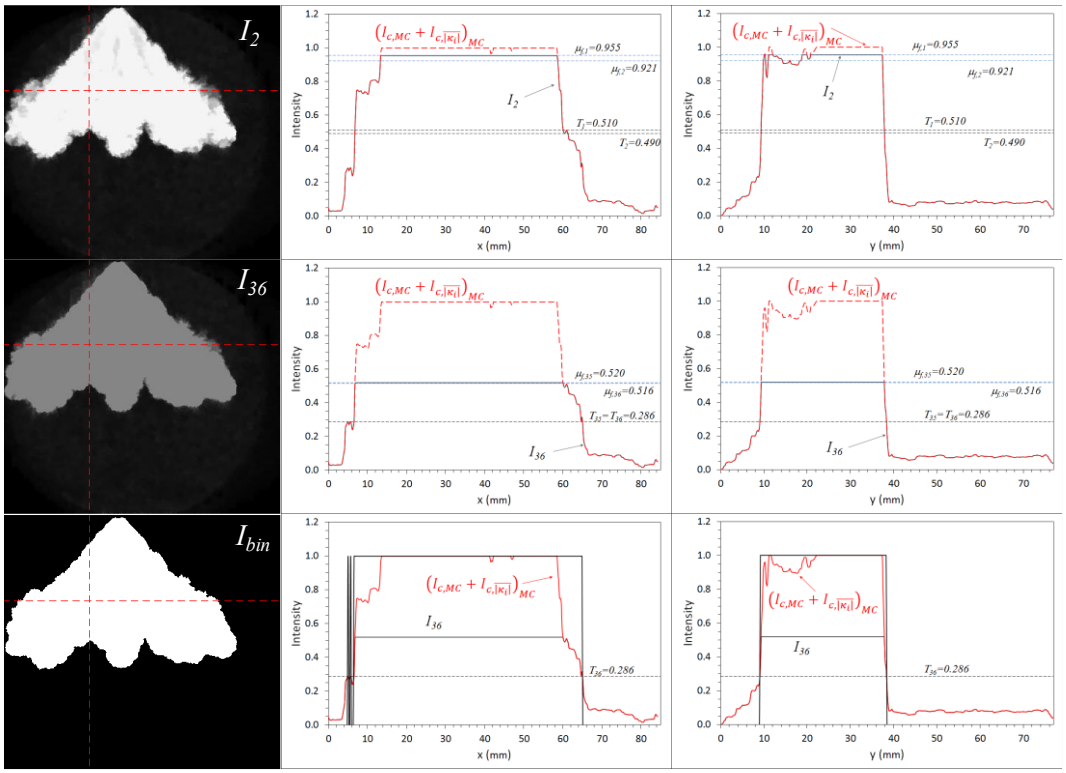

Figure 4.8 - Image processing of Schlieren spray images. The first two pictures illustrate the iterative thresholding of the curvature enhanced image. The final step of image binarization is shown in the last row.

The threshold values and the mean values of the foreground classes obtained throughout the iterative thresholding process of the Schlieren image are shown in Figure 4.9. The histograms of $\left(I_{c,MC} + I_{c,\overline{|\kappa_l|}}\right)_{MC}$ (red bars) and I_{36} (grey bars) are also shown in the log-scale diagram at the bottom.

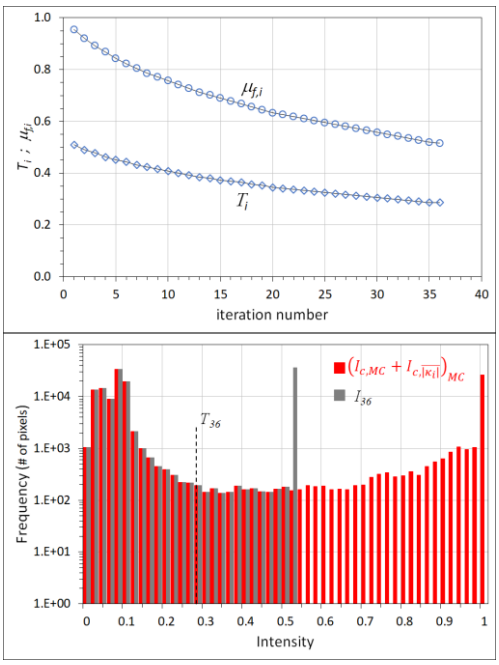

Figure 4.9 - Threshold values and mean values of the foreground classes obtained throughout the iterative thresholding process of image $\left(I_{c,MC} + I_{c,|\overline{\kappa_l}|}\right)_{MC}$ *in Figure 4.7 and Figure 4.8. (Bottom) Intensity histograms of* $\left(I_{c,MC} + I_{c,|\overline{\kappa_l}|}\right)_{MC}$ *(red bars) and* I_{36} *(grey bars). The black dotted line indicates the final threshold value.*

The contour of the vapor phase of the spray, superimposed onto its raw schlieren image, is shown in the top picture of Figure 4.10. Some enlarged zones of the spray contour are also shown in pictures a-c. Even with a qualitative analysis of the results, one can appreciate the potential of the surface curvature and of the proposed method in analyzing the schlieren structure of vapor density gradients. The iterative process converges uniformly to a constant threshold value that takes into account the whole vapor phase of the spray. Also, in this case, the spray contours shown in the figure were the net result of the process described above, without further morphological processing on the elaborated images. However, especially in the final stages of spray development, it may be needed to “clean” the image from small spurious boundaries.

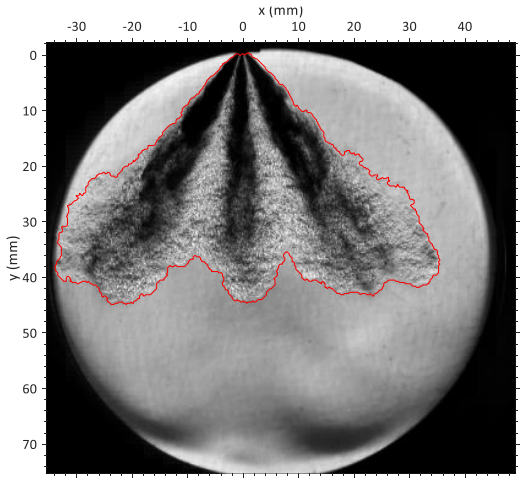

Figure 4.10 - Boundaries of the vapor phase of the spray obtained from its Schlieren image.

Spray liquid core: Looking again at the flowchart in Figure 4.6, additional information about the liquid phase of the spray can be inferred from the regularized image Ic,MC. As we can see in the second row of Figure 4.7, the MC filter smooths out the schlieren texture in the image, highlighting the light extinction profile of the spray liquid phase. Of course, it should be considered that, according to Lambert-Beer's law [24], the extincted light depends exponentially from the droplet concentration and spray width. Nevertheless, by thresholding the image Ic,MC, with the Otsu's method, we can get the contours of the spray liquid core, or rather of the spray areas with high droplet concentration. The results are shown in Figure 4.11, where the two contours of the spray liquid phase obtained from Mie-scattering (yellow lines) and Schlieren (red lines) have been superimposed to the raw images. Although the images refer to a late injection phase at a relatively low speed of the spray, we must not forget that consecutive Schlieren / Mie images are spaced by 5□s.

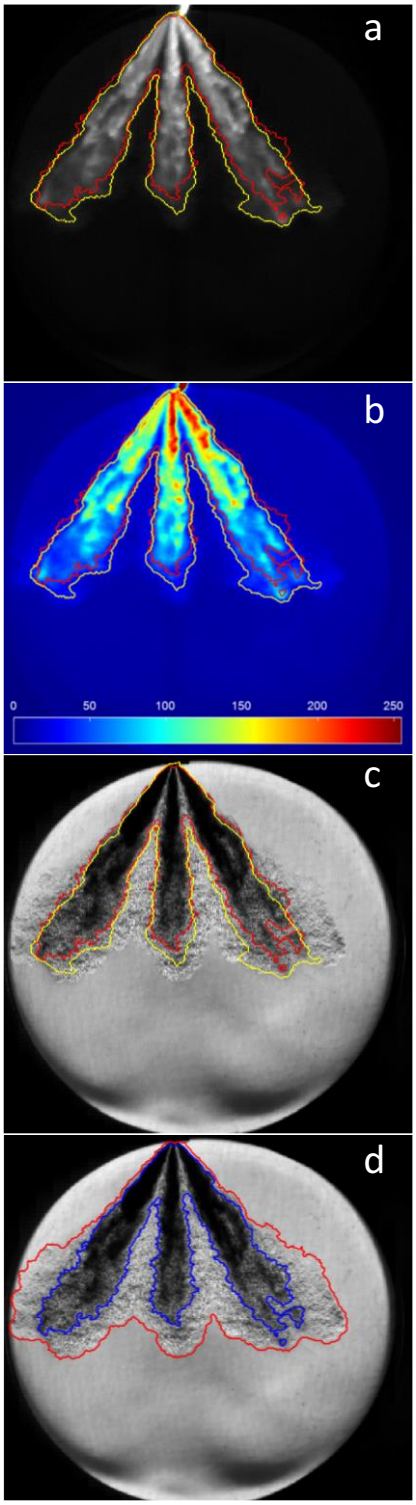

Figure 4.11 - Contours of the liquid phase obtained from Mie-scattering (yellow lines) and Schlieren (red lines) imaging superimposed to their raw images. Picture d: Comparison between the contours of liquid (blue line) and vapor (red line) phase obtained by Schlieren image.

This section ends with some additional considerations about the last steps of the segmentation procedure of schlieren spray images (image regularization and thresholding) to get the liquid phase contours. The results seem to suggest that the method could be effectively applied also in investigating the spray liquid phase by shadowgraph and, above all, DBI measurements.

The image processing procedure described above was applied to investigate the time evolution of the spray in the experimental conditions described in the experimental section. The contours of the liquid and vapor phases were determined throughout the spray development, fully highlighting the potential of the proposed method. The macroscale parameters of the spray, namely spray angle, penetration length, and spray area, have also been measured.

The results of the image processing are shown in:

- Figure 4.12 refers to the conditions with ρ_{amb}=1.12kg/m^3 and T_{amb}=333K;
- Figure 4.13 shows the results at ρ_{amb}=1.12kg/m^3 and T_{amb}=573K;
- Figure 4.14 illustrates the behavior of the spray at ρ_{amb}=3.5kg/m^3 and T_{amb}=573K.

As indicated in the "Image Processing" section, the stopping criterion for the iterative threshold of Mie-scattering images has been set to 10%. For Schlieren images, instead, it was set at 2% for ambient condition (T_{amb}=333K) images and 1% for the other two conditions, stopping the process in any case after a maximum of 40 iterations. In the first two columns of the Figure 4.12-14, the contours of the vapor (red lines) and liquid (yellow lines) phase are shown superimposed to the respective Schlieren and Mie-scattering raw images. The third column shows the scattering images in false colors that help us in evaluating the final result of the segmentation process. These pictures also highlight the uneven image intensity distribution because of the side illumination of the spray. In the fourth column, the contours of the spray liquid phase obtained from Mie-scattering and Schlieren (red lines) images are compared.

As described in the "Image Processing" section, Schlieren spray images in standard G spray conditions have been processed by applying the additional background correction. Although slowly, the background of the image changes with time and high-intensity gradients due to high density and gas temperature can affect the segmentation process. Figure 4.15 clearly illustrates the effectiveness of this additional correction, which completely suppresses any effect of the vessel surfaces. The figure refers to the Schlieren image at the high-density condition at 720μs ASOI.

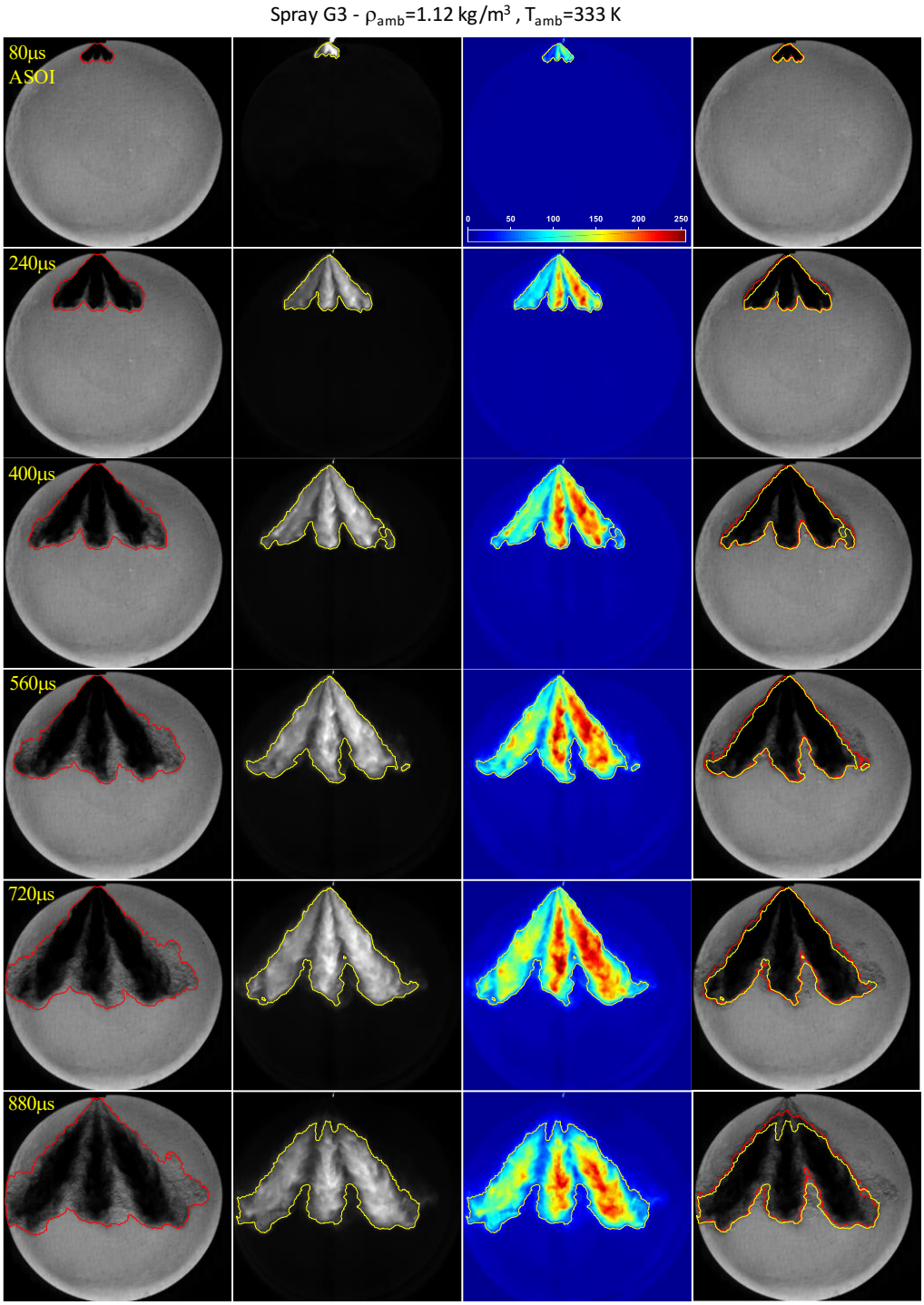

Figure 4.12 - Time evolution of Schlieren and Mie-scattering spray images and the corresponding vapor and liquid contours, under the ambient conditions. The first and second column shows the contours of the vapor phase (red lines) and the liquid phase (yellow lines) superimposed to the respective Schlieren and Mie-scattering raw images. The third column shows the Mie-scattering images in false colors with the corresponding liquid phase contours. In the last column, the latter is compared with the liquid phase contours (red lines) obtained from Schlieren images.

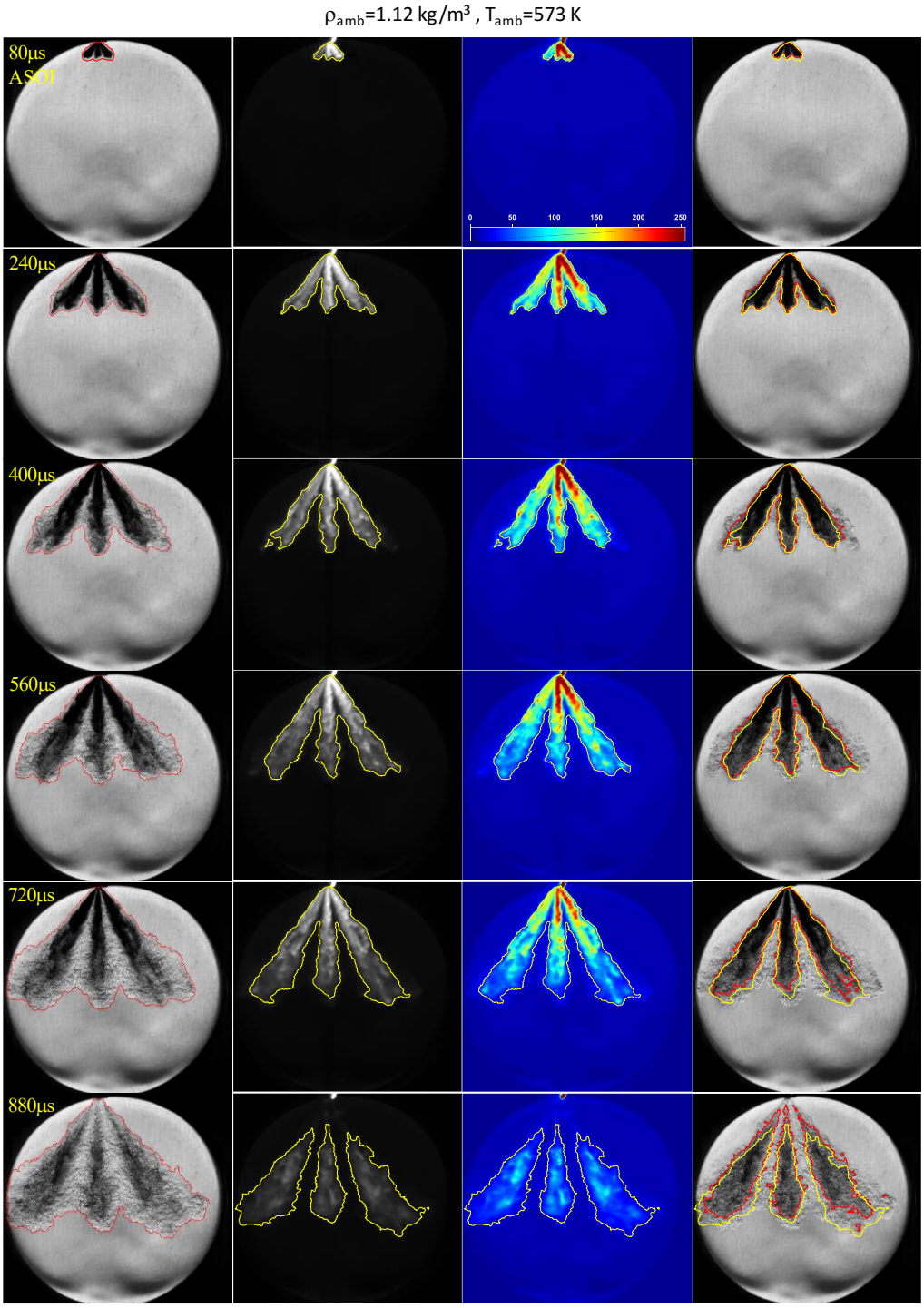

Figure 4.13 - Time evolution of Schlieren and Mie-scattering spray images and the corresponding vapor and liquid contours, under the conditions ρ_{amb}=1.12 kg/m^3 and T_{amb}=573 K The first and second column shows the contours of the vapor phase (red lines) and the liquid phase (yellow lines) superimposed to the respective Schlieren and Mie-scattering raw images. The third column shows the Mie-scattering images in false colors with the corresponding liquid phase contours. The latter are compared in the last column with the liquid phase contours (red lines) obtained from Schlieren images.

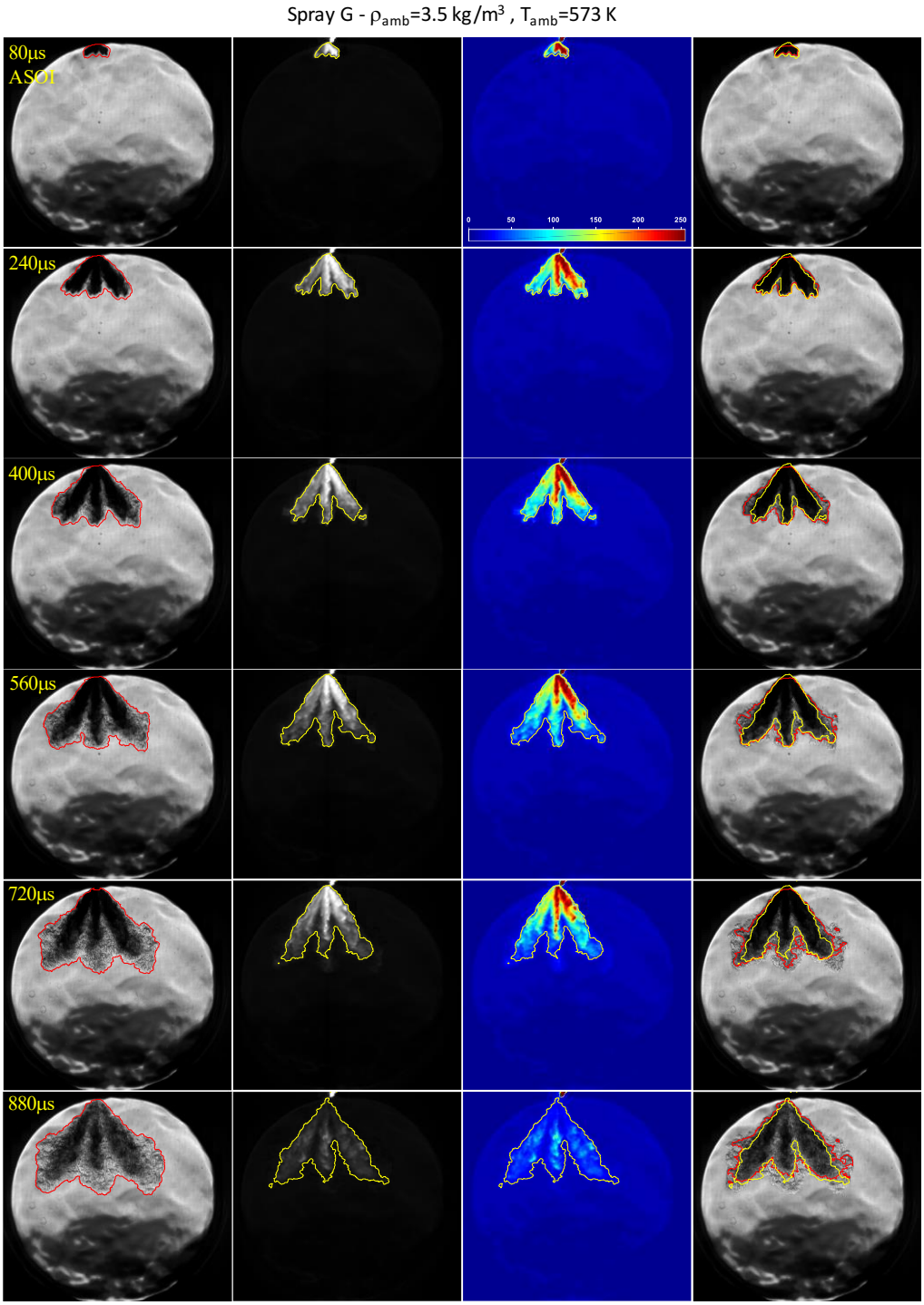

Figure 4.14 - Time evolution of Schlieren and Mie-scattering spray images and the corresponding vapor and liquid contours, at high-density conditions. The first and second column shows the contours of the vapor phase (red lines) and the liquid phase (yellow lines) superimposed to the respective Schlieren and Mie-scattering raw images. The third column shows the Mie-scattering images in false colors with the corresponding liquid phase contours. In the last column, the latter is compared with the liquid phase contours (red lines) obtained from Schlieren images.

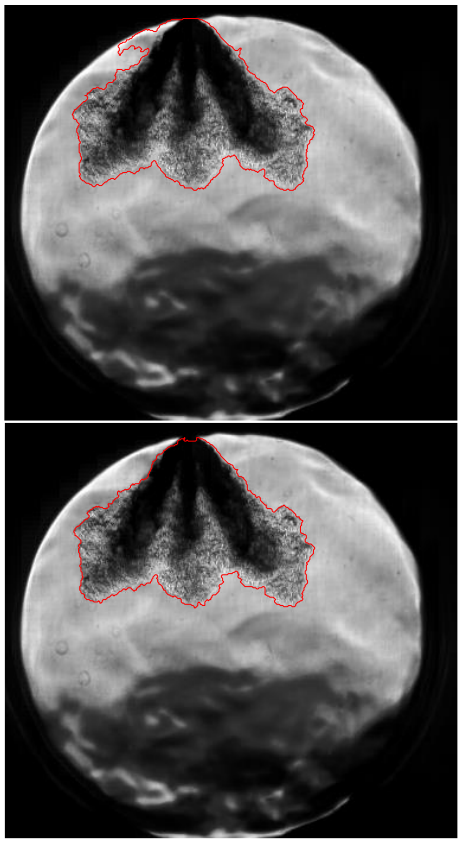

Figure 4.15 - Vapour phase boundaries of the spray, at the high-density condition and 720µs ASOI, obtained with (bottom) and without (top) applying the additional background correction.

A snapshot of the thresholding procedure and its mode of operation, referred to the image sequences shown in Figure 4.12-13, is provided by Figure 4.16, where the thresholds T_1 and T_{fin} and the mean values of the foreground classes $\mu_{f,1}$ and $\mu_{f,fin}$ versus the time ASOI have been shown for Mie-scattering images. From these pictures, we can appreciate the dynamic behavior of the iterative threshold method and the effect of fuel vaporization on the final threshold value.

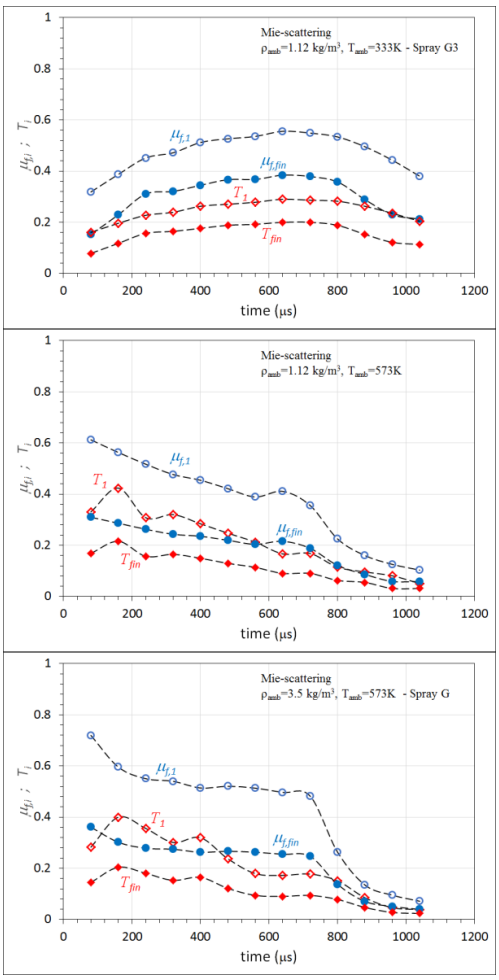

Figure 4.16 - Thresholds T_1 and T_{fin} and mean values of the foreground classes $\mu_{f,1}$ and $\mu_{f,fin}$ versus the time ASOI for Mie-scattering images.

In our opinion, the results illustrated so far clearly show that the proposed method works appropriately, allowing to efficiently segment both Schlieren and Mie-scattering images of a vaporizing GDI spray under different experimental conditions, and for the whole spray development. The segmentation of Schlieren images allows getting the whole vapor phase of the spray, highlighting the enormous potential of the surface curvature and of the proposed method in analyzing the schlieren structure of vapor density gradients. For scattering images, the iterative process provides a threshold value that takes into account almost the entire liquid phase of the spray. One cannot avoid using the term "almost". It is objectively problematic to delineate the "true" contours of the liquid phase and discern it from the image background. As previously described in the introduction section, at the outer edges of the liquid phase of a spray, the scattering volume reduces, and the droplet concentration rapidly drops; hence the intensity values of the scattering image blurs with the background. It is even

more so true towards the end of the injection of vaporizing sprays, where the small residual droplets are highly dispersed in the environment, and the scattering signal progressively vanishes. Our image processing method, through the stopping criterion adopted for the iterative thresholding, allows getting a reliable contour of the liquid phase throughout the spray development.

This section ends with the measurement of the macroscale parameters of the liquid (from Mie-scattering images) and vapor phase (from Schlieren images) of the spray, which in fact, should be the ultimate goal of such studies, whatever the image processing method. The spray penetration was calculated as the maximum axial distance of the spray contour from the injector tip. The spray angle, defined as the angle of the cone enclosing the whole spray, was measured from a linear fit through the spray outer edges, where the origin is fixed at the geometric intersection of the spray holes axes, 1.4 mm inside the injector tip [17]. For the liquid phase, the fit starts at 10% and ends at 40% of the axial penetration. For the vapor phase, the linear fit was limited at 30% of the axial penetration before the spray spreads outward [8] and no longer holds the initial conical shape. The results, shown in Figure 4.17, were obtained by averaging the results of five consecutive spray injections.

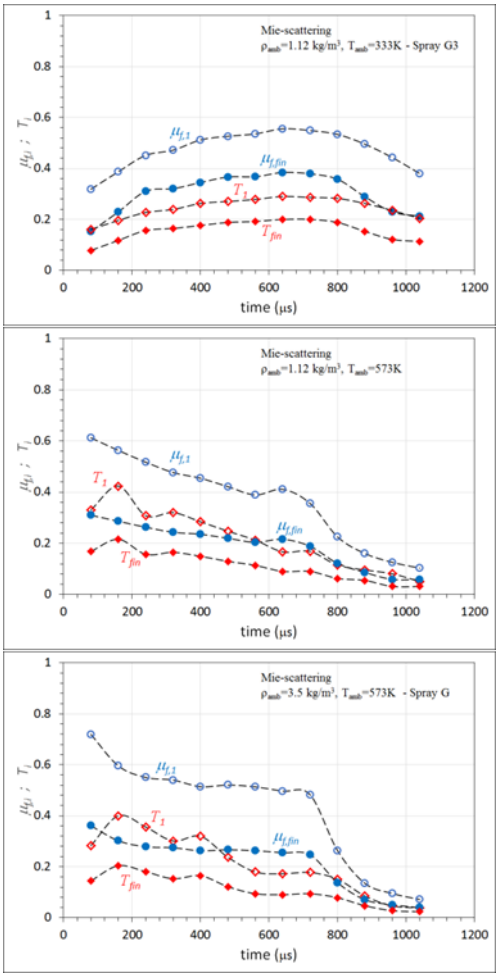

Figure 4.17 - Maximum axial penetration (top), spray angle (middle), and spray area (bottom) of the liquid and vapor phases of the spray.

The top picture shows the maximum axial penetration of the liquid and vapor phases of the spray. The different stages of spray development are identifiable [25]. Up to 300 µs, the liquid and vapor phases developed almost uniformly and grouped. Afterward, the jets progressively slow down, and the vapor front detaches from the liquid phase. The results for high-density spray show how the ambient density strongly affects the spray development. The low standard deviation of the measurements (black error bars) gives an account of their extreme repeatability.

The spray angles are shown in the middle picture. The ambient conditions slightly affect the spray angle of the liquid phase, while significant differences can be appreciated for the vapor phase as the gas density increases.

Finally, the bottom picture shows the cross-section area of the spray, meant as the area enclosed by the spray contour, giving an overall view of the spray diffusion. The curves clearly show how ambient temperature and density affect the spray

development. At ρ_{amb}=1,12 kg/cm^3, the areas of the vapor phase practically coincide, while a substantial reduction in the liquid phase area is observed as the temperature is raised to 573K. At T = 573K, increasing the gas density to 3.5 kg/m^3, the vapor and liquid phase areas decrease considerably, but their ratio is not affected at all, remaining nearly the same throughout the spray development.

REFERENCES

[1] R. C. Gonzalez and R. E. Woods, *Digital image processing Addison*. Wesley publishing company, 1992.

[2] N. R. Pal and S. K. Pal, 'A review on image segmentation techniques', *Pattern recognition*, vol. 26, no. 9, pp. 1277–1294, 1993.

[3] N. Otsu, 'A threshold selection method from gray-level histograms', *IEEE transactions on systems, man, and cybernetics*, vol. 9, no. 1, pp. 62–66, 1979.

[4] J. V. Pastor, J. Arregle, and A. Palomares, 'Diesel spray image segmentation with a likelihood ratio test', *Applied optics*, vol. 40, no. 17, pp. 2876–2885, 2001.

[5] J. V. Pastor, J. Arrègle, J. M. García, and L. D. Zapata, 'Segmentation of diesel spray images with log-likelihood ratio test algorithm for non-Gaussian distributions', *Applied optics*, vol. 46, no. 6, pp. 888–899, 2007.

[6] V. Macian, R. Payri, A. Garcia, and M. Bardi, 'Experimental evaluation of the best approach for diesel spray images segmentation', *Experimental Techniques*, vol. 36, no. 6, pp. 26–34, 2012.

[7] A. Cronhjort and F. W\a ahlin, 'Segmentation algorithm for diesel spray image analysis', *Applied optics*, vol. 43, no. 32, pp. 5971–5980, 2004.

[8] R. Payri, F. J. Salvador, P. Martí-Aldaraví, and D. Vaquerizo, 'ECN Spray G external spray visualization and spray collapse description through penetration and morphology analysis', *Applied Thermal Engineering*, vol. 112, pp. 304–316, 2017.

[9] R. Payri, J. P. Viera, V. Gopalakrishnan, and P. G. Szymkowicz, 'The effect of nozzle geometry over the evaporative spray formation for three different fuels', *Fuel*, vol. 188, pp. 645–660, 2017.

[10] R. Payri, J. Gimeno, M. Bardi, and A. H. Plazas, 'Study liquid length penetration results obtained with a direct acting piezo electric injector', *Applied Energy*, vol. 106, pp. 152–162, 2013.

[11] J. Lacey *et al.*, 'Generalizing the behavior of flash-boiling, plume interaction and spray collapse for multi-hole, direct injection', *Fuel*, vol. 200, pp. 345–356, 2017.

[12] A. Cronhjort and F. W\a ahlin, 'Segmentation algorithm for diesel spray image analysis', *Applied optics*, vol. 43, no. 32, pp. 5971–5980, 2004.

[13] Y. Ma, R. Huang, P. Deng, and S. Huang, 'The development and application of an automatic boundary segmentation methodology to evaluate the vaporizing characteristics of diesel spray under engine-like conditions', *Measurement Science and Technology*, vol. 26, no. 4, p. 045004, 2015.

[14] J. Benajes, R. Payri, M. Bardi, and P. Martí-Aldaraví, 'Experimental characterization of diesel ignition and lift-off length using a single-hole ECN injector', *Applied thermal engineering*, vol. 58, no. 1–2, pp. 554–563, 2013.

[15] O. Scherzer, M. Grasmair, H. Grossauer, M. Haltmeier, and F. Lenzen, *Variational methods in imaging*. Springer, 2009.

[16] L. A. Vese and C. Le Guyader, *Variational methods in image processing*. CRC Press, 2015.

[17] Y. Gong, 'Spectrally regularized surfaces', PhD Thesis, ETH Zurich, 2015.

[18] Y. Gong and I. F. Sbalzarini, 'Curvature filters efficiently reduce certain variational energies', *IEEE Transactions on Image Processing*, vol. 26, no. 4, pp. 1786–1798, 2017.

[19] G. Paul, J. Cardinale, and I. F. Sbalzarini, 'Coupling image restoration and segmentation: a generalized linear model/Bregman perspective', *International journal of computer vision*, vol. 104, no. 1, pp. 69–93, 2013.

[20] *http://mosaic.mpi-cbg.de/?q=downloads/curvaturefilters*. .

[21] F. Peet and T. Sahota, 'Surface curvature as a measure of image texture', *IEEE transactions on pattern analysis and machine intelligence*, no. 6, pp. 734–738, 1985.

[22] A. Gray, E. Abbena, S. Salamon, and others, 'Modern differential geometry of curves and surfaces with Mathematica', 2006.

[23] L. M. Pickett, S. Kook, and T. C. Williams, 'Visualization of diesel spray penetration, cool-flame, ignition, high-temperature combustion, and soot formation using high-speed imaging', *SAE international journal of engines*, vol. 2, no. 1, pp. 439–459, 2009.

[24] C. F. Bohren and D. R. Huffman, *Absorption and scattering of light by small particles*. John Wiley & Sons, 2008.

[25] S. E. Parrish, 'Evaluation of liquid and vapor penetration of sprays from a multi-hole gasoline fuel injector operating under engine-like conditions', *SAE International Journal of Engines*, vol. 7, no. 2, pp. 1017–1033, 2014.

[26] J. Manin, Y. Jung, S. A. Skeen, L. M. Pickett, S. E. Parrish, and L. Markle, 'Experimental characterization of DI gasoline injection processes', SAE Technical Paper, 201

CHAPTER 5 HOLLOW-CONE NOZZLES CHARACTERIZATION

Reference: "Outward-Opening Hollow-Cone Spray Characterization by Experimental and Numerical Approach in Evaporative and Non-Evaporative Conditions[3]"; "Outwardly Opening Hollow-Cone Diesel Spray Characterization under Different Ambient Conditions[4]".

5.1 Introduction

The injection system of direct injection (DI) diesel engines has an essential role regarding the fulfillment of demands for low pollutant emissions and high engine efficiency. One of the injection system parameters affecting fuel spray characteristics, fuel-air mixing, and consequently, combustion and pollutant formation is the geometry of the nozzle hole [1-3]. In particular, the main physical processes defining the atomization capabilities of diesel injectors can be associated with the cavitation and turbulence conditions characterizing the nozzle flow. Design parameters like hole diameter, hydro grinding, conicity, or inlet hole radius have shown a direct influence on the internal hydraulic flow, allowing a better trade-off between high performances and emissions.

For this reason, in-depth knowledge of how injector geometry influences the emerging spray is a mandatory task. Alternative spray concepts to the conventional Multi-Hole Nozzles (MHN) could be considered as solutions to the extremely high injection pressures increase to assure a high and faster fuel-air mixing in the piston bowl, with the final target of increasing the fuel efficiency and reducing engine emissions [4, 5]. In this scenario, the Hollow Cone Nozzle (HCN) injector concept could theoretically be an attractive solution to meet these targets. The basic idea is to increase the radial fuel distribution by using a 360-degree delivery area. Pressure-

[3] https://doi.org/10.4271/2017-24-0108;

[4] https://doi.org/10.4271/2018-01-1694.

swirling and inwardly-opening hollow-cone spray injectors have been commonly utilized in gasoline direct injection (GDI) and gasoline compression ignition (GCI) engines due to its efficient atomization with relatively wide spray angle and fine atomization [6, 7]. GCI engines, in general, operate at low-temperature combustion (LTC) conditions that have been gaining increasing attention over the last decade due to its potential of achieving diesel-like thermal efficiencies with significantly reduced engine-out nitrogen oxides (NOx) and soot emissions [8–10]. Recently, the outwardly-opening piezo-electric injector is gaining popularity as a high efficient hollow-cone spray injector due to its precise control of the spray by an accurate piezoelectric actuator. Briefly, the piezo injector has a more extensive linear working flow range, higher static flow rate, the capability of rapid multiple-pulsing producing closely spaced multiple injection events, can inject minimal quantities precisely, has the potential of variable needle-lift, and because of its outwardly-opening poppet design is deemed more resistant to fouling.

Further, the spray produced by a piezo injector is typically better atomized, less penetrating, and produces a more compact mixture cloud [11]–[13]. Different authors analyzed the spray of this kind of injector in the past but concentrated mainly on the studies on GDI injectors types. This work aims to study morphology as well as the stability of these sprays types at high injection pressures, typical of diesel applications. These results could be useful for studying, in the further steps, the injector behavior and performances in research engines to evaluate potentiality and critical aspects for real application in diesel combustion systems.

5.2 Hydraulic characterization HCN

The HCN prototype injector is hydraulically characterized by an AVL fuel injection rate meter working on the Bosch tube principle (chapter 3), at different injection pressures, injection durations, and voltage command.

The total amount of injected fuel mass is derived by the pressure signal in the Bosch tube [14, 15], and is proportional to the injection rate through geometrical parameters of the apparatus and chemical-physical properties of the fluid [16]. The measurements are averaged over one hundred shots, and the dispersion is restrained in less than 2%. The results are compared with that pounded at the Bosch tube discharge by a precision balance. Table 5.1 reports the experimental conditions carried out in order to characterize the mass flow rate, for two different voltage command 110, and 150V, different injection pressures, 30, 80, 120, and 160 MPa, with a different energizing

time. The signals are averaged on one hundred shots to reduce the white noise. As discussed previously, the hydraulic characterization was carried out only for the HCN; therefore, the results will refer only to the injector just mentioned.

Table 5.1 – Experimental conditions.

Voltage [V]	110	150
p_{inj} [MPa]	30-80-120-160	30-80-120-160
ET [ms]	0.3-0.5-0.7-1.25-1.5	0.3-0.5-0.7-1-1.25-1.5
P_{back} [MPa]	5	5
Fuel	Diesel	Diesel
T_{fuel} [K]	298	298
a_{fuel} [m/s]	1323	1323

The imposed backpressure was 5 MPa for all test points in order to simulate the main injection condition in the combustion chamber. The fuel used was commercial diesel; the fuel's characteristics were illustrated in chapter 3.

5.2.1 Supply Voltage Effect

In the following paragraph, the effect of different supply voltage was analyzed to characterize the injector hydraulic behavior.

Figure 5.1 shows the relationship between the voltage command and the corresponding injection rate at 80 MPa. The typical shape of injector energizing voltage has been observed, assuming a typical step pattern, with an almost impulsive rate for opening/closing.

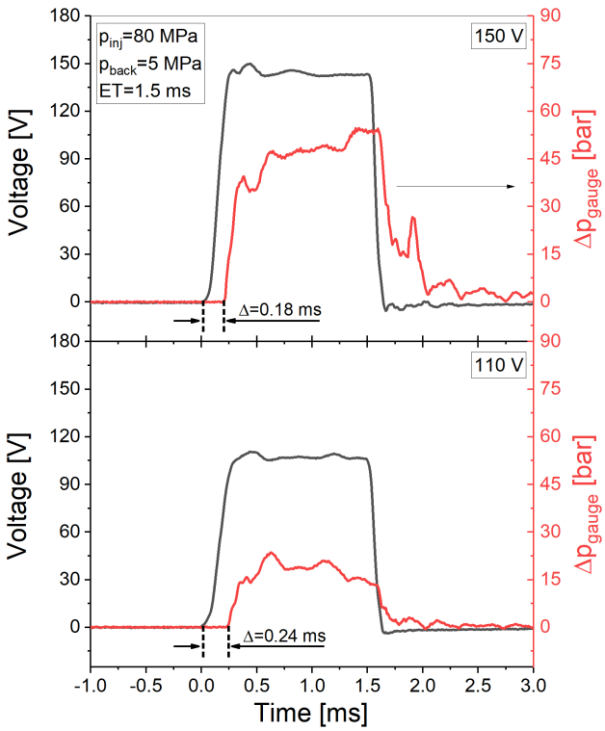

Figure 5.1 - Voltage command (black) and corresponding fuel injection rate (red) at the same p_{inj} (80MPa), ET (1.5ms), and p_{back} (5MPa), at different supply voltage 150V (a) and 110V (b).

The fuel mass rate shows a not progressive lifting of the needle during the opening stroke, as well as to pulsating effects of the flow rate before reaching a quasi-steady condition (150 V, Figure 5.1a), while at 110 V (Figure 5.1b) an almost constant trend is observed. A quick increase of signal is recorded at the start, obviously more evident in the first one. The needle is rapidly raised due to the excitation of piezoelectric, and a strong increase in the flow area is obtained. A hydraulic delay, proportional to the voltage, of around 0.18 ms for 150 V and 0.24 ms for 110 V was shown. The difference was also detected in spray imaging.

A non-perfect closure of the needle around 1.8 ms there was highlighted; in fact, a re-opening is observed. This behavior was not detected at a lower voltage (110V). The hydraulic durations, with an energizing time of 1.5 ms, between the two different test points, are 1.56, and 1.59 ms, respectively, for 110 and 150V.

5.2.2 Injection Rate Measurements

ROI profiles of diesel fuels for the energizing injection time of 1.25 ms at the injection pressures of 30, 80, 120, and 160 MPa, at the same voltage command 150 V are shown in Figure 5.2. For the sake of brevity, low voltage profiles (110 V) are not displayed because they show the same trends.

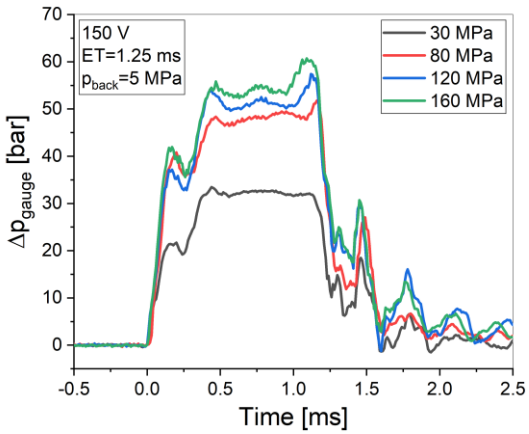

Figure 5.2 - Rate of injection profiles at injection pressures of 30, 80, 120, and 160 MPa; energizing time of 1.25 ms, voltage command 150 V, and back-pressure 5 MPa.

The curves trend for the pressures is similar, all along with their time duration. The profiles depict just a slower outflow of fuel during the first instants at the lowest injection pressure (30 MPa) to the other three conditions. Moreover, in each condition, a first relative injection rate peak is observable about 0.15-0.2 ms after the start of injection. Such an effect could be related to a not progressive lifting of the needle during the opening stroke, as well as to pulsating effects of the flow rate before reaching a quasi-steady condition. Thanks to only on the modeling and simulation of the flow inside the injector could permit a more detailed analysis of this behavior. The injection rates continue to increase up to the needle and reach its maximum lift around 0.4 ms, hereafter they reach a quasi-stable value. The different plateau levels give the reason for the diverse injection pressures, while negligible differences in closures time are registered for the profiles. The corresponding actual injection durations are approximately 1.3 ms for all the injection pressures. A reopening of the injector is observed after the closure, proportional to the injection pressure. This behavior was also detected in the spray imaging due to the rebounding of the pintle.

The total injected mass registered a well-scaled behavior with regards to the different injection pressures varying between 40.6 up to 69.4 mm^3/stroke at 30 and 160 MPa, respectively. At the end of injection, damped oscillations are registered because of fluid-dynamic effects in the Bosch tube.

Table 5.2 - Injected fuel mass [mm³/stroke] for different injection pressures, timing, and voltage command, 150 V (a), and 110 V (b).

a)

		p_{inj}			
		30 MPa	**80 MPa**	**120 MPa**	**160 MPa**
ET	**0.3 ms**	5.5	9.8	10.2	11.8
	0.5 ms	12.1	19.7	21.7	22.3
	0.7 ms	21.0	31.1	34.1	34.6
	1.0 ms	31.3	47.6	50.6	51.8
	1.25 ms	40.6	61.2	65.6	69.4
	1.5 ms	52.2	77.1	81.1	80.6

b)

		p_{inj}			
		30 MPa	**80 MPa**	**120 MPa**	**160 MPa**
ET	**0.3 ms**	1.6	2.9	3.6	4.1
	0.5 ms	8.2	12.3	13.7	15.3
	1.25 ms	16.4	23.5	27.1	29.4
	1.5 ms	19.4	27.5	30.6	31.4

In Table 5.2, the total amount of injected fuel is reported for all the investigated conditions. The injection system showed stable and repetitive behavior for a range of injected fuel mass from approximately 1.6 to 80.6 mm³/stroke. A general trend of increasing quantities was observed versus the increase in injection pressure and timing.

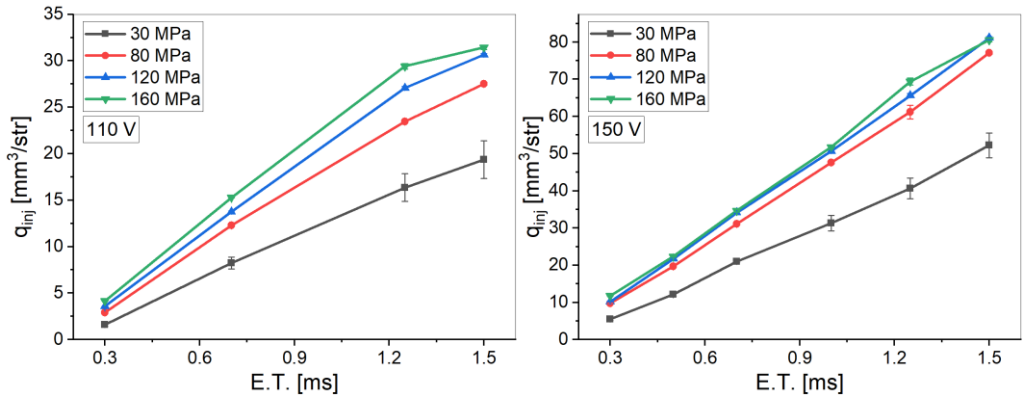

Figure 5.3 - Total amount of injected fuel vs. time for different injection pressures and voltage command.

Figure 5.3 reports the total amount of injected fuel and the relative standard deviation for different injection duration and voltage command at the explored

injection pressures. The curves show a quite linear increment to time and a well-scaled behavior with the injection pressure. The small error bars, representative of the standard deviation calculated to the average value, denote a stable and repetitive performance of the injection system for the range of injected fuel mass.

5.3 Spray Characterization

The tests were performed in a high-pressure constant volume vessel, optically accessible through three quartz windows 80 mm in diameter. As introduced previously, the activities were focused on characterizing outwardly opening pintle-type nozzles. A mono-component fuel, n-heptane (C_7H_{16}), was chosen to ensure a full knowledge of chemical proprieties and thermodynamics transitions realized during the mixture/combustion process and assuring repeatability of the processes.

The experimental characterization of the HCN was carried out under evaporative and non-evaporative conditions injecting the fuel in order to measure the spatial and temporal spray pattern at engine-like gas densities. The tests were carried out at the injection pressures (p_{inj}) of 80 and 120 MPa, ambient density (ρ_{gas}) 14.8 kg/m^3 and for two ambient temperatures (T_{amb}) 298 and 560 K. Sulfur hexafluoride (SF_6) was used to achieve the desired air densities according to the different ambient temperatures, 0.25 MPa @298K, and 0.47 MPa @560K, respectively. Five consecutive events were acquired for each injection condition for an evaluation of the standard deviation. The main specifications of the tested conditions are summarized in Table 5.3.

Table 5.3 -Experimental conditions HCN.

p_{inj} [MPa]	80-120
ET [ms]	1.25
Inj. Fuel [mm^3/str]	60
T_{amb} [K]	298-560
P_{gas} (SF_6) [kg/m^3]	14.8
p (SF6) [MPa]	0.25@298K and 0.47@560K
Fuel	n-heptane
Voltage [V]	150

The spray evolution was characterized by employing two optical techniques, Mie scattering, and schlieren. Schlieren images take into account of both liquid and vapor fraction of the spray, while the scattered light is mostly due to the liquid fraction. The optical setup is schematically shown in Figure 3.6. The images were processed through

a customized procedure developed in MATLAB (CHAPTER 4) to better outline the contours of the liquid phase and the vapor/atomized zone. The backgrounds of schlieren images at high density and temperature because of the convective phenomena observed were changed in order to highlight the spray behavior better, in Figure 5.4, is shown an example.

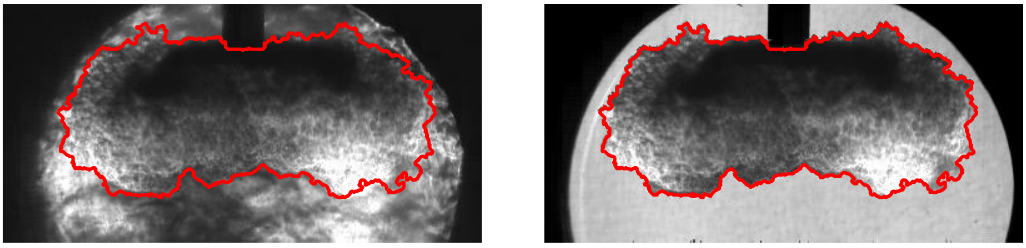

Figure 5.4 - Example background image schlieren modified.

The main macroscopic parameters employed to characterize the liquid and vapor phases development were axial (a) and radial (r) penetration versus the time from the start of injection as the maximum elongation in the vertical and horizontal direction, respectively (Figure 5.5).

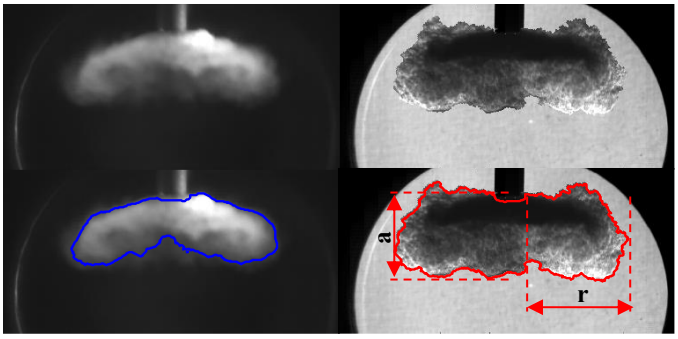

Figure 5.5 - Image processing with outlines of liquid (Mie scattering on the left) and vapor (schlieren on the right) phases. Definition of axial (a) and radial (r) penetration.

It is important to point out that the experimental characterization of all prototypes was also carried out under the non-evaporative condition at engine-like gas densities. The configurations used are shown in Figure 3.7. The tests were performed at the injection pressure (p_{inj}) of 80 MPa, ambient density (ρ_{gas}) 14.8 kg/m^3, and ambient temperature (T_{amb}) 298 K.

The injector, housed in the holder (1), was allocated in one of the optical access of the vessel chamber while the high-speed C-Mos camera and the enlightening high-intensity flash lamp (3) completed the Mie-scattering configuration for capturing, in a synchronized way, the images of the developing jet. For each layout (Figure 3.7), the acquired image of the spray is shown on the right for each injector. The HCN-8J was only characterized using frontal configuration, Figure 5.6.

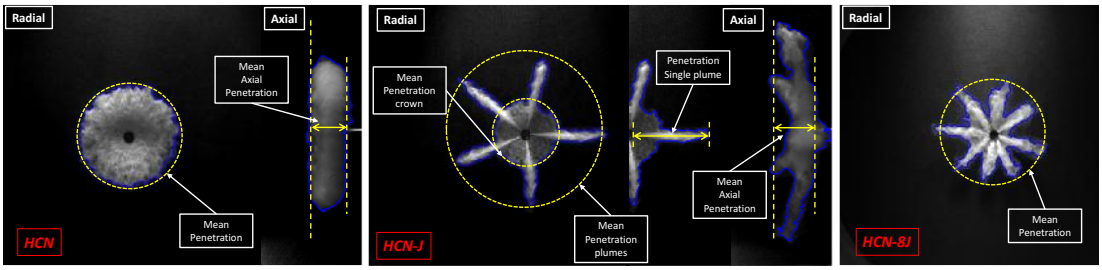

Figure 5.6 - Image processing with outlines of liquid phase(Mie scattering) for both injectors HCN (left), HCN-J (center), and HCN-8J (right). Definition of axial (a) and radial (r) penetration.

The main macroscopic parameters employed to characterize the spray development were axial (a) and radial (r) penetration. For the HCN-J, in addition to the above-mentioned global penetrations defined by the mean distance from the reference (nozzle exit), the single plumes were also characterized in terms of radial penetration. The parameters are shown in Figure 5.6, in the two configurations employed, except for the HCN-8J.

5.3.1 Voltage command effect

In this section, the voltage command was changed to analyze and compare the specific influence of the actuating variable on the nozzle exit flow. The main characteristics describing the development of the liquid phase will be shown for non-evaporative (T_{amb} 298 K) conditions, at the same density (ρ 14.8 kg/m^3), injection pressure (p_{inj} 80 MPa), and energizing time (ET 1.25 ms). This effect was evaluated for both injectors using only the Mie-scattering technique, and the experimental layout is shown in Figure 3.7.

The images obtained with two different experimental configurations from the Mie-scattering test for a case with an injection pressure of 80 MPa and vessel conditions of 14.8 kg/m^3 and 298 K are shown in Figure 5.7 at different voltage command for both injectors. For either prototype, the tests at 150 V show higher penetration values in both development spray directions. It is consistent with the higher instantaneous mass flow delivered, as already highlighted in the previous paragraph. From the HCN spray

images at the transition phase, it is evident that the emerging annular liquid jet is somewhat regular, reaching a quasi-equal penetration in the axial direction at the spray front.

Concerning HCN-J, a different shape is observed in the function of the different voltage commands. The crowns developed between the jets remain almost uniform, while the jets have a completely different shape. At 110 V, the top of the plume assumes a cusp-shaped, unlike the typical rounded shape.

The spray sequences for HCN-8J in Figure 5.7c show a partial sample of the spray structure, frontally-acquired, with the fuel freeze at different times from the start of injection. Images collected to the injector show is almost insensitive to the different supply voltage, in terms of spray shape. Only a front of the jets that are more uniform due to the higher voltage condition can be seen. A small crown is also observed around the nozzle, similar to that of the HCN-J but less evident, mainly due to the geometry of the nozzle.

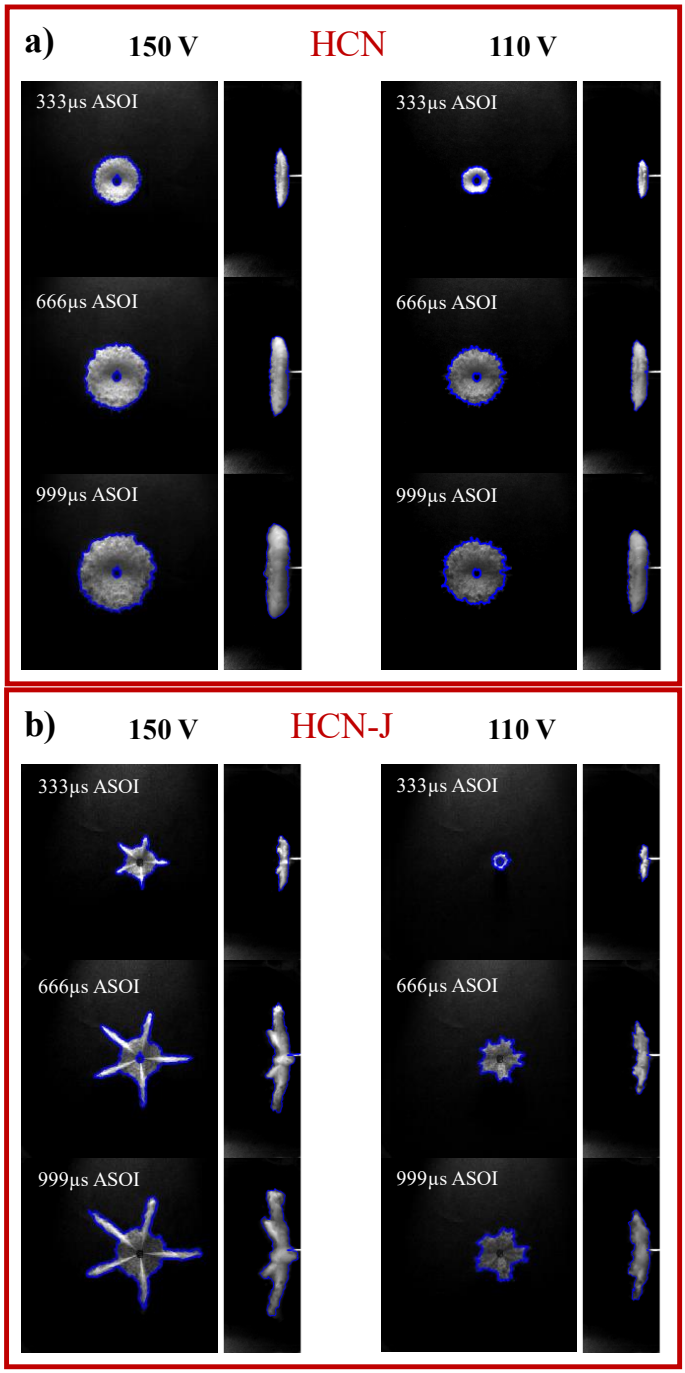
a)
150 V
HCN
110 V
333µs ASOI
666µs ASOI
999µs ASOI
333µs ASOI
666µs ASOI
999µs ASOI
b)
150 V
HCN-J
110 V
333µs ASOI
666µs ASOI
999µs ASOI
333µs ASOI
666µs ASOI
999µs ASOI

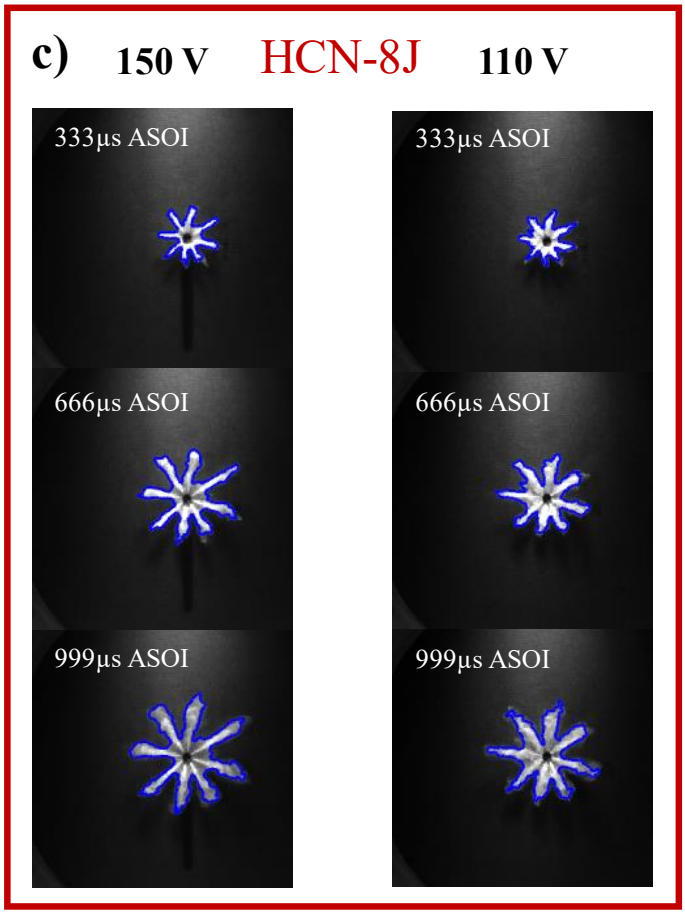

Figure 5.7 - Liquid spray evolution for both configurations frontal (left) and lateral (right), p_{inj}: 80 MPa, T_{amb}: 298 K, at different voltage command. HCN (a), HCN-J (b), and HCN-8J (c) in the only frontal configuration.

Figure 5.8 shows the post-processed values of HCN spray penetrations, illustrated in Figure 5.7. The spray evolution was measured on both sides, and the average value was calculated for the five repetitions at each injection timing. The axial penetration (Figure 5.8b) has a significant change of slope after around 200 µs. It is linked to different injection rates (Figure 5.8d). The difference remains constant for all injection events. While radial penetration (Figure 5.8a) is sensible to the voltage variation, it has a significant change of slope from the first instants. To better understand the injector behavior, the penetration ratio is shown in figure Figure 5.8c. In the transition phase, until 300 µs, the radial penetration ratio has an opposite trend than to the axial one. It is evident how the radial tip depends mainly on the different voltage commands and less sensitive to different needle lift, while the axial penetration depends only on the second one. At the regime, the ratio is proportional to the fuel injection rate trend.

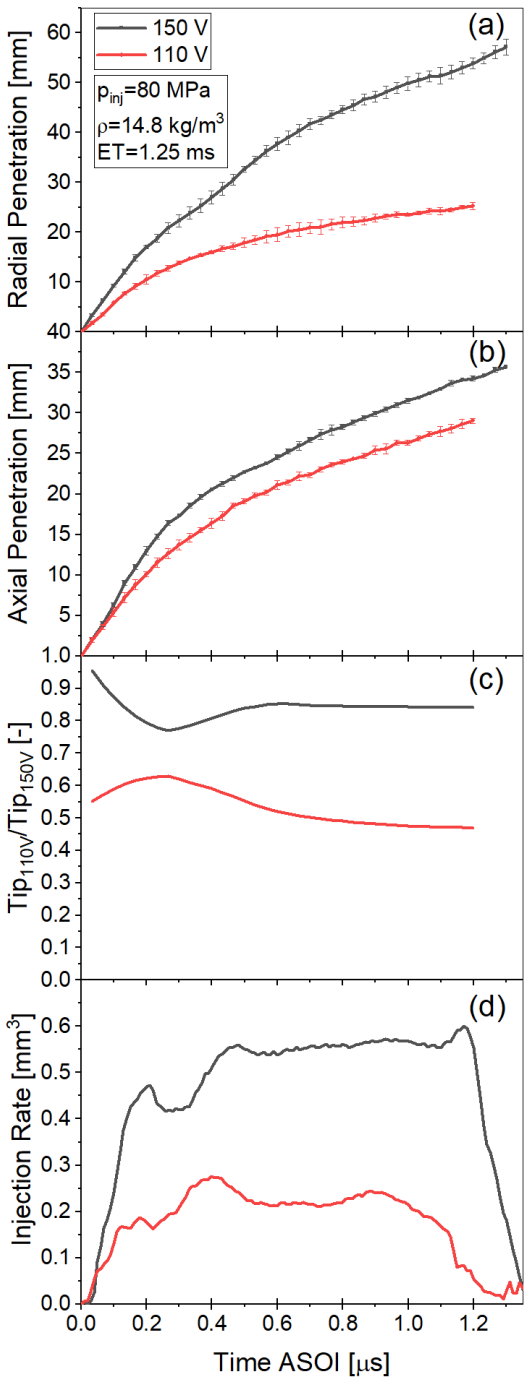

Figure 5.8 - Comparison of spray radial penetration (a), axial penetration (b), the penetration ratio (c), and fuel injection rate (d) at different voltage commands for HCN. P_{inj} 80 MPa; ρ 14.8 kg/m^3; T_{amb} 298 K.

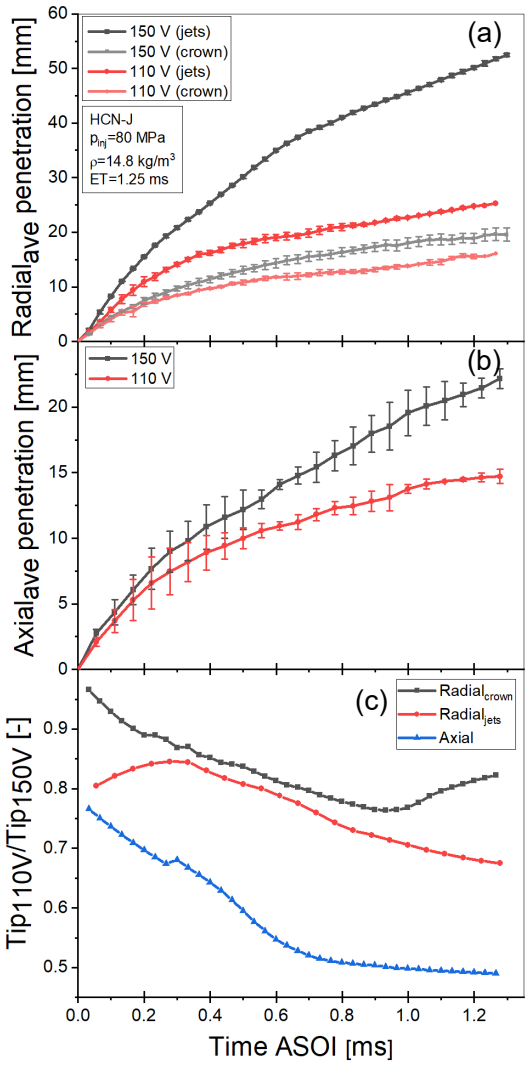

Figure 5.9 – Comparison of spray radial penetration (a), axial penetration (b), the penetration ratio (c) at different voltage commands for HCN-J. P_{inj} 80 MPa; ρ 14.8 kg/m³; T_{amb} 298 K.

Figure 5.9 depicts the liquid trends as a function of the voltage command for HCN-J injector at ambient temperature (298 K) at an injection pressure of 80 MPa. As regards the axial propagation (Figure 5.9b), the profiles overlap up to around 0.4 ms, indicating a negligible effect of voltage command at the early stages. Later, at the highest voltage, the penetration is longer than that corresponding to the lower one. Similar behavior also for the crown radial penetration (Figure 5.9a). The effect is not visible until about 0.2 ms, to then have a constant gap throughout the injection event. The radial penetration of the jets has a similar behavior of HCN (Figure 5.8a), with a divergent trend from the first instants.

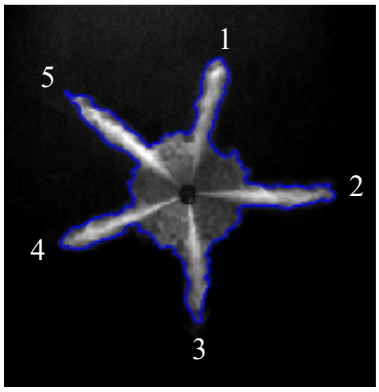

Figure 5.10 – Progressive numbering spray plumes.

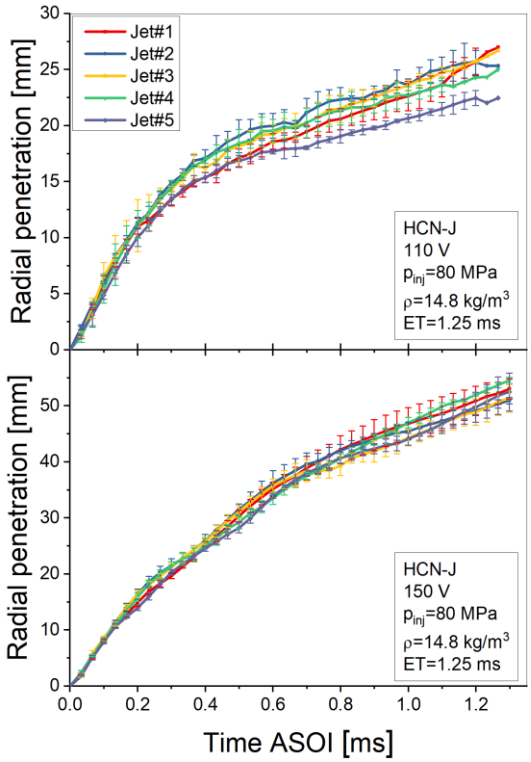

Figure 5.11 - Individual jet penetration profiles comparison at different voltage commands for HCN-J. P_{inj} 80 MPa; ρ 14.8 kg/m^3; T_{amb} 298 K.

Figure 5.11 reports, for the same working conditions, the individual jets penetration profiles identified by 'jet#1' to 'jet#7' curves. The first chart refers to the lowest voltage command (110 V), the second one the highest voltage (150V). It is interesting to note that the anisotropy between the jets is tiny for the 150V condition. Some perceivable variations in the jets' penetration can be found at the lowest voltage command after about 0.4 ms. It demonstrates not optimal repeatability in this operating

condition. The measurements have been carried out on the main injection and the seven sprays and then averaged on five repeated images.

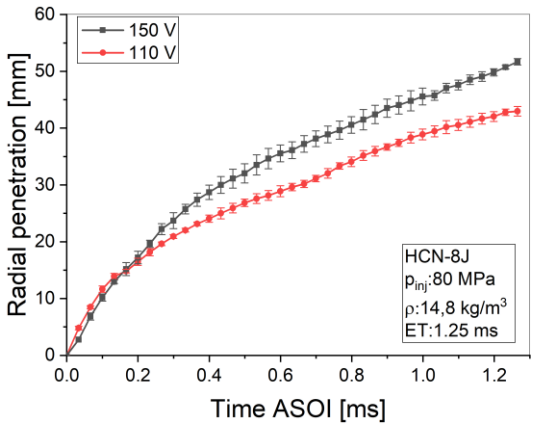

Figure 5.12 – Comparison of spray radial penetration at different voltage commands for HCN-8J. P_{inj} 80 MPa; ρ 14.8 kg/m3; T_{amb} 298 K.

Figure 5.9 illustrates the liquid trends as a function of the voltage command for the HCN-8J injector at ambient temperature (298 K) at an injection pressure of 80 MPa. The same progress is observed until 0.2 ms in terms of spray penetration. As the injection event progresses, a constant gap between the two penetrations at different voltages is highlighted. The jets are evident from the first instant of the injection phase for both voltage command (Figure 5.7c), compared to HCN-J, whose jets not have the typical shape at 110 V (Figure 5.8b).

5.3.2 Nozzle Deterioration Effect

In the following paragraph, the effect of the carbonaceous deposits of the nozzle after the test campaign in the single-cylinder engine was evaluated.

The analysis foresees the spray characterization of the HCN-8J prototype before and after the engine test campaign. This analysis aimed to evaluate both the effect on the spray's shape and the penetration into the combustion vessel.

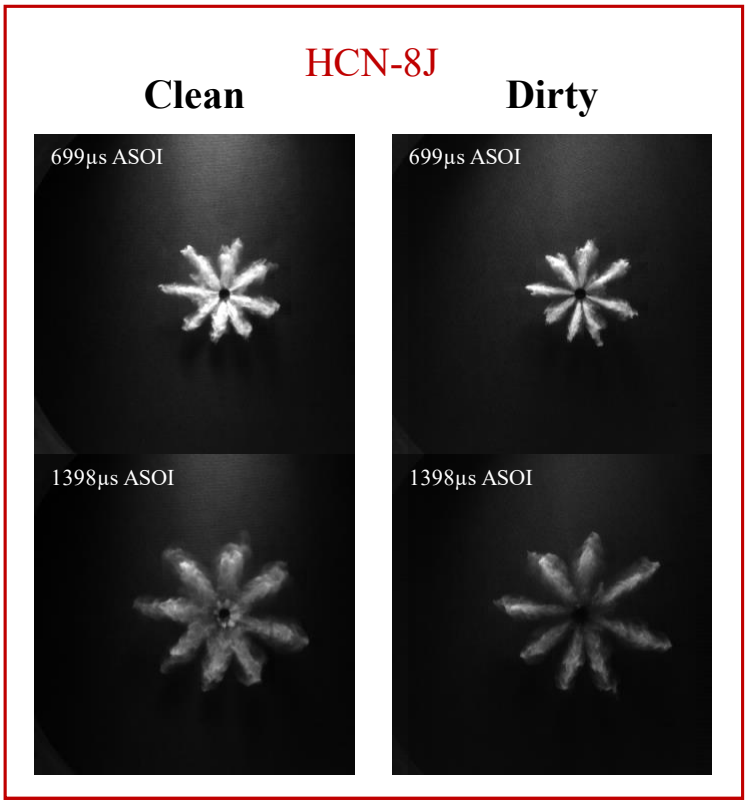

Figure 5.13 - Spray comparison in different operating conditions clean(left) and dirty (right), at p_{inj}: 80 MPa, T_{amb}: 298 K, 150 V for HCN-8J.

Example images obtained from the Mie-scattering tests for a case with an injection pressure of 80 MPa and vessel conditions of 14.55 kg/m^3, 293 K, and 150 V for the different operating conditions are shown in Figure 5.13. Considering the first step (699 µs), it observes a spray more distributed over the entire circumference, especially near the nozzle, as regards the clean nozzle. Instead, the dirty one has more distinguishable and uniform jets between them. A particular aspect to highlight is the rebound of the plate after the end of the injection for a clean nozzle. In fact, in the second illustrated frame (1398 µs), a further injection is observed due to a reopening of the injector, a phenomenon that cannot be seen at the same time for the dirty one. Therefore, the effect of carbon deposits on the nozzle has a positive impact on the injection process since the reopening, in cleaned condition, inevitably causes an increase in polluting emissions, in particular, the soot.

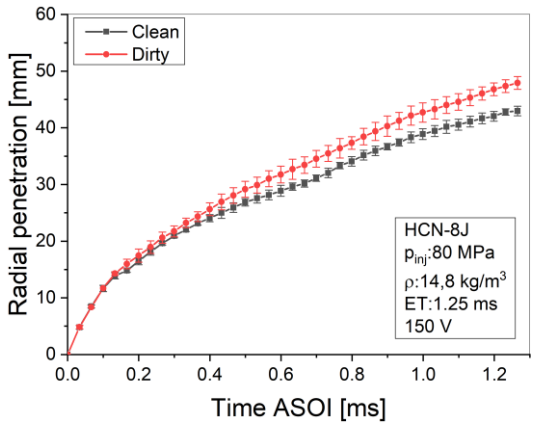

Figure 5.14 - Comparison of spray radial penetration at operating conditions for HCN-8J. P_{inj} 80 MPa; ρ 14.8 kg/m3; T_{amb} 298 K, and 150 V.

Figure 5.14 shows the post-processed values of spray penetration from the same operating condition, as in Figure 5.13. The penetration delta has a significant change of slope at 0.3 ms. It is linked to the carbon deposit due to the combustion previously discussed.

When the injection event advances, it would be expected that nozzle dirty showed the shortest penetration due to its lower area. Nevertheless, the dirty nozzle provides a reduction of dynamic fluid losses, generating drops characterized by a larger diameter, thus ensuring a more significant momentum, such as to justify this gap, approximately equal to 10%.

5.3.3 Injection Parameters Effect

In this section, the injection pressure, energizing duration, and ambient temperature were changed to analyze and compare the specific influence of each actuating variable on the nozzle exit flow. The discussion in this section will only concern the characterization of HCN spray. The main characteristics describing the development of the liquid and vapor phases will be showed for both non-evaporative (T_{amb} 298 K) and evaporative conditions (T_{amb} 560 K) at constant voltage command (150V). Mie scattering and schlieren were employed to measure the spray characteristics. The optical setup was discussed in Chapter 3, and as shown in Figure 5.15.

The images were acquired using a high-speed C-Mos camera (Photron FASTCAM SA4), at a rate of 45,000 frames per second (fps) with an image window of 384x192 pixels. The camera was equipped with a 90 mm objective, f 1:2.8, resulting in the spatial resolution 4.5 pixels/mm.

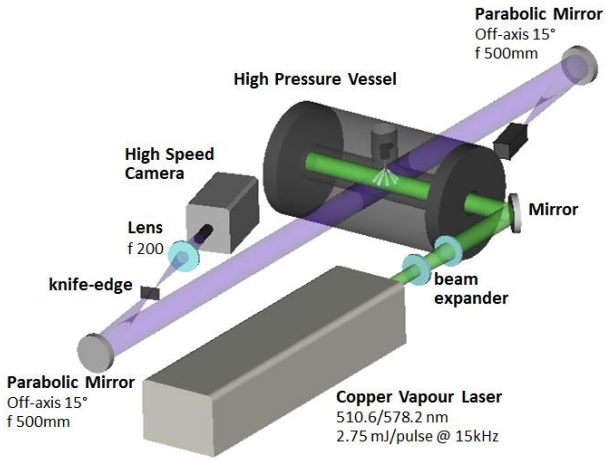

Figure 5.15 - Experimental Setup.

The liquid phase under non-evaporative conditions was analyzed by both schlieren and Mie scattering optical technique. The spray morphology captured by the two techniques appeared very similar; hence, the choice was to report in this paragraph just the analysis by Mie scattering for the liquid phase at non-evaporative temperature. The general spray shape and the evolution of the spray structure are shown in Figure 5.16, where Mie scattering images of the liquid spray are reported at a different time from the start of injection at the injection pressure of 80 MPa under non-evaporative condition.

From the spray images at the transition phase, it is evident that the emerging annular liquid jet is somewhat regular, reaching a quasi-equal penetration in the axial direction at the spray front. Later, a slight non-uniform distribution of the fuel is observed (more penetrating on the left side), probably due to a non-regular lift of the injector plate and resulting in a non-uniform nozzle exit area. Therefore, a higher amount of fuel fluxing was observed on one side at full needle lift. Nevertheless, we referred to the maximum distance in the vertical direction of the spray front from the injector nozzle as the axial penetration. Vice versa, in the radial direction, the spray develops in quasi-symmetrical mode on both sides for the entire injection event starting from the first instants. However, the radial evolution was measured on both sides, and the average value was calculated for the five repetitions at each injection timing.

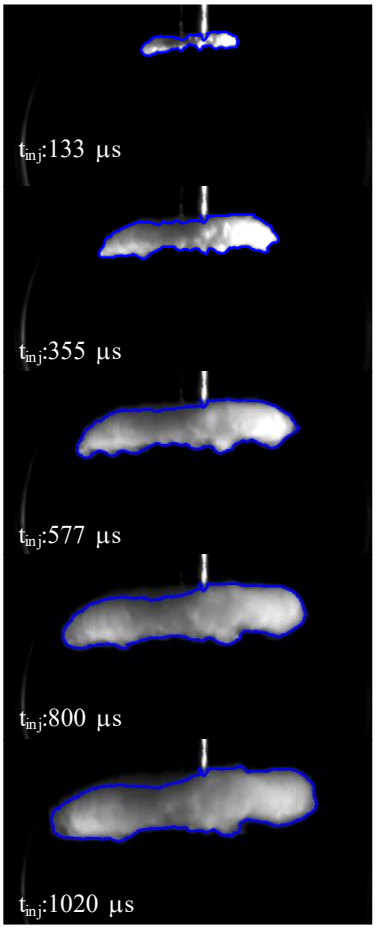

Figure 5.16 - Liquid spray evolution, p_{inj}: 80 MPa, T_{amb}: 298 K, 150 V.

Figure 5.17 shows the effects of the injection duration on both axial (top) and radial (bottom) liquid penetration at 80 MPa of injection pressure. The measurements were collected far beyond the effective injection duration to follow the spray development even after the injector closing. The results were averaged on five consecutive injections to consider the cycle-to-cycle variability with an analysis of the spread. The corresponding error bars are reported per each acquisition time. The first useful measure is relative to the acquired image 22.2 µs after the start of injection (ASOI). Both axial and radial profiles show a quasi-linear growth vs. time for all the investigated durations. Different phases in the spray propagation can be identified: an initial linear propagation with constant velocity during the liquid breakup is followed by a square root shaped deceleration of droplets. The tip penetration trend is mainly a function of the injection pressure, ambient density, and discharge area, while no effects were registered concerning the energizing time. The curves in Figure 5.17 depict a negligible effect of the different injection durations on the spray evolution, being the

profiles overlapping for the common parts. The most prolonged duration of the injections is just an extension of the shortest ones. After the end of injection, the spray slows down the evolution reaching a stable value and a well-scaled behavior regarding the injection duration for both axial and radial development, as shown in the profiles. This aspect is symptomatic of the functional stability of all injection systems.

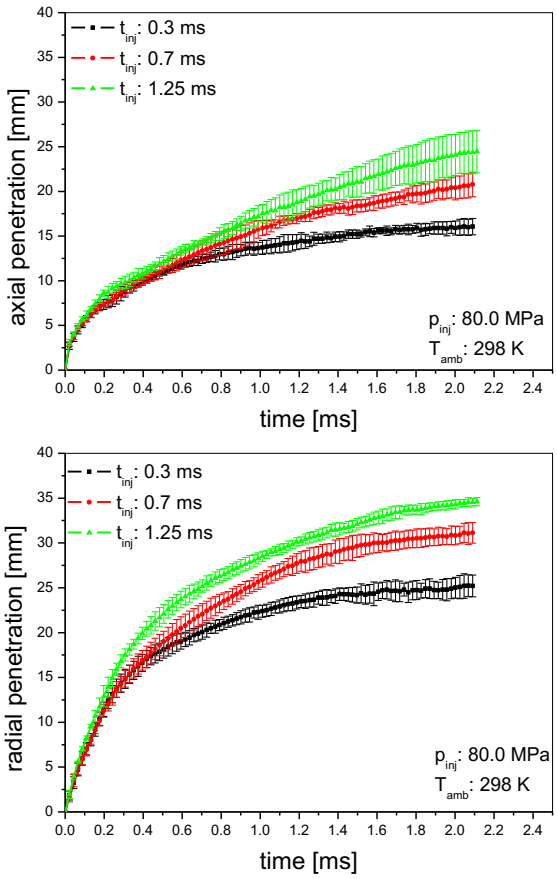

Figure 5.17 - Effect of injection duration on axial (top) and radial (bottom) liquid penetration at an injection pressure of 80 MPa.

The effects of the fuel injection pressure on the hollow cone spray morphology were investigated for the liquid phase under non-evaporative conditions. Figure 5.18 reports two Mie scattering spray sequences at the injection pressures of 80 (left) and 120 MPa (right) at different time ASOI for the energizing time of 0.7 ms. The increase of the injected fuel mass, related to the growth of injection pressure, causes a greater liquid penetration in both horizontal and vertical directions. As a consequence, the spray appears denser and brighter (right side) when increasing the amount of injected fuel. Finally, no significant effects were observed on the global spray morphology when varying the injection pressure. The spray repeatability and stability also observed a p_{inj}

of 120 MPa demonstrates the capability of the HCN injector to generate a high-pressure hollow cone spray.

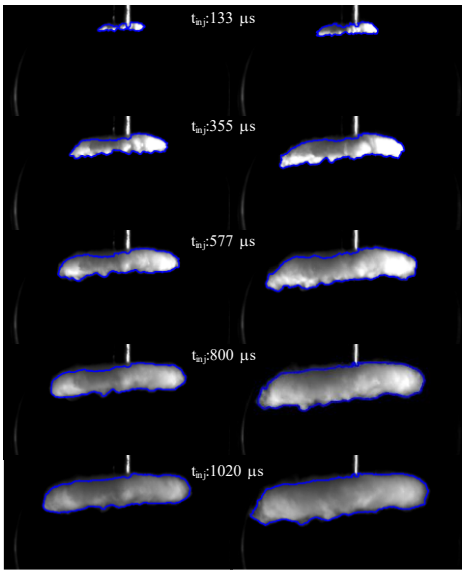

Figure 5.18 - Liquid spray sequences for two injection pressures: 80.0 (left) and 120.0 MPa (right).

Figure 5.19 depicts the liquid axial and radial penetration trends concerning the different injection pressures. The curves confirm the increment of the spray on both directions with increasing of the injection pressure from 80 to 120 MPa. The profiles overlap only at the early stages; later, the most significant fuel momentum generates a healthy growth of the spray evolution on both sides. Even though the geometry of the injector differs completely from classical diesel multi-hole nozzle, the shape of the penetration curves showed that the physical processes seem to be quite similar with the primary and secondary breakup mechanisms that break up the liquid core, exiting in the nozzle, into ligaments, blobs and kid droplets [17]–[19].

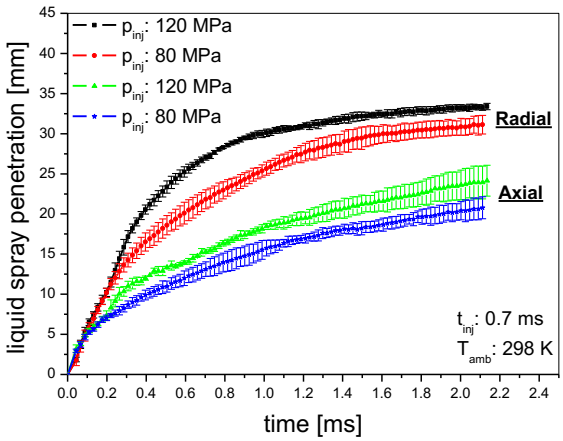

Figure 5.19 - Liquid axial and radial penetration for different injection pressures.

The evaporative conditions were studied by increasing the ambient temperature up to 560 K, far beyond the n-heptane boiling point (371.4 K) [20]. A J-type thermocouple located inside the pressurized vessel allowed a precise measure of the ambient temperature with deviation respect to the set value within the range of ± 5 K.

Figure 5.20 reports an evaporative spray sequence at different time ASOI, derived from Mie scattering (left) and schlieren (right) optical technique. The imagines refer to the injection pressure of 80 MPa and an injection duration of 1.25 ms. For each column, the effects of the ambient temperature can be evaluated on the liquid phase from the Mie scattering images and, on both liquid and vapor from the schlieren ones.

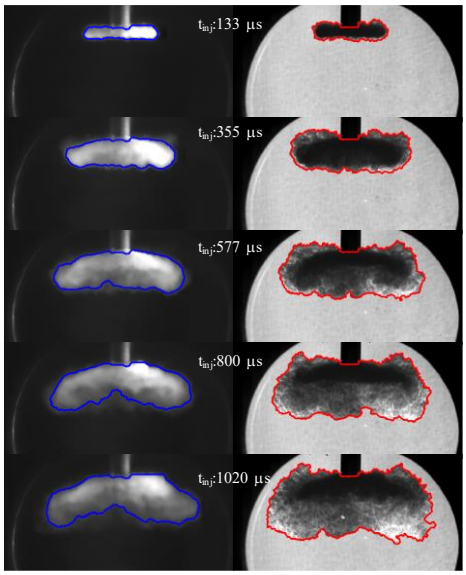

Figure 5.20 - Spray sequence under evaporative conditions, liquid, and vapor detection.

The increment of the ambient temperature affects both the liquid, with much-dispersed droplets and the vapor phases. The schlieren spray images in Figure 5.20 displays a liquid dense core (dark part immediately close to the nozzle) and surrounding the liquid portion; a mixed area includes ligaments, droplets more or less finely atomized and vapor phase. The vapor phase begins to develop at the outer spray edge, because of a stronger droplets' atomization and then grows more and the time. The spatial and temporal spray evolution shows the capability of this nozzle configuration of generating a finely atomized spray homogeneously and circumferentially distributed and this aspect could be contributing to a better fuel-air mixing level.

As concern the liquid phase, the evaporation rate can be estimated in the liquid spray penetration plot of Figure 5.21 for both axial (top) and radial (bottom) direction. Figure 5.21 depicts the liquid trends as a function of the ambient temperature from the room (blue curves) to 560 K (red curves) at an injection pressure of 80 MPa. As regards the axial propagation (on the top), the profiles overlap up to around 0.2 ms, indicating a negligible effect of the vaporization process at the early stages. Later, at the highest temperature, the liquid penetration is longer than that corresponding to the room one. The reason for this unexpected behavior could be explained by looking at Figure 5.22, where the comparison between liquid spray under evaporative condition (on the left) and non-evaporative one (on the right) are reported. As previously discussed, at room temperature, the liquid spray front develops over time in a quasi-uniform way (right side in Figure 5.22). Vice versa, the effects of the vaporization process promote a liquid spray collapse towards the middle, where the fuel concentration is less dense than in the periphery, with a consequent contraction of the spray cone angle. Consequently, on both sides of the spray, two lobes more penetrating form. The penetration on the sides increases more and more concerning the central part up to the end of the injection event. This maximum value was considered as axial penetration, and it justifies a more extended liquid spray propagation in the vertical direction when evaporative conditions occur than room temperature ones.

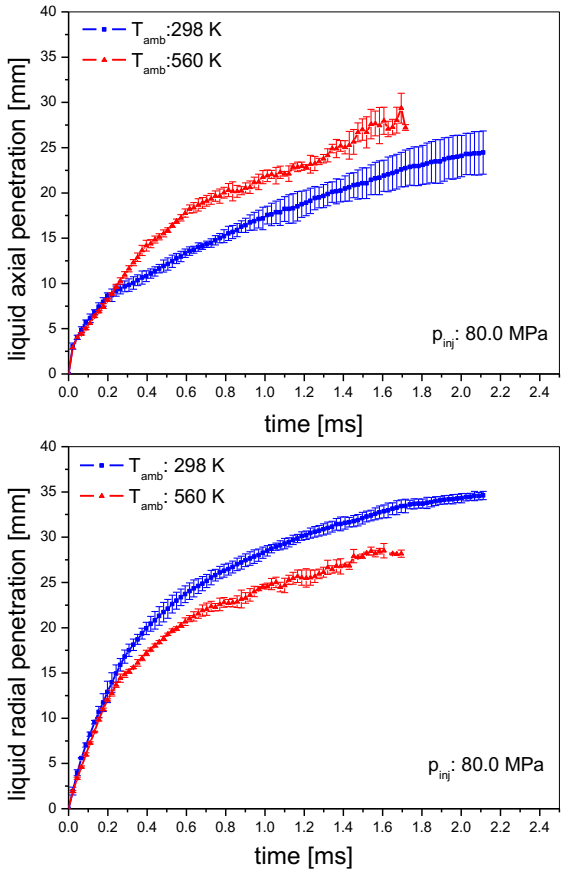

Figure 5.21 - Effect of ambient temperature on liquid axial (top) and radial (bottom) penetration at an injection pressure of 80.0 MPa.

The inverse trend was carried out from the liquid radial evolution (bottom part Figure 5.21). The contraction of the liquid hollow cone spray generates a strong reduction of the liquid phase in radial direction because of the vaporization process. The divergent trend between the liquid profiles under evaporative condition (red curve) and non-evaporative (blue curve) is the consequence of the vaporization of the liquid fuel in the horizontal direction that grows more and the time.

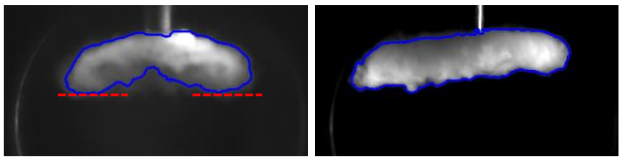

Figure 5.22 - Evaporative (left) and non-evaporative (right) liquid spray morphology.

Figure 5.23 reports the liquid and vapor penetration profiles against the time at the ambient density of 14.8 kg/m^3 and an injection pressure of 80 MPa for both axial (on the top) and radial direction (on the bottom). The blue lines were derived from the Mie

scattering acquisitions and related to the liquid evolution. The red ones resulting from the schlieren images and represent liquid and vapor, at the conditions where both phases coexist, and just the vapor upon complete fuel vaporization. At early time, the schlieren penetration curves match up with the Mie scattering ones indicating that no vapor is detected surrounding the liquid. Later, the penetration curves begin to differ from each other. This deviation indicates the existence of the vapor phase in addition to liquid one in both directions. It is worthwhile to realize that, without the corresponding Mie scattering images, this could not be derived alone from the schlieren being the last inclusive of both the liquid and the vapor phases in undifferentiated mode. At the later time from the start of the injection, the vapor profiles move forward faster than liquid ones with a slight tendency for both liquid and vapor radial curves to saturate at long times.

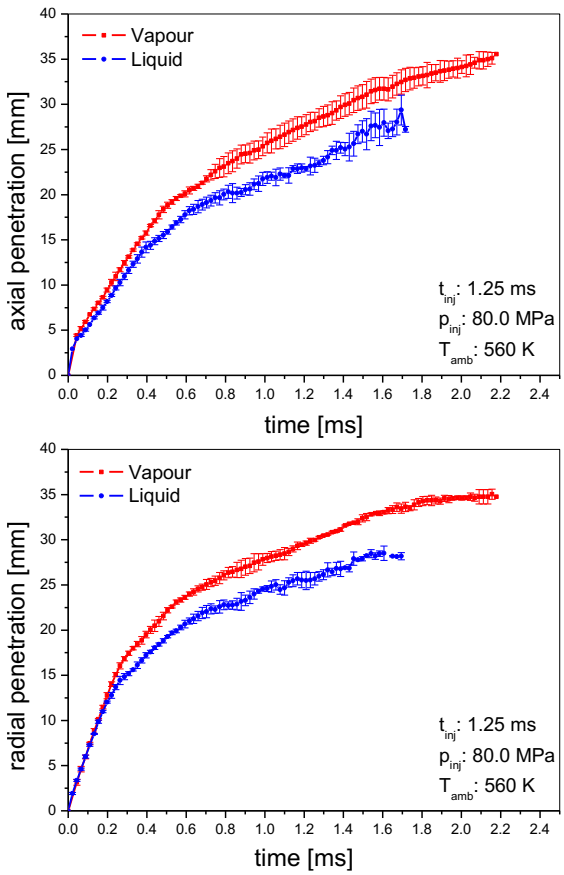

Figure 5.23 - Axial (top) and radial (bottom) penetration profiles under evaporative conditions; liquid (blue curves) and vapor (red curves).

5.4 Experimental and Numerical Comparison

5.4.1 The code

The simulation of diesel spray experiments in the constant volume vessel was performed for the test conditions of Table 5.4 in non-evaporating and evaporating conditions. The numerical characterization of the spray pattern was performed with the OpenFOAM® CFD methodology [21], adopting the Lib-ICE set of libraries well developed for internal combustion engine applications [22, 23].

Table 5.4 – Experimental condition.

p_{inj} [MPa]	80
ET [ms]	1.25
T_{amb} [K]	298 - 560
ρ_{gas} (SF_6) [kg/m^3]	14.8
p (SF_6) [MPa]	0.25@298K and 0.47@560K
Fuel	n-heptane

The injection rate from AVL [14] was assumed as input data for the test conditions of Table 5.4 under both evaporative and non-evaporative conditions. The mass flow rate profile was corrected with a discharge coefficient (Cd) that takes into account only the variation of the geometrical discharge area due to the needle lift during the injection event. In the present simulation, the contemporary effects on the active fuel discharge area at the nozzle exit caused by cavitation pockets and/or air bubbles produced by the air entrainment (from the outside regions into the nozzle) are neglected because information on the flow inside the nozzle was not yet available. The evolution of the spray was simulated through the classical models for high-pressure spray simulation. The Discrete Droplet Model (DDM), based on a Lagrangian approach, is used to describe the liquid phase while a Eulerian description is employed for the gas phase [24]. The spray droplets are described by stochastic particles, which are usually referred to as parcels [25].

The setup of spray sub-models is reported in Table 5.5. Some literature information were found about physical mechanisms involved in the breakup process for an outwardly HCN injector operating at low p_{inj} typical of GDI applications [17, 26, 27], while few studies are relative to higher p_{inj} typical of diesel fuel (like CR FIS) [28]. As verified in a previous paper [29], the physical breakup mechanisms appear well similar

to those typical of MHN, therefore, in this first numerical approach, the Kelvin-Helmholtz (KH) and Rayleigh-Taylor (RT) mechanisms by Reitz [30] were employed, with the main constant values of B_0 and B_1 equal to 0.61 and 15 respectively. In the following simulations, the standard drag model and a so-called 'random walk procedure' for turbulent dispersion were adopted [31].

Table 5.5 - Setup of spray sub-models for spray simulation.

Models	Setup
Injector	Hollow Cone
Atomization	off
Breakup	KHRT
Evaporation	Frossling
Heat Transfer	Ranz-Marshall

All simulations were performed adopting the standard k-ε model for turbulence description [21]. Drop to drop collisions, generally neglected due to their high dependency from the quality of the mesh, were here considered, thanks to the adoption of the Adaptive Local Mesh Refinement (ALMR) technique [32]. Starting from an initial mesh quite coarse, the ALMR was employed for a correct prediction of the spray behavior, keeping an acceptable computational time. The mesh refinement is performed only in the cells where the total fuel mass fraction is within a specific range. In this way, the simulation started with a cell size of 2.2 mm and 19683 cells, which was progressively refined during simulation up to a cell size of 0.25 mm in the spray region and about 252000 cells. The predictive capabilities of the code, when the ALMR technique is used, were assessed in previous work [32].

No experiments were available for HCN nozzle forming a dense array of distinct streaks of fuel systematically ordered around the circumference of the cone when injection pressure is higher than 30 MPa. This means that no information is available about the shape and morphology of fuel structures at the nozzle exit [33] from HCN spray, neither about the droplet diameter size at injection nor during the breakup process. Therefore, the choice of the initial condition of SMD for HCN spray simulation is critical, and SMD represents the most uncertain parameter. The followed approach is based on the hypothesis of assuming the mean initial drop size diameter directly related to the outward needle lift. Different tests were performed for sensitivity analysis concerning the value of initial drop diameter and are reported in Figure 5.24 varying the initial value from 20 to 40 μm around the highest value of needle lift in the

operating conditions equivalent to 24 µm. The choice of initial drop diameter seems to have a very slight effect on liquid tip penetration (as 99% of liquid mass penetration) due to the minimal initial diameter values [33]. This analysis shows that once injected, the mechanism of primary atomization, secondary breakup, and droplet collisions is very fast, and after only 200 µs, the diameter is reduced up to about 8 µm for all initial diameter sizes. In the considered conditions, the predictive capabilities of the code in capturing spray characteristics for HCN injector were evaluated in the next paragraph comparing numerical results with experimental ones.

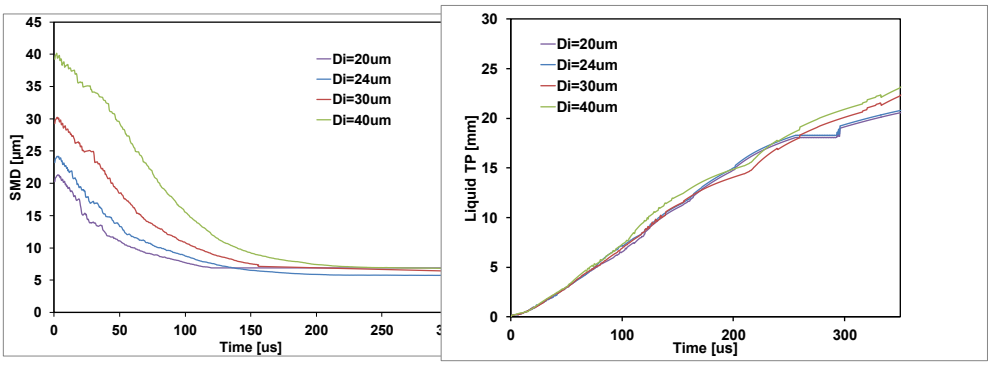

Figure 5.24 - Sensitivity analysis of the effect of initial drop diameter on drop diameter reduction and liquid TP.

5.4.2 Numerical Results

In Figure 5.25, the schlieren images of the spray were compared with numerical images for the injection conditions of Table 5.4 under non-evaporative conditions. The spray evolution is analyzed from 110 up to 1000 µs after the start of injection. Figure 5.25 shows the comparison of frontal images evidencing a quite good agreement in terms of spray shape and spray diffusion during the injection event.

The comparison between experimental and computed results in terms of liquid TP is reported in Figure 5.26. Numerical images were processed through the same customized procedure developed in MATLAB applied on experimental images for radial and axial TP calculation, as described in the previous paragraph. This procedure was also employed because, in these numerical tests, the hollow cone injector model does not take into account the exact radius of the needle seat diameter. Considering the measured error bars, the axial liquid TP is quite accurately predicted from the code, and the calculated evolution reproduces quite well the experiments during the whole injection event. Up to 500 µs, the agreement between calculated and measured radial liquid TP is also excellent, while after 500 µs, its value is overpredicted. At the end of the injection event, the overestimation reaches about 25%: the increasing discrepancy

in terms of radial TP can probably be ascribed to model inaccuracies in the prediction of the recirculation motion at the jet periphery, as better clarified looking at the following Figure.

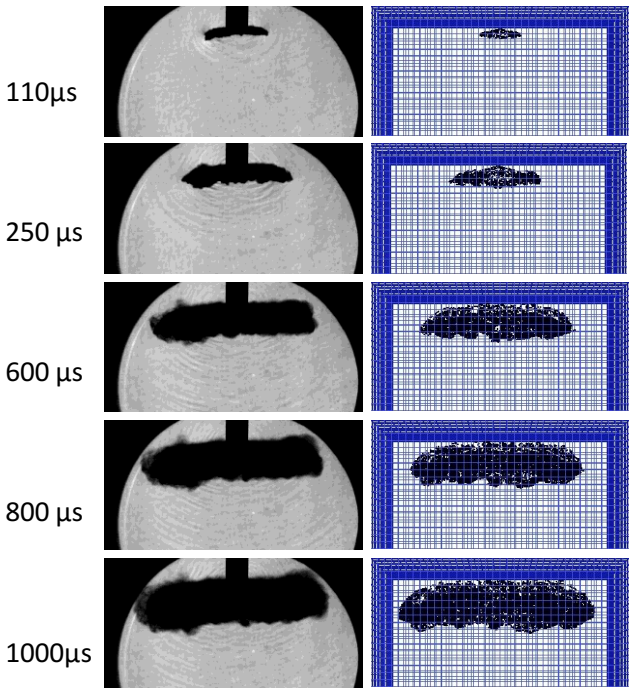

Figure 5.25 - Frontal spray evolution acquired with schlieren images (left) compared with numerical spray images (right) under non-evaporative conditions.

Figure 5.27 shows, in fact, the evolution of the droplet velocity distributions during the injection event. In these computed spray images, vectors are colored according to the injection velocity. As reported in a previous paper [29], measured images show a particular effect of the cloud of the spray propagation not only in the forward direction but also backward to the rear wall of the constant volume vessel. This recirculation zone, typical of HCN sprays [34], is scarcely captured by the computations, as visible in Figure 9: despite toroidal vortices at the edges of the conical spray are detectable, the amount of predicted recirculation is likely to be lower than the actual one. As a result, foreseen radial TP turns out to be overestimated, as previously discussed.

Different contemporary effects could be considered responsible for this fuel backflow. Firstly, the intense airflow from the outside region enters into the conical spray [34], then the hydraulic dynamic behavior of the needle lift itself forms air bubbles and cavitation pockets in the gap between the pintle and the seat [35], or a continuous vapor film around the circumferential needle sealing area [17, 26, 27].

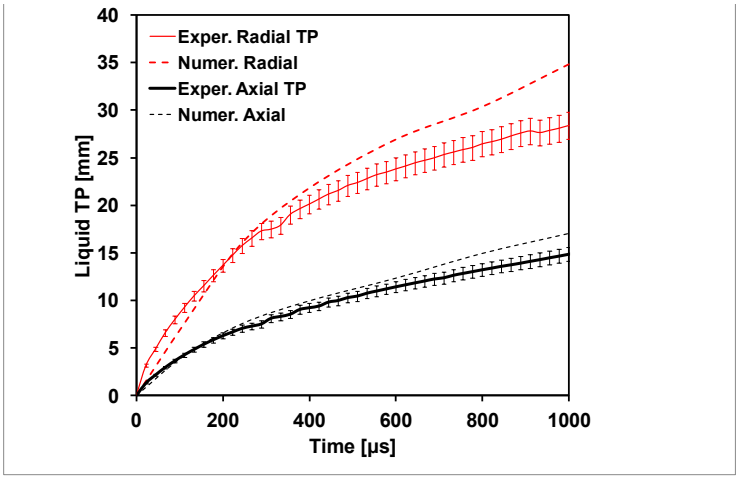

Figure 5.26 - Comparison between experimental and numerical liquid TP for both the axial and radial components under non-evaporative conditions.

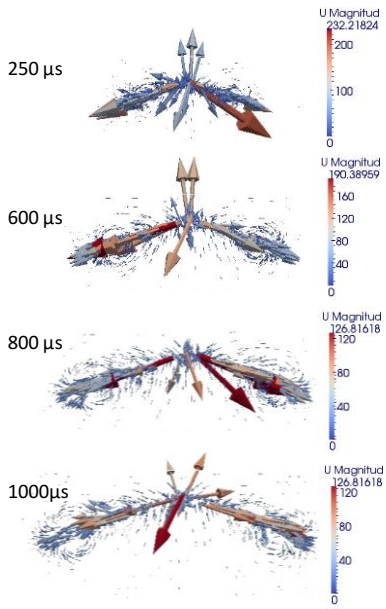

Figure 5.27 - Evolution of air and droplets velocity distribution in a symmetry plane under non-evaporative conditions.

Figure 5.28 shows the comparison under evaporative conditions between experimental Mie scattering images and calculations in terms of liquid fuel mass fraction distribution in the constant volume vessel.

The comparison between experimental and numerical images always must take into account differences because, in the simulation, the injector model does not consider the exact radius of the needle seat diameter. Based on these considerations, the evolution of the calculated liquid mass fraction reproduces quite well the measured

liquid tip penetration in the radial direction, as already demonstrated in Figure 5.29, considering the radial component.

On the contrary, the axial penetration of the liquid mass fraction seems to be underestimated by simulations, as also reported in Figure 5.29. This effect could always be ascribed to the lack of the code insufficiently describing the recirculation zone at the jet periphery that is more and more evident under evaporative conditions at higher ambient temperature and pressure conditions. As verified under non-evaporative conditions, the amount of the predicted recirculation is likely to be lower than the measured one. Therefore, the bending of the spray, evidenced by the experiments in Figure 5.25, is not adequately predicted from the code after 200 µs. As a consequence, although the radial liquid TP seems better predicted to the ambient temperature and pressure conditions (see Figure 5.25 and Figure 5.26), the axial liquid TP calculated is significantly underestimated to the measured values, as displayed in Figure 5.28 and Figure 5.29.

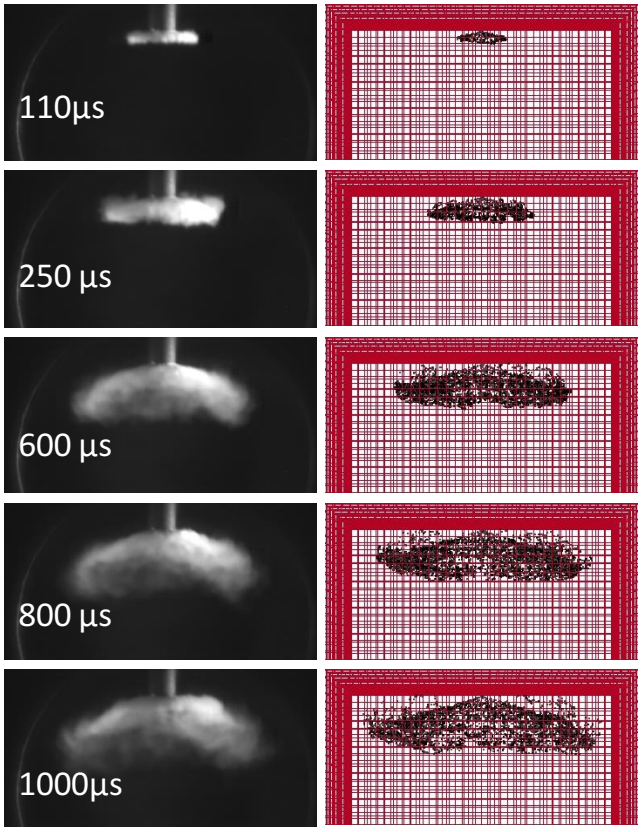

Figure 5.28 - Frontal liquid mass fraction evolution acquired with Mie images (left) compared with numerical spray images (right) under evaporative conditions.

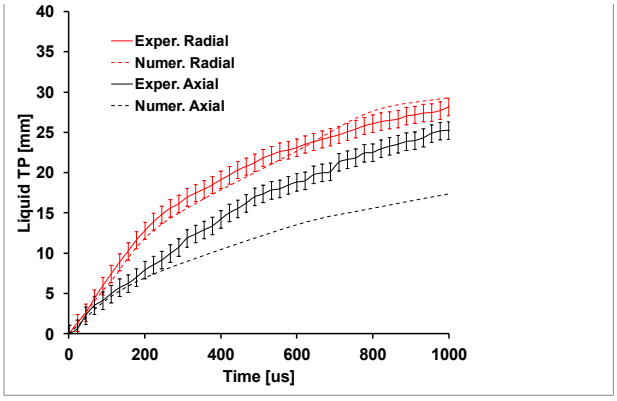

Figure 5.29 - Comparison between experimental and numerical liquid TP for both the axial and radial components under evaporative conditions.

Figure 5.30 shows the evolutions of fuel vapor mass distribution measured from the schlieren technique and calculated from the code. The comparison in terms of vapor diffusion and penetration shows that the radial vapor penetration seems quite acceptable, while the predicted vapor axial penetration is underestimated. These results reported in Figure 5.31 in terms of vapor tip penetration curves are coupled with the underestimation of the liquid mass fraction penetration, as explained before.

As evidenced in Figure 5.30, the smallest drop diameter sizes of HCN nozzle produce very fast evaporation at the early stages of the injection process, with the vapor homogeneously distributed along the circumference and located in an annulus very near to the nozzle. The well-developed cloud of vapor during the injection event exhibited by the HCN prototype injector allows a right fuel-air mixing level.

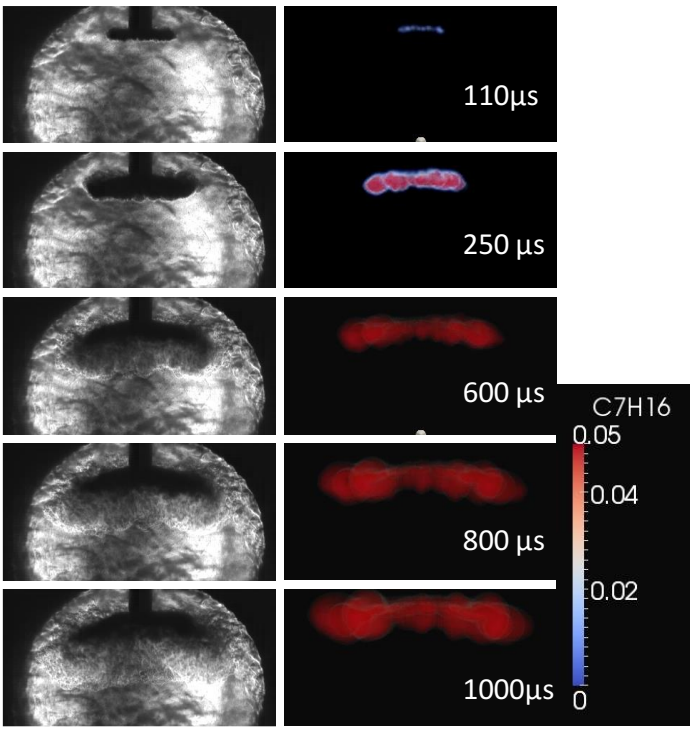

Figure 5.30 - Frontal vapor mass fraction evolution acquired with schlieren images (left) compared with numerical spray images (right) under evaporative conditions.

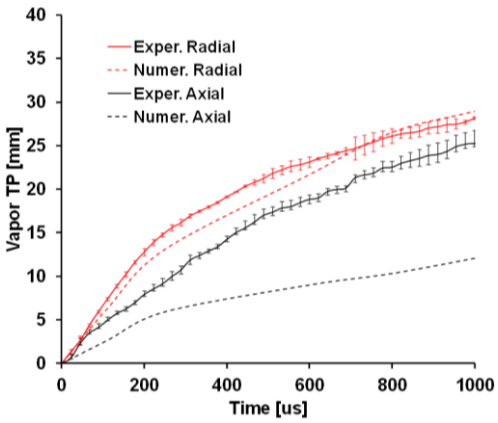

Figure 5.31 - Comparison between experimental and numerical vapor TP for both the axial and radial components under evaporative conditions.

5.5 HCN vs. MHN

To understand the response of the considered HCN injector in terms of the evaporative rate, a comparison with the classical MHN was made at the same injection conditions. The reference MHN was characterized with 7 holes, and a diameter of 141 µm [29]. Figure 5.32 shows the evaporation rate from both injectors, calculated as a

fraction between the vapor mass fraction and the residual liquid mass fraction. The HCN injector evidences a higher vapor production to the classical MHN injector in the first 500 μs after the start of injection. This trend is limited after this time due to the lower penetration and to the lower air entrainment exhibited by the HCN to the MHN [29]. As reported in [29], HCN spray atomization and penetration are sensitive to the injection control parameters (in particular to the injection pressure level, and the HV-stationary level of the voltage command at the actuator). Therefore, graduating injection control parameters, it could be possible to appropriately control spray penetration and atomization levels in a dedicated engine combustion chamber, and as a consequence, to exploit the potentiality of an initial high evaporation rate presented by the HCN injector.

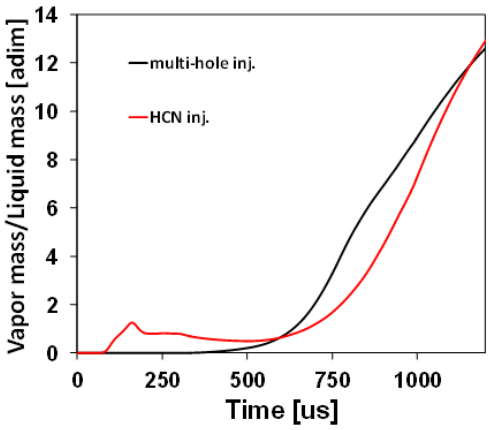

Figure 5.32 - Computed vapor mass fraction relative to residual liquid mass fraction for the HCN and MHN during the injection event.

In Figure 5.33, a comparison of the jet penetration profiles for the different injectors versus time from the start of injection is reported.

The injectors considered can be divided according to the cone angle of the spray, which significantly influences the radial penetration values. The HCN and HCN-J have a greater angle than the other two (145° vs. 100°). In fact, in Figure 5.33, the main difference is due to this aspect, especially in the stationary phase.

Neglecting the HCN (old version), for now, then considering the other prototypes and comparing them with the classic MHN, a higher penetration than the latter is observed, in the transitional phase, up to about 0.4 ms. As the injection event progresses, the penetrations of the prototypes with a higher cone angle, are almost similar to MHN.

Concerning the HCN-8J, there is a detachment from the prototypes just described with an almost parabolic trend, of about 20% compared to the reference injector.

The HCN (old version) turns out to be a version before these injectors just described, whose cone angle is tiny, typical of a GDI injector, which does not guarantee adequate radial penetration for a compression ignition combustion. Admittedly, it will have an axial penetration, which has not been reported in the text, that it will undoubtedly be higher than the cases illustrated and cause a more significant impact on the combustion chamber with a consequent increase in emissions. This aspect will be better described in the following chapter.

In conclusion, the prototype injectors, except the HCN (old version), generate a spray in line with the traditional MHN, except for having more excellent atomization and distribution of the fuel.

Differences in the shapes seem not to produce effects on the spray penetration for this operating condition, concerning the HCN and HCN-J, meaning the negligible role played by the nozzle. Considering the different mixing air-fuel in evaporating condition and the response between the different electric command, the spray shape could have a fundamental role, an aspect that will be evaluated in the following chapter.

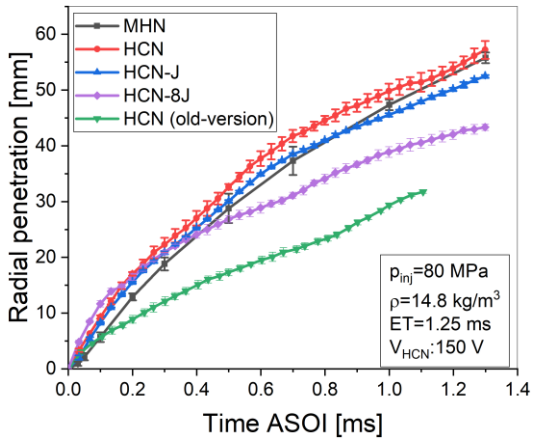

Figure 5.33 – Comparison of the radial tip between prototypes and MHN.

REFERENCES

[1] B. Mahr, 'Future and potential of diesel injection systems', in Thermo-and Fluid Dynamic Processes in Diesel Engines 2, Springer, 2004, pp. 3–17.

[2] F. Brusiani, G. M. Bianchi, S. Falfari, A. Onorati, T. Lucchini, and R. Di Gioia, 'Influence of cylindrical, k, and ks diesel nozzle shape on the injector internal flow field and on the emerging spray characteristics', SAE Technical Paper, 2014.

[3] B. Argueyrolles et al., 'Influence of injector nozzle design and cavitation on coking phenomenon', SAE Technical Paper, 2007.

[4] D. Ueda, H. Tanada, A. Utsunomiya, J. Kawamura, and J. Weber, '4th Generation Diesel Piezo Injector (Realizing Enhanced High Response Injector)', SAE Technical Paper, 2016.

[5] X. Leng, Y. Jin, Z. He, W. Long, and K. Nishida, 'Numerical study of the internal flow and initial mixing of diesel injector nozzles with V-type intersecting holes', Fuel, vol. 197, pp. 31–41, 2017.

[6] Z. Han, S. E. Parrish, P. V. Farrell, and R. D. Reitz, 'Modeling atomization processes of pressure-swirl hollow-cone fuel sprays', Atomization and sprays, vol. 7, no. 6, 1997.

[7] P. Senecal, D. P. Schmidt, I. Nouar, C. J. Rutland, R. D. Reitz, and M. Corradini, 'Modeling high-speed viscous liquid sheet atomization', International Journal of Multiphase Flow, vol. 25, no. 6–7, pp. 1073–1097, 1999.

[8] A. B. Dempsey, S. J. Curran, and R. M. Wagner, 'A perspective on the range of gasoline compression ignition combustion strategies for high engine efficiency and low NOx and soot emissions: Effects of in-cylinder fuel stratification', International Journal of Engine Research, vol. 17, no. 8, pp. 897–917, 2016.

[9] M. Sellnau, M. Foster, K. Hoyer, W. Moore, J. Sinnamon, and H. Husted, 'Development of a gasoline direct injection compression ignition (GDCI) engine', SAE International Journal of Engines, vol. 7, no. 2, pp. 835–851, 2014.

[10] S. Ciatti and S. N. Subramanian, 'An experimental investigation of low-octane gasoline in diesel engines', Journal of engineering for gas turbines and power, vol. 133, no. 9, p. 092802, 2011.

[11] M. Oki, S. Matsumoto, Y. Toyoshima, K. Ishisaka, and N. Tsuzuki, '180MPa piezo common rail system', SAE Technical paper, 2006.

[12] J. Smith, G. Szekely Jr, A. Solomon, and S. Parrish, 'A comparison of spray-guided stratified-charge combustion performance with outwardly-opening piezo and multi-hole solenoid injectors', SAE International Journal of Engines, vol. 4, no. 1, pp. 1481–1497, 2011.

[13] J. Sim, J. Badra, A. E. Elwardani, and H. G. Im, 'Spray modeling for outwardly-opening hollow-cone injector', 2016.

[14] W. Bosch, 'The fuel rate indicator: a new measuring instrument for display of the characteristics of individual injection', SAE Technical Paper, 1966.

[15] I. Wallace, 'Injection rate gauge: pass off information and user instructions', Fuel & Engine Management Systems, Graz-December, 2002.

[16] R. Payri, F. Salvador, J. Gimeno, and G. Bracho, 'A new methodology for correcting the signal cumulative phenomenon on injection rate measurements', Experimental techniques, vol. 32, no. 1, pp. 46–49, 2008.

[17] A. M. Schmid, 'Experimental characterization of the two phase flow of a modern, piezo activated hollow cone injector', PhD Thesis, ETH Zurich, 2012.

[18] G. Faeth, L.-P. Hsiang, and P.-K. Wu, 'Structure and breakup properties of sprays', International Journal of Multiphase Flow, vol. 21, pp. 99–127, 1995.

[19] M. Pilch and C. Erdman, 'Use of breakup time data and velocity history data to predict the maximum size of stable fragments for acceleration-induced breakup of a liquid drop', International journal of multiphase flow, vol. 13, no. 6, pp. 741–757, 1987.

[20] W. M. Haynes, CRC handbook of chemistry and physics. CRC press, 2014.

[21] 'OpenFOAM® web site, "The Open-source CFD toolbox". http://www.openfoam.org. OpenCFD Limited 2007.'

[22] T. Lucchini, G. D'Errico, D. Ettorre, and G. Ferrari, 'Numerical investigation of non-reacting and reacting diesel sprays in constant-volume vessels', SAE International Journal of Fuels and Lubricants, vol. 2, no. 1, pp. 966–975, 2009.

[23] T. Lucchini et al., 'Full-cycle CFD modeling of air/fuel mixing process in an optically accessible GDI engine', SAE International Journal of Engines, vol. 6, no. 3, pp. 1610–1625, 2013.

[24] J. K. Dukowicz, 'A particle-fluid numerical model for liquid sprays', Journal of computational Physics, vol. 35, no. 2, pp. 229–253, 1980.

[25] F. Bracco, 'Modeling of engine sprays', SAE Technical Paper, 1985.

[26] J. Nouri, M. Hamid, Y. Yan, and C. Arcoumanis, 'Spray characterization of a piezo pintle-type injector for gasoline direct injection engines', in Journal of Physics: Conference Series, 2007, vol. 85, p. 012037.

[27] Q. Dong, T. Ishima, H. Kawashima, and W. Long, 'A study on the spray characteristics of a piezo pintle-type injector for DI gasoline engines', Journal of Mechanical Science and Technology, vol. 27, no. 7, pp. 1981–1993, 2013.

[28] T. Obokata, W.-Q. Long, and T. Ishima, 'PDA and LDA measurements of large angle hollow cone spray proposed for hot-premixed combustion type diesel engine', SAE transactions, pp. 1071–1084, 1996.

[29] M. Migliaccio, A. Montanaro, C. Beatrice, P. Napolitano, L. Allocca, and V. Fraioli, 'Experimental and numerical analysis of a high-pressure outwardly opening hollow cone spray injector for automotive engines', Fuel, vol. 196, pp. 508–519, 2017.

[30] R. REITZ and others, 'Modeling atomization processes in high-pressure vaporizing sprays', Atomisation and Spray Technology, vol. 3, no. 4, pp. 309–337, 1987.

[31] P. J. O'Rourke, 'Statistical properties and numerical implementation of a model for droplet dispersion in a turbulent gas', Journal of Computational Physics, vol. 83, no. 2, pp. 345–360, 1989.

[32] M. Migliaccio, D. Ettorre, A. Aprovitola, and S. Alfuso, 'Effects of Turbulence Modulation Addition in OpenFOAM® Toolkit on High Pressure Fuel Sprays', SAE Technical Paper, 2011.

[33] J. Sim, J. Badra, A. E. Elwardani, and H. G. Im, 'Spray modeling for outwardly-opening hollow-cone injector', 2016.

[34] S. Das and P. G. VanBrocklin, 'Effect of design and operating parameters on the spray characteristics of an outward opening injector', in Proceedings of the 13th International Multidimensional Engine Modeling User's Group Meeting, Detroit, MI, 2003, pp. 1–6.

[35] M. Jia, M. Xie, H. Liu, W.-H. Lam, and T. Wang, 'Numerical simulation of cavitation in the conical-spray nozzle for diesel premixed charge compression ignition engines', Fuel, vol. 90, no. 8, pp. 2652–2661, 2011.

CHAPTER 6 ENGINE RESULTS

In this chapter, the experimental engine results performed with the different prototypes illustrated in chapter 3 are presented. As a reminder, the main aim of the project, on which the thesis work is based, is the development of an innovative injector nozzle concept design suitable for diesel combustion application; therefore, the results obtained by using the first prototype built is also illustrated and compared to the conventional MHN. The critical issues and motivations that led to the development of new pintle geometries are illustrated. Then, the subsequently developed injectors, the HCN-J, and the HCN-8J results are illustrated. A more comprehensive test campaign was conducted on the HCN-J.

6.1 The first prototype "HCN"

In this paragraph, the results reported in work"[1]" are considered as a reference. The combustion performances comparing the HCN and MHN are reported.

The tests have been performed at an engine speed of 1500 rpm, and two loads conditions of 3.3 and 4.2 bar of indicated mean effective pressure (IMEP) by employing a practical engine parameter calibration. Indeed, the tests have been performed employing a Eu5 engine parameter calibration in terms of injection strategy, boost pressure, swirl, NOx level (controlled by EGR), etc., derived from the real four-cylinder engine.

Considering that the needle lift control is realized through the charging voltage, firstly, the HCN and MHN injectors are compared employing the HCN charging voltage of the manufacturer (122V) in order to reproduce the same fuel flow rate at constant injection timing.

Figure 6.1 shows the in-cylinder pressure, injection profile, HR, and HRR trends for both injectors, the MHN and HCN, and for the operating conditions 1500x4.2. The start of injection (SOI) for the HCN injector is set to get the same combustion center (MBF50%) of the MHN injector. The selected MBF50% value is considered to be the best compromise in terms of emission-efficiencies trade-off, and it derives from the

Eu5 engine calibration employing the MHN, more detail will be shown in the following paragraph.

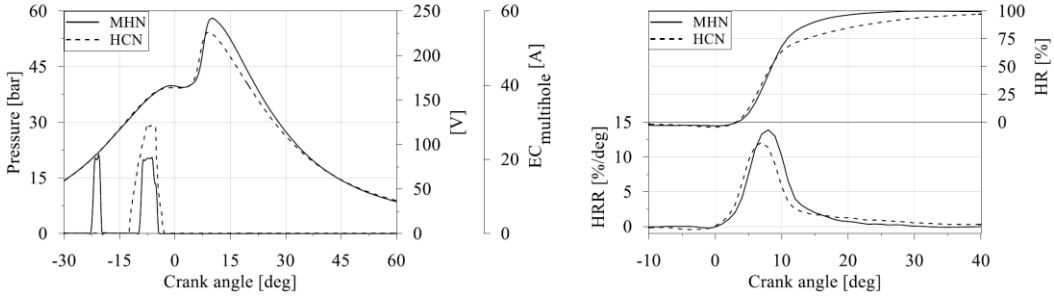

Figure 6.1 - Comparison of In-cylinder pressure and injection energizing pattern (left), Heat Release, and Heat Release Rate (right) at 1500 rpm at 4.2 bar of IMEP and HV 122V, for both injectors [1].

As already pointed out, the engine was operated with a single injection strategy when employing the HCN injector (see Figure 6.1). Notwithstanding the single injection strategy, the HCN combustion shows comparable Heat Release (HR), during the premixed combustion phase, but significantly lower values during the diffusion and late combustion phases. For the HCN injector, the HR decline around 70%. The combustion shifts towards the late combustion phase (Figure 5), increasing the MBF50-90% significantly (Figure 6.2b). However, looking at the HCN results, they are globally worse compared to the MHN injector [1].

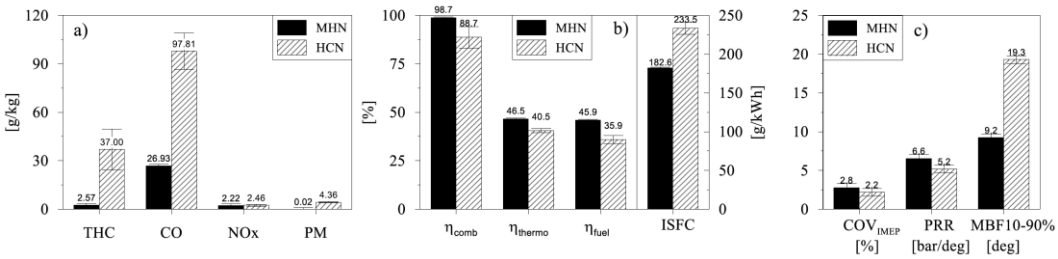

Figure 6.2 - Specific emissions, COV, PRR, and MBF10-90% at 1500 rpm and 4.2 bar of IMEP for MHN and HCN (old version) [1].

The longer combustion duration (calculated as MBF10-90%), in particular, the diffusive-late combustion phase (MBF50-90%), is attributed to the lower spray penetration and kinetic energy compared to the MHN. This aspect was already discussed in Paragraph 5.5, where the HCN (old version) has a lower radial penetration than MHN, due to the lower spray cone angle (148° vs. 100°). Then, the reduced air-fuel spray interaction impacts negatively on the mixing-controlled combustion phase. All these results are also supported by the optical measurements reported in Figure 6.3.

The constant NOx (Figure 6.2a), equal to the Eu5 level, is achieved varying the EGR from 45% to 35% passing from MHN to the HCN. This is related to the general more diffusive combustion of HCN combustion.

When using the HCN injector, the global indicated efficiency (η_{fuel}) shows a significant reduction (about 27%) compared to the multihole one (Figure 6.2b). The lower ηfuel is due to both the lower combustion and thermodynamic efficiencies. The combustion efficiency, therefore, the higher THC and CO levels are significantly affected by the fuel-wall impact that causes the quenching phenomenon as confirmed by the optical diagnostics (Figure 6.3). The lower thermodynamic efficiency is related to the high late combustion duration that causes higher exhaust losses, thus exhaust temperatures (about 30°C).

From the presented results, it emerges the significantly higher soot production for HCN (about two orders of magnitude). The reason behind this is related to the not adequate air-fuel mixing with locally very rich regions (Figure 6.3)

Figure 6.3 reports a sequence of images of natural flame luminosity during the combustion process, available in the literature [1]. Images at a given combustion cycle have been reported instead of the averaged ones in order to preserve the resolution of the flames contour. The first visible reactions can be detected at about 9.4 deg ATDC, where weak flames are in the center of the combustion chamber and close to the wall on the top-left side of the image. The luminosity of the flame in the center increases faster because this zone is richer in fuel compared to the periphery that is further from the nozzle. When the fuel moves towards the chamber wall, has mixed with the air, the combustion becomes stronger also there, and more luminous flames can be detected (13.9 deg ATDC). However, the fuel on the chamber wall burns in rich conditions that would produce more soot compared to a homogeneously distributed flame. Similar considerations can be made for the fuel that burns on the optical window. As the combustion process continues, the flames on the chamber wall move according to the counterclockwise swirl motion of the air in the cylinder.

The combustion behavior depicted by the images is not the expected one for this kind of injector. It is strongly asymmetric and not homogeneous.

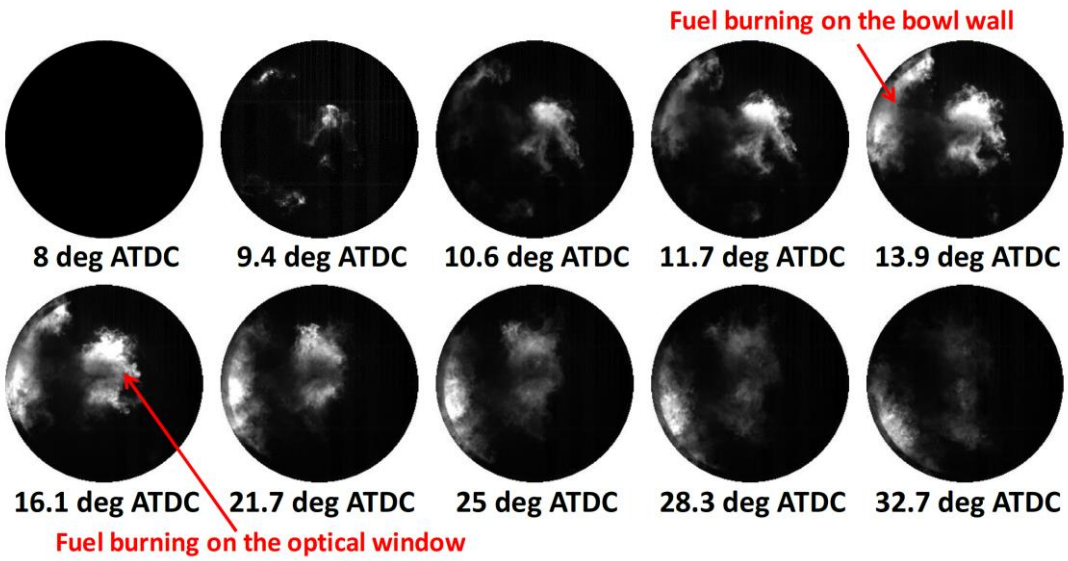

Figure 6.3 - Images of combustion processes in the optical engine at 1500 rpm and 3.3 bar of IMEP for HCN (old version) [1].

Thus, the combination of the HCN (old version) injector and the conventional combustion architecture for direct-injected compression ignition engines exhibits worse performance in terms of global emissions and efficiencies. For this reason, different nozzles geometries were developed to increase the spray cone angle (HCN) and build wall guides on the pintle to generate a spray jet (HCN-J and HCN-8J). This requirement arose from the low level of air trapped utilization in the cylinder, highlighted in HCN (old version) test campaigns.

In the following paragraphs, the test campaign on different nozzles will be illustrated carried out during the Ph.D. program.

6.2 Test methodology

The experimental campaign was aimed to assess the HCN-J and HCN-8J injectors performance on the SCE engine, which specification and the fuel adopted are reported in chapter 3. An exhaustive test campaign was only performed for HCN-J. The assessment is carried out in five steady-state engine operating points: three speeds (1500, 2000, and 2500 rpm) and three loads (2, 5, and 8 bar of BMEP). The operating points were selected since they are “key” operating conditions of the correspondent multi-cylinder engine during the execution of the NEDC [2], see Figure 6.4. These points are used for the application of a validated estimation procedure of the engine outputs of a real multi-cylinder engine of equal unit displacement during the execution of the UDC (Urban Driving Cycle) sub-cycle of the NEDC homologation cycle [3]. In

particular, Figure 6.4 identifies the selected points position in the speed-load plot of the NEDC cycle performed by a vehicle with 1490 kg of inertial mass, equipped with the corresponding four-cylinder engine. In order to facilitate the interpretation of the IMEP values of the single-cylinder engine with the outputs of the correspondent multi-cylinder engine, the operating points refer to the brake mean effective pressure (BMEP).

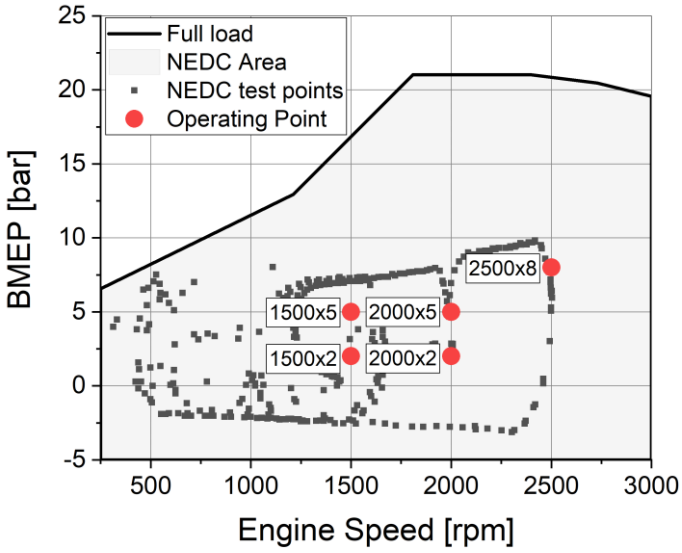

Figure 6.4 - Engine map, selected part-load test points, and operating points of a vehicle with 1490 kg of inertial mass, equipped with the multi-cylinder engine over the NEDC.

The first part is oriented to identify the optimal injector control parameters for a robust operating of the injector. The approach of this study was to assess, employing a proper designed experimental plan, the HCN performance on main injection control, and geometrical parameters. At first, a nozzle tip protrusion (NTP) analysis was performed to evaluate the interaction between the spray and piston bowl. To get different values of NTP, the thickness of the washer between the injector shoulder and the engine has been varied. Figure 4 defines the washer thickness (WT) and the NTP. This analysis allowed us to minimize both fuel consumption and emissions. The tests have been performed at an engine speed of 1500 rpm and a load of 3.3 bar of indicated mean effective pressure (IMEP) employing a practical engine parameter calibration. No Exhaust Gas Recirculation (EGR) is adopted during the test to isolate the combustion behavior from the EGR effect. It is worth underlining that, only a single injection strategy is employed, since preliminary tests have shown very high smoke levels with a conventional double injection strategy, as also demonstrated for the previous test campaign for HCN (old version) [1].

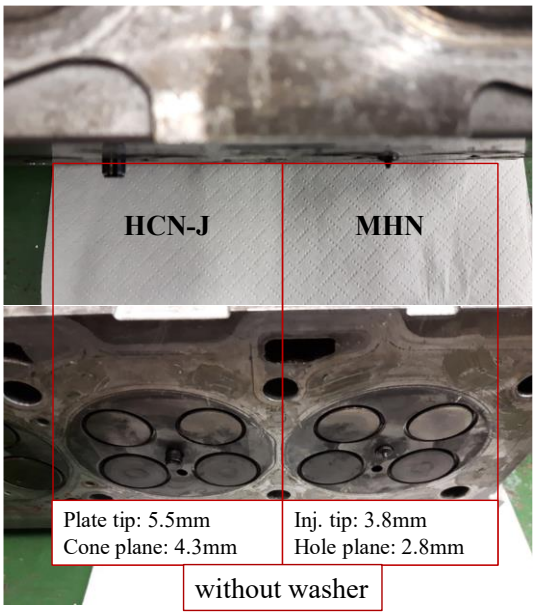

Figure 6.5 - Comparison of tip protrusion without washer between HCN-J and MHN.

The engine operating parameters used during the NPT sweep are reported in Table 6.1. The injection strategy adopted was a single injection pulse, and eight washer thickness (WT) levels were adopted.

Table 6.1 -Washer thickness vs. fuel outlet area protrusion.

WT [mm]	Protrusion Fuel outlet area [mm]
1.5	2.8
1.8	2.5
2.0	2.3
2.2	2.1
2.5	1.8
3.0	1.3
3.5	0.8
4.0	0.3
(Ref. MHN) 2.0	**0.8**

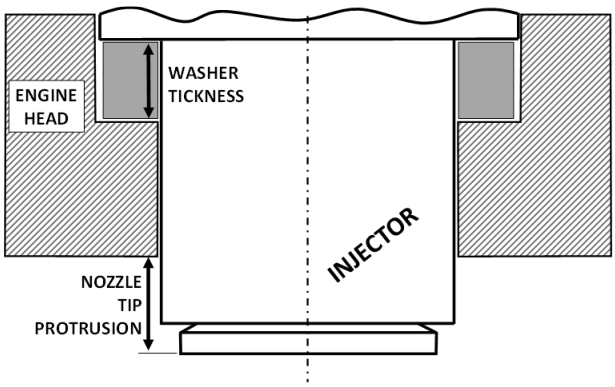

Figure 6.6 - Description of the Washer Thickness (WT) and Nozzle Tip Protrusion (NTP) concepts.

Subsequently, the current injection parameterization was performed in terms of opening/closing current and time that determines the speed of the needle opening and closure. Finally, the charging voltage (HV) effect was analyzed. The parametric NTP, injection current profile, and charging voltage analyses represent essential phases for the optimization and validation of the injector and engine performance. The main operating parameters and the test point, adopted in this first assessment, is reporting in the following table.

Table 6.2 - Test point and main operating parameters.

Injector	**[rpm] x [bar]**	**p_{rail}[bar]**	**Voltage[V]**	**Washer Thickness [mm]**
HCN-J	1500 x 3.3	620	90; 100; 110; 120; 150	1.5; 1.8; 2.0; 2.2; 2.5; 3.0; 3.5; 4.0

Subsequently, a comparison between the HCN-J prototype and MHN in terms of combustion characteristics, emissions, and efficiencies on the engine is shown. Starting from the reference calibration reported in Table 6.3, adopted in CDC mode and derived from the reference multi-cylinder Euro 5 engine, a single parametric analysis (varying one parameter per time) was performed keeping constant the others. During the analysis, no EGR was applied in order to isolate the effects of the parameter's variation. The SoI of the complete injection pattern was varied in order to keep constant the combustion phasing (equal to the base Euro5 set), and it was only varied during the combustion phasing parametrization. In the thesis, notations like

1500x2 (i.e., rpm x BMEP) are assumed to define the test points. It is worth to remark that the methodology and constraints used were designed to make the results easily transferable to the application on modern diesel engines.

Table 6.3 - Selected steady-state test points and engine calibration parameters of interest (Euro 5 diesel base calibration).

Test point [speed x bmep]	bmep [bar]	imep [bar]	p_{boost} [bar]	T_{intake} [°C]	CA50 [deg]	p_{rail} [bar]
1500x2	2.0	3.3	1.03	63	7.7	620
1500x5	5.0	7.0	1.15	60	9.7	780
2000x2	2.0	4.0	1.07	65	9.8	720
2000x5	5.0	7.0	1.20	63	9.0	880
2500x8	8.0	10.5	1.60	65	9.5	1250

Table 6.4 reports the variation range of each parameter assessed, taking into consideration that the test campaign was carried out only at partial load (except 2500x8) and the SoI parametrization only for 2 and 5 bar of BMEP at 1500 rpm. The variation of each parameter is applied maintaining the others constant; i.e., during the rail pressure sweep at 1500 rpm and 2 bar of BMEP, the EGR and CA50 are kept constant at values of 0%, 7.7 deg aTDC respectively and equal to the base calibration dataset reported in Table 6.3. The rail pressure parametrization was also performed with the HCN-8J.

Table 6.4 - Parameters variation ranges for all parameters investigated mode at four key points at Partial Load.

Parameters	Injector	1500x2	1500x5	2000x2	2000x5
p_{rail} [bar]	HCN-J, HCN-8J	420-620-820	580-780-980	520-720-920	680-880-1080
SOI [deg aTDC]	HCN-J	7.5-9.5-11.5	9.5-11.5-13.5		
Charging Voltage [V]		110-150			

Literature results and previous authors experiences confirm that the main issues of a DI engine are the simultaneous control of the peak pressure rise rate (PRRmax), the coefficient of variation of IMEP (COVimep) and for these reasons, during the experimental assessment they were limited to the values reported in Table 4.3. The limit of 160 bar of peak firing pressure (pfp) is imposed as engine thermomechanical

limit while the 80 bar/ms PRRmax limit is to preserve the comfort standards as requested for modern diesel passenger cars. The maximum COVimep of 3.0% is considered as acceptable cycle-to-cycle combustion stability and comparable to that of SI engines. The used methodology and constraints described up to now are designed to make the results easily transferable to the application on modern diesel engines.

Table 6.5 - Constraint values on the engine operating conditions adopted during the test campaign.

Constrain	max. value
PRR_{max} (pressure rise rate)	80 bar/ms
pfp (peak firing pressure)	160 bar
COV_{imep} (Coefficient of Variation)	3.0%

6.3 Injection parameters analysis

A parameterization on the injection washer thickness was assessed for the HCN-J on the single-cylinder engine to find the optimal nozzle thickness protrusion (NTP) for the best spray-piston bowl interaction. The engine operating parameters used during the NPT sweep are reported in Table 6.1. The injection strategy adopted was a single injection pulse, and eight washer thickness (WT) levels were adopted. Figure 6.7 shows the soot emissions and isfc trends by varying the washer thickness. The HCN-J injector exhibits a quite constant value of soot while the lowest isfc is for WT=2 mm. Hence, this WT value is used in the following tests.

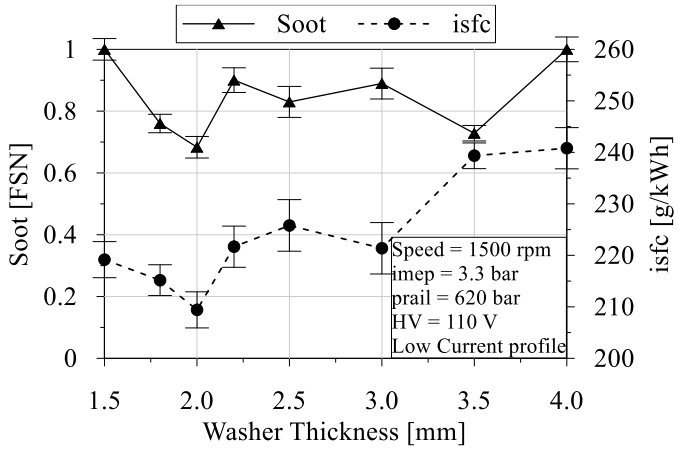

Figure 6.7 - Soot and isfc trends varying the injection washer thickness.

After the NTP assessment, the current injection profile and the charging voltage were analyzed for the HCN. Starting from the current injection profile, two different values were used at 110 V of charging voltage. The injector current phase (Iphase)

settings of 2 and 8 A, which charging voltage profiles are shown in Figure 6.8. Due to hardware problems, the parameterization in the current phase, could not be carried out in terms of spray characterization. The two values are the minimum and maximum values of the different interval suggested by the OEM that has built the injector. In particular, this is the Iphase injector command parameter that controls the opening phase of the needle. Increasing the Iphase value, the needle lift achieves earlier the max lift value. The combustion logic used for the tests was to keep the combustion phasing (CA50) constant for both current injection profiles and, for this reason, different Start of Injection (SoI) values were required. Meanwhile, in Figure 6.8, the tests with the same SoI are reported. Both injection patterns have the same fuel mass flow rate of 0.42 kg/h ± 1%. By adopting a high injection current profile (8 A), about 1 CA degree is necessary to achieve the imposed HV target (110 V), and that corresponded to the fully open flow section. When adopting the low injection current profile (2 A), about 3.5 CA degrees were necessary to achieve 110 V. As a consequence, with the low injection current profile, the End of Injection (EoI) was delayed obtaining the same injected fuel mass. Thus, increasing the current injection values, the faster response of the injector during the opening phase was observed.

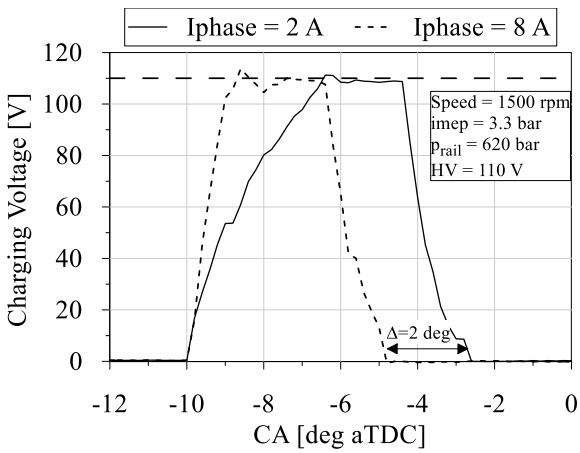

Figure 6.8 - Charging voltage profile function of the injection current.

Figure 6.9 reports the Heat Release Rate (HRR) and the charging voltage profile by varying the current injection profile. The SoI values change to keep constant the CA50. A lower HRR peak can be observed for the high injection current profile (8 A) compared to the low one (2 A). The faster response of the injector opening phase, obtained with 8 A, permitted to improve the combustion stability expressed in terms of Coefficient of Variation on IMEP (COV_{imep}), which was about 1.6 %; compared to 3.7 % for the 2 A case. The latter is above the acceptable limits of current diesel engine

standards. The higher injection current during the opening phase of the nozzle led to lower smoke emissions and isfc of about 25 % and 2.7 %, respectively, compared to the 2 A case. Also, the THC and CO were reduced by adopting the higher Iphase value. The improvement was about 1.5 % of the units of combustion efficiency.

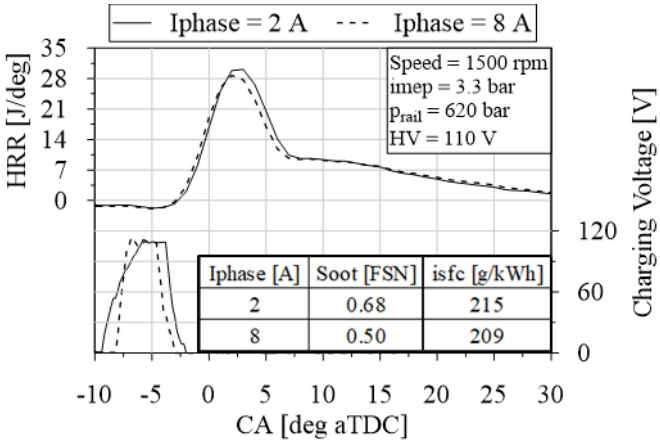

Figure 6.9 - HRR traces for two different injections' current profile.

Finally, the effects of maximum charging voltage variation are investigated on combustion, emissions, and engine performance. The maximum charging voltage (HV) is directly linked to the maximum needle lift, by increasing the charging voltage, an increase of needle lift is observed. Figure 6.10 reports the soot emissions and isfc for different values of charging voltage, no linear trends are detected for the isfc and soot emissions varying the charging voltage. Lower fuel consumption and soot are obtained with HV of 110 V. High values of charging voltage up to 150 V results in a high level of soot and isfc. This phenomenon is not straightforward.

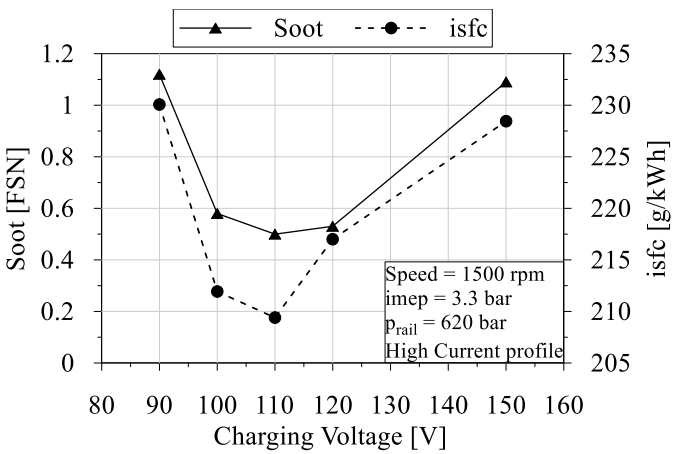

Figure 6.10 - Soot and isfc trends varying the charging voltage.

However, a possible hypothesis is that a high charging voltage hurts the atomization spray levels causing rich mixtures in the region of the needle and then producing high soot emissions. Figure 6.11 reports the charging voltage injection profile at different values of HV. Increasing the HV and keeping constant the fuel mass flow rate, a reduction of energizing time was necessary.

This preliminary analysis has permitted us to choose the optimal injector command parameters and washer thickness concerning emissions, efficiency, and combustion stability. However, notwithstanding the optimization, the HCN soot level is about one order of magnitude higher compared to the standard multi-hole injectors. Considering the evolution of the spray, analyzed in the previous chapter, the 110 V tip penetration, lower than the other one (150 V), guarantees an optimal compromise to the air-fuel mixing.

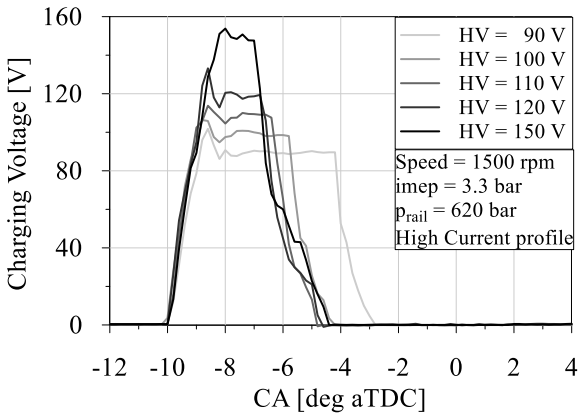

Figure 6.11 - Charging voltage profile varying the high voltage (HV).

6.4 HCN-J vs. MHN

Figure 6.12 shows the in-cylinder pressure, injection profile, HR, and HRR trends for both injectors, the MHN and HCN-J, and for the operating conditions 1500x4.2 (Table 2, point 1). The start of injection (SoI) for the HCN-J injector is set to get the same combustion center (MBF50%) of the MHN injector. The selected MBF50% value is considered to be the best compromise in terms of emission-efficiencies trade-off, and it derives from the Eu5 engine calibration employing the MHN. It is clear that this value is only a starting point, and it could not be the optimal one for the HCN. In this sense, further investigations are needed. The resulted trends and discussion are valid for all the tested points; therefore, for brevity, the results are presented only for

the point 1500 rpm and 2 bar of BMEP. However, since the emissions and efficiencies are useful for the discussion, they are presented for all the points (Figure 6.16).

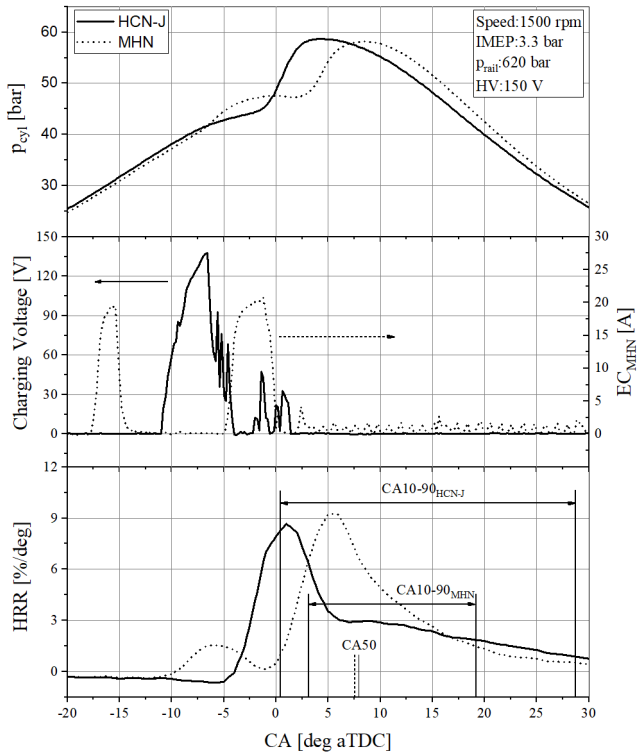

Figure 6.12 - Comparison of in-cylinder pressure, injection energizing pattern, HRR at 1500 rpm, and 2 bar BMEP, for HCN-J and MHN.

As already pointed out, the engine was operated with a single injection strategy when employing the HCN injector. Notwithstanding the single injection strategy, the HCN combustion shows comparable Heat Release (HR), during the premixed combustion phase, but significantly lower values during the diffusion and late combustion phases. The combustion shifts towards the late combustion phase (Figure 5), increasing the MBF50-90% (crank angle interval between MBF50 and MBF90) significantly (Figure 6 c). However, looking at the HCN results, they are globally worse compared to the MHN injector. The longer combustion duration (calculated as MBF10-90%), in particular, the late combustion phase (MBF50-90%), is attributed to the worse air-fuel spray interaction impacts negatively on the mixing-controlled combustion phase [4].

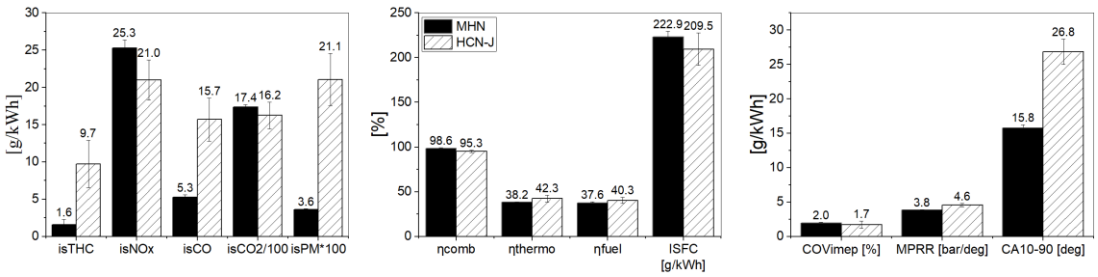

Figure 6.13 - Specific emissions, efficiencies, COV, PRR, and MBF10-90% at 1500 rpm and 2 bar of BMEP for HCN-J and MHN.

When using the HCN injector, the global indicated efficiency (η_{fuel}) shows a significant increase (about 2.7%) compared to the multi-hole one (Figure 6.13). The higher η_{fuel} is due to the greater thermodynamic efficiencies. The combustion efficiency than the higher THC and CO levels are significantly affected by the fuel-wall impact that causes the quenching phenomenon as confirmed by the optical diagnostics discussed in the previous chapter. The higher thermodynamic efficiency is related to the high late combustion duration that causes higher exhaust losses, thus exhaust temperatures (about 15°C).

From the presented results, it emerges significantly higher soot level for HCN-J that is about two orders of magnitude higher. The reason is related to the not adequate air-fuel mixing that leads to very locally reach regions.

Figure 6.13 also reports the trends of the maximum pressure rise rate (PRRmax), coefficient of variation of the mean effective pressure (COVIMEP) for both injectors. Using the HCN-J, the PRRmax and the COVIMEP reduce congruently to the discussion about the HR and HRR.

In order to provide a more detailed understanding and description of the results obtained on the metal engine, optical analysis of the injector behavior in the cylinder has been performed through an optical engine which characteristics are reported [5].

Hence, to explain and support the observations made about macroscopic measurements as in-cylinder pressure and engine-out emissions, the images of the injection and combustion process, available in the literature [5], have been employed and reported below.

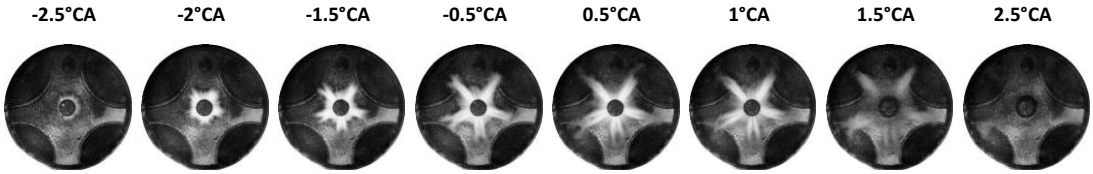

Figure 6.14 - Images of the liquid spray evolution in the optical engine for HCN-J.(1500x2, #1 Table 6.2) [5].

Figure 6.14 reports a collection of injection images for HCN-J from the start to the end of the injection process. At the start of injection (-2.5 CA degree), the fuel exits from the nozzle with a circular shape as described in the previous chapter, at -2 CA degree, the fuel guided by the nozzle geometry accelerates, forming five protuberances from the annulus cloud. The tip penetration of the compact jets is more than twice that of the circular region, ensuring better air utilization. After the injector closure, at 1.5 CA, only the five jets can be detected in the combustion chamber while the fuel in the circular cloud is evaporated [5].

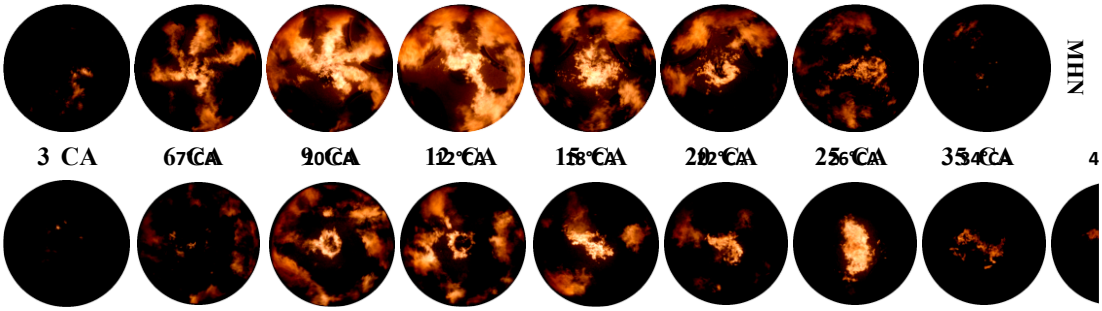

Figure 6.15 - Images of the evolution of the luminous flame in the optical engine for MHN and HCN-J. (1500x2, #1 Table 6.2) [5].

Figure 6.15 reports a sequence of visible flames images recorded during the combustion process for the injectors MHN and HCN-J. At first sight, a different distribution of the flames in the combustion chamber is noted. For MHN, the first luminous flames are detected at 3 CA degrees, during the premixed combustion phase. In the following crank angles (6-20 CA degree), they form a quite homogeneously bright flame, located in the center of the combustion chamber and on the liner thanks to the air swirl motion. On the other hand, for the HCN-J, where the fuel is delivered in the center and the periphery of the combustion chamber, the flame distribution is different. As first, the occurrence of visible flames is retarded compared to MHN; the first luminous flames are detected at 6 CA degree. These are located close to the chamber wall and are relative to the combustion of the five jets that penetrated deep in

the combustion chamber. The lower air-fuel mixing compared to the MHN, causes a not homogeneous fuel distribution in the combustion chamber.

Moreover, while the fuel on the periphery of the chamber continues to burn, bright flames appear under the nozzle (12-20 CA degree). The intense luminosity of these flames suggests that this location is rich in fuel, likely due to a low-pressure fuel delivery during the injector closure. The flames are still evident in the center of the bowl at the end of combustion (35 CA deg); while they extinguish in the periphery of the chamber, where a low quantity of fuel was delivered.

For the reasons mentioned at the beginning of the paragraph, the efficiencies and emissions are illustrated for all operating test points (Figure 6.16). It is essential to point out that the MHN test points were carried out by adopting a double injection strategy, while for HCN-J only using the main injection.

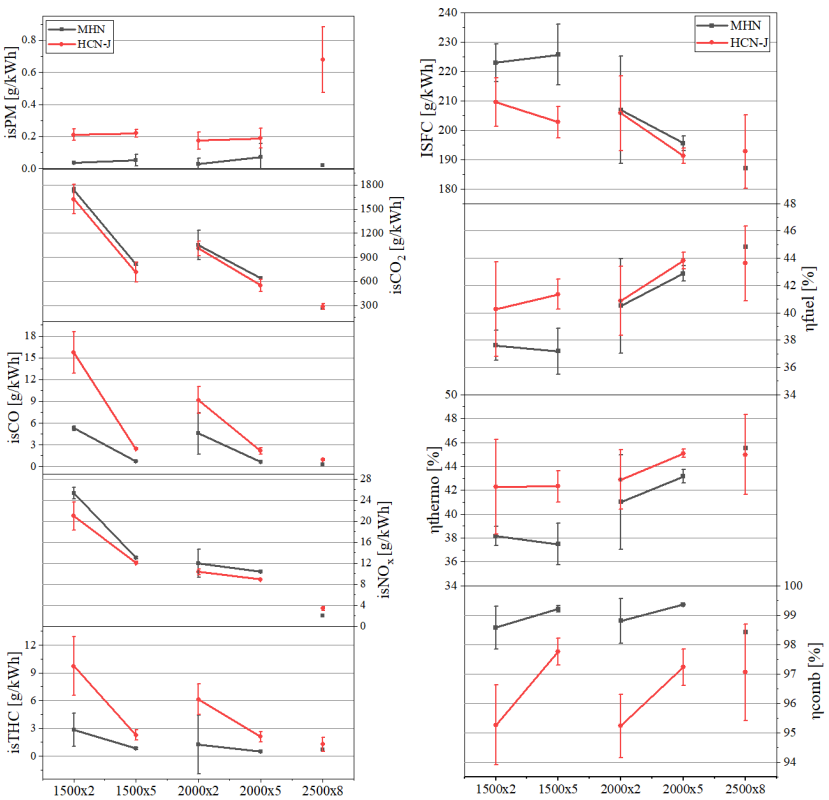

Figure 6.16 – Emissions and efficiencies trace for all the test points.

The higher η_{fuel} for the HCN-J injector is due to both the thermodynamic and combustion efficiencies. The lower thermodynamic efficiency obtained for the HCN-J, as well as, the lower combustion performance is validated what emerged in the analysis of the 1500x2 test point (Figure 6.13). The fuel consumption (ISFC) confirms

the η_{thermo}, in particular, the gap is reduced with the increase of the load. The trend is not confirmed only for the higher load, 2500x8, in which the less repeatability for HCN-J influences the results and, therefore the analysis. At the end of the chapter, a paragraph was dedicated to better analyzing the high-load point, where the results of the HCN-8J injector will be compared.

In Figure 6.16, the comparison between the two injectors is reported in terms of specific emissions. It was observed an increase of PM, THC, and CO and the corresponding modification of NO_x.

This result is influenced by air-fuel mixing speed because of a lower injection phase for the HCN-J than to MHN one [6]. For this reason, it has observed a shifting the combustion towards more diffusive conditions, and therefore a poor fuel premixing in the first phase of the combustion. An increase of PM is observed, while the high values of THC and CO emissions are due to excessive combustion duration, as shown in Figure 6.12 (HRR). As shown in the optical engine, penetration of air-borne droplets and the fuel evaporation, a significant amount of fuel vapor tends to penetrate a short distance and stay in the center region of the cylinder. The fuel in this region cannot use the air in the outer squish region near the piston lip and piston top surfaces [7]. Thus, THC and CO emissions increase. At the same time, the combustion temperatures are lower than the MHN with backlash on the formation of NO_x.

6.5 Start of Injection

In order to investigate the effect of main injection timing variation, the main injection for HCN-J, the timing was varied from 11.5 to 7.5 and 13.5 to 9.5 deg aTDC, respectively 2 and 5 bar of BMEP at 1500 rpm.

The tests are performed at fixed engine calibration parameters (such as p_{boost}, p_{back}, p_{rail}, charging voltage, etc.), engine load (i.e., imep), and without employing the EGR and pilot (only the main injection). In-cylinder pressure, HRR, and current injection profiles are shown in Figure 6.17, compared to the MHN reference calibrations point.

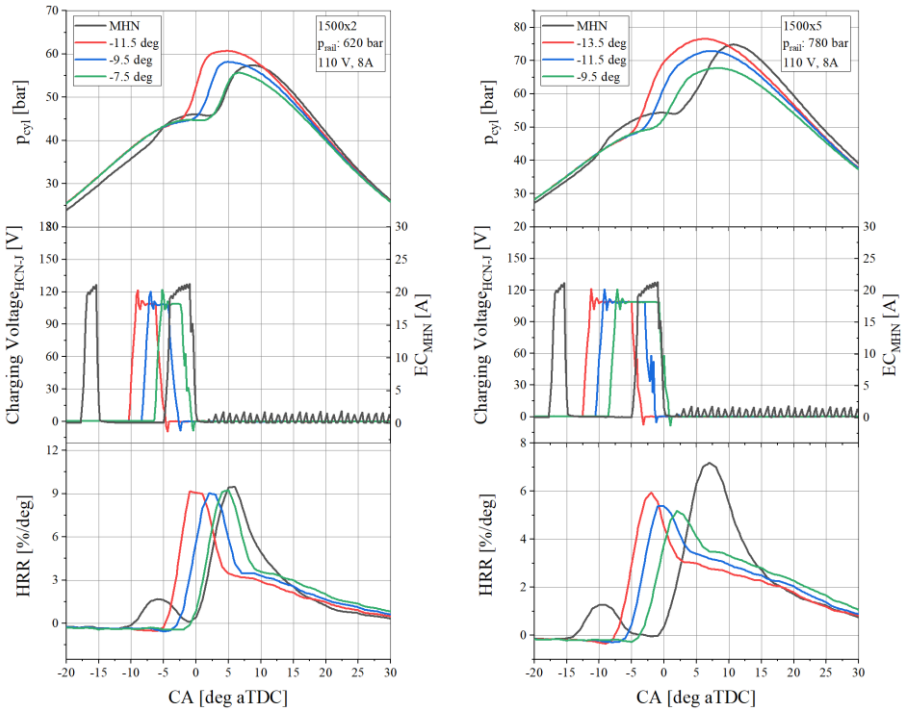

Figure 6.17 - SoI variation effect on in-cylinder pressure, current injection profile and HRR versus crank angle at 1500 rpm and 2 (left),5 (right) bar of BMEP, No EGR.

First of all, it has observed the different in-cylinder pressure traces between the two nozzles, due to the different injection strategies. In particular, in the case of the MHN, it was adopted the EU5 calibration, reported in Table 6.2. The single-injection strategy was instead applied for HCN because it shows more modest HRR (less combustion noise).

As injection timing was advanced, ignition timings were advanced, and peak heat release rates and maximum pressure rise rates increased (Figure 6.17). This indicates that the main injection timings significantly influence noise levels, which are strictly correlated with the maximum pressure rise rate.

Furthermore, a prolonged heat release for the HCN injector is observed, which indicates that the combustion duration is longer than the MHN, and this causes a worsening of the thermodynamic efficiency. To confirm this remark, figure 4.8 shows the SoI variation effect on combustion duration (CA90-10); the HCN-J values are about 10 deg greater than in the MHN case, for both tests point, in the SoI reference. The cause of the increase in the CA90-10 may be related to a slower air-fuel mixing of the HCN injector compared to the MHN.

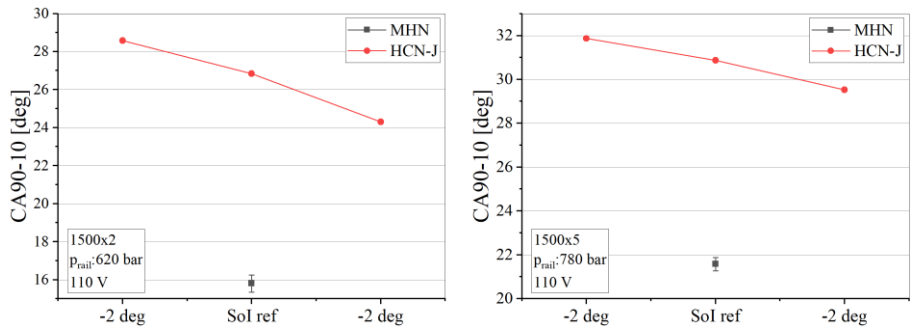

Figure 6.18 - SoI variation effect on CA90-10 at 1500 rpm, and 2 (left), 5 (right) bar of BMEP, comparing to MHN reference calibration point.

PM, NOx, THC, and CO emissions for various injection timings, for both test points are shown in Figure 6.19.

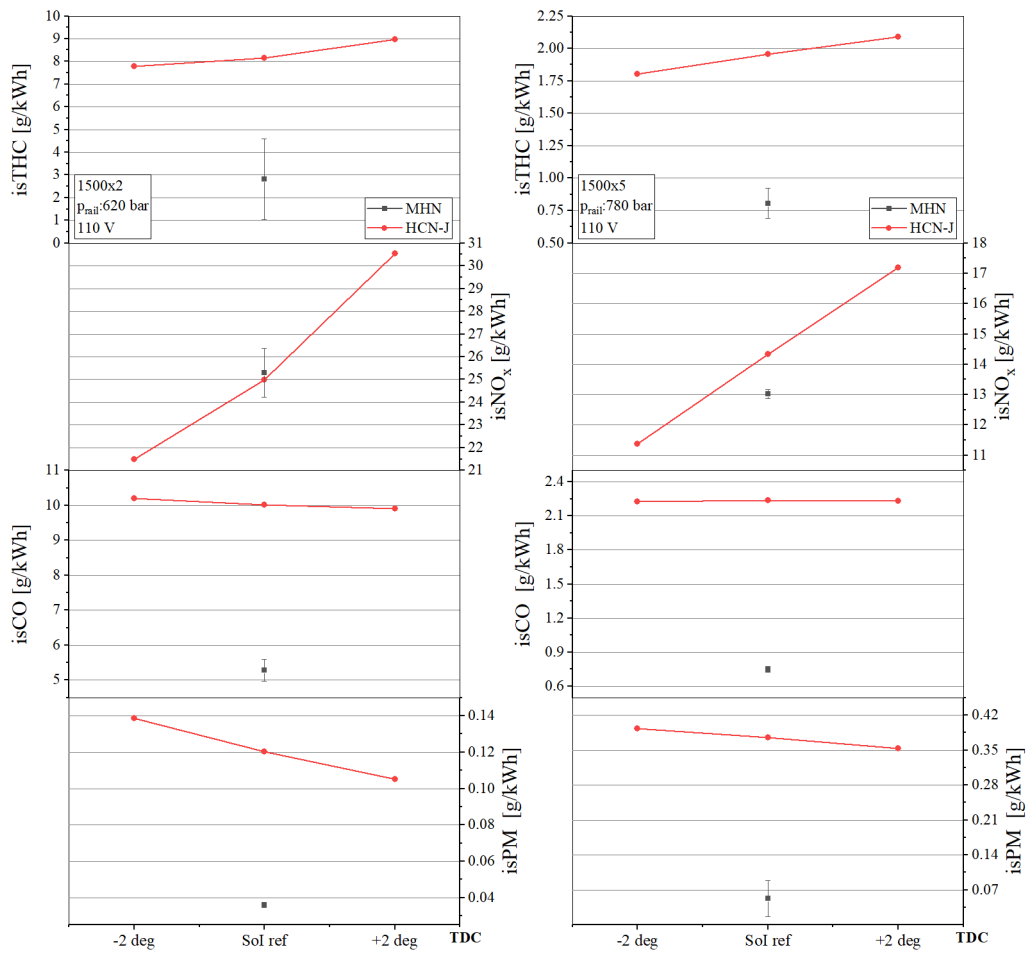

Figure 6.19 - SoI variation effect on specific emissions at 1500 rpm, and 2 (left), 5 (right) bar of BMEP, comparing to MHN reference calibration point.

The soot emissions are seen to decrease as the main injection is advanced towards TDC, it is due to the more significant premixed combustion phase compared to diffusive one, and therefore, a corresponding increase in NO_x [7, 8].

However, for extremely late injection, combustion becomes weaker due to too low gas temperatures; thus, THC formation increases and CO emissions maintain similar levels [7]. These remarks are valid for both test points analyzed.

6.6 Rail pressure

The assessment of the rail pressure variation effects on emissions and efficiency is discussed. Again, all the tests are performed without EGR and adopting the Euro5 calibration dataset at constant load. Obviously, as a consequence of the no EGR, the NOx assessment is of minor importance since they are higher and not representatives of the reference Euro5 calibration. The results of both injectors HCN-J and HCN-8J will be illustrated and compared with the classic MHN using the conventional double-injection strategy (pilot + main).

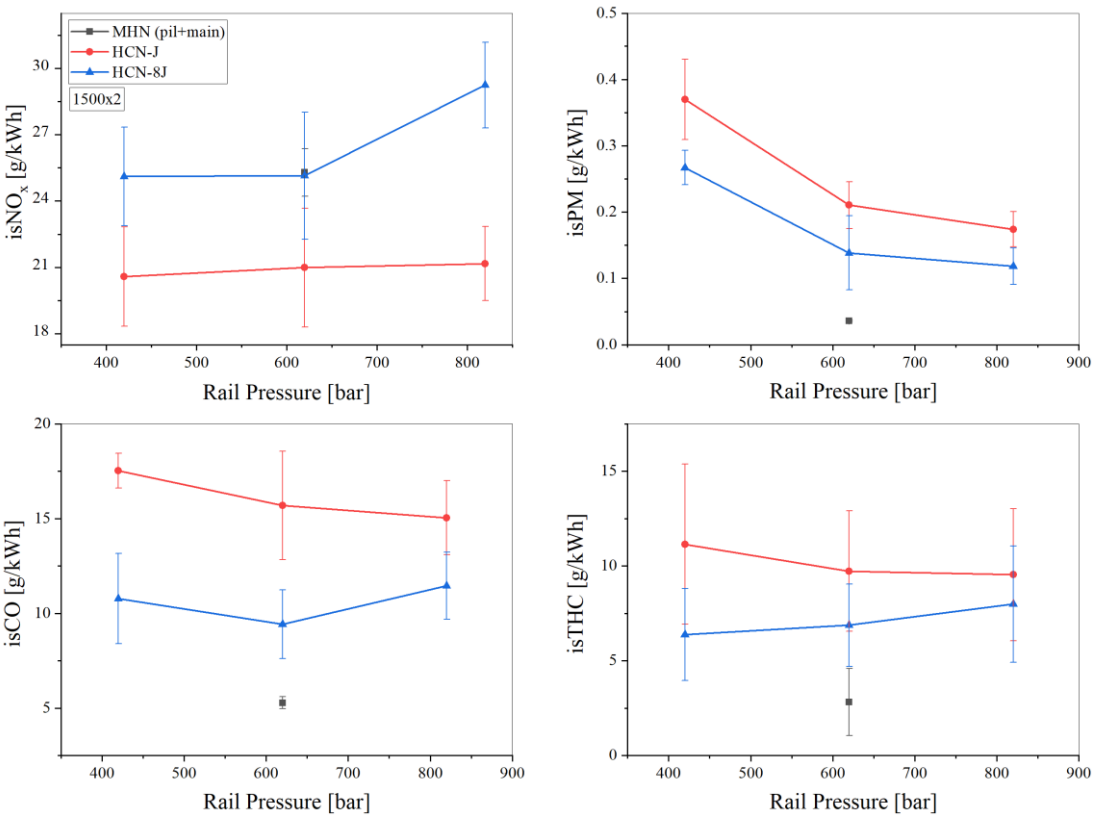

Figure 6.20 - Effect of the rail pressure variation on the specific emission for the test point 1500x2, without EGR, HC 110V.

The pollutant emissions for the operating point 1500x2, and both nozzles are shown in Figure 6.20. As for the previous parametrizations described above, also, in this case, there is an increase in the HC, CO, and PM compared to the case of the MHN and a reduction of NOx. It is due, as mentioned above, to scarce atomization and penetration of the HCN compared to the MHN.

However, it is interesting to highlight also for this nozzle, the increase of the injection pressure maintains a strong influence on PM emissions, showing, as reported in many works in the literature, the correlation very similar to MHN [9].

For this reason, it could be possible to operate with high injection pressures that would allow reaching PM emission levels comparable to the multi-hole, since passing from the minimum to the maximum injection pressure, PM emissions are reduced of about 50%, for both injectors.

The PM graph, Figure 6.20, also shows a marked difference between the HCN-J and HCN-8J, in favor of the latter. The analysis of heat release, not reported for the sake of brevity, showed no significant differences, and probably it could be due to the more excellent radial distribution of the fuel for the HCN-8J compared to the other one.

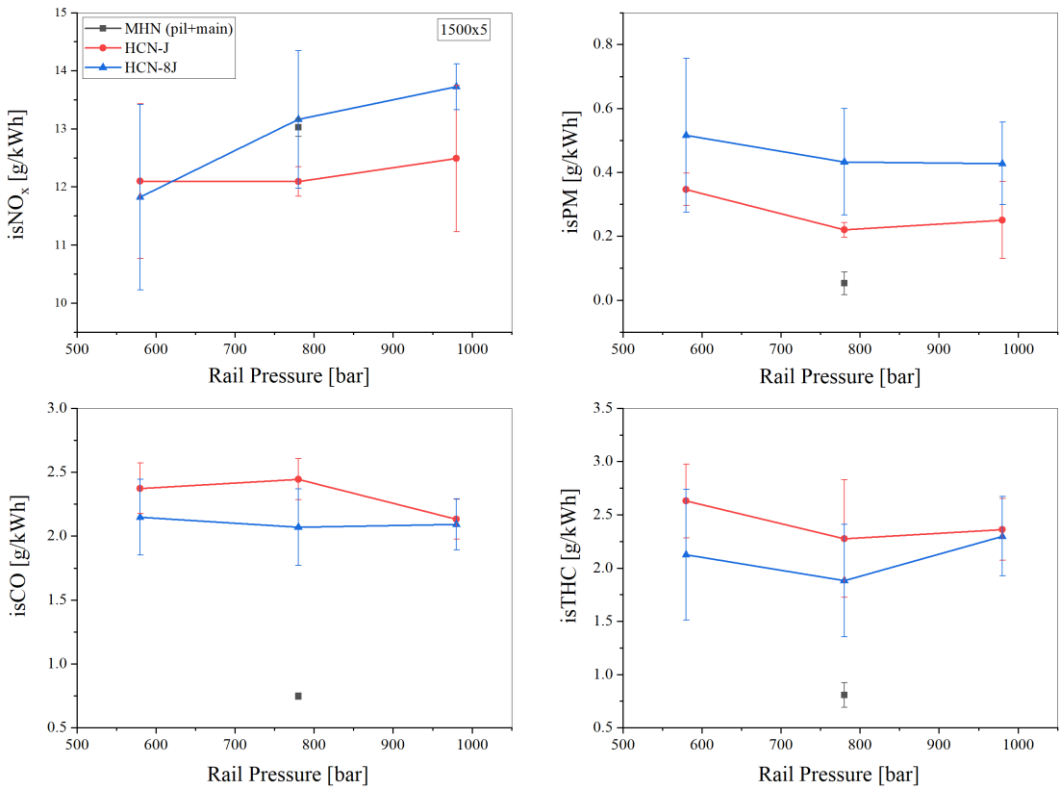

Figure 6.21 - Effect of the rail pressure variation on the specific emission for the test point 1500x5, without EGR, HC 110V.

The pollutant emissions for test point 1500x5 for both prototypes show a trend reversed compared to 1500x2. In this operating point, the HCN-8J has a more significant amount of PM than HCN-J, (see Figure 6.21). Furthermore, the increase in injection pressure is less effective than the operating point of 1500x2. For the other pollutants, although there are differences, they are much less marked.

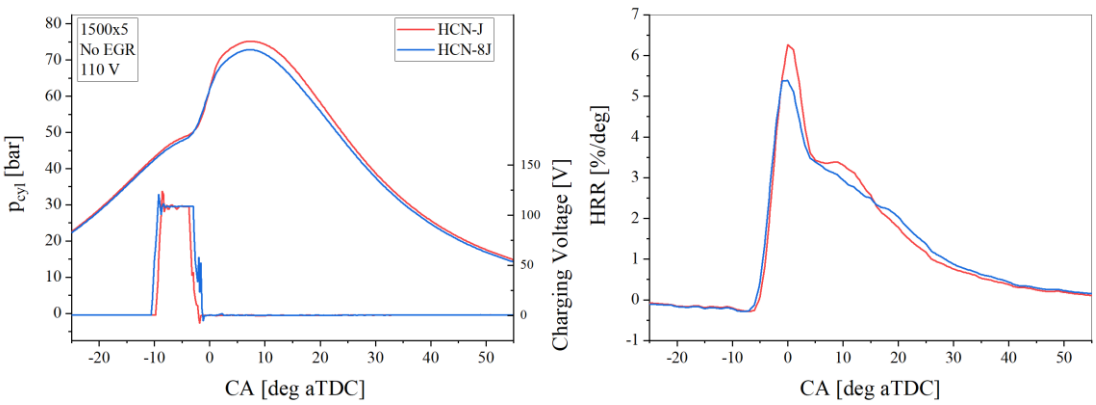

Figure 6.22 - Effect of the rail pressure variation on the in-cylinder pressure and heat release rate at 1500x5 for both injectors (HCN-J and HCN-8J).

The in-cylinder pressure and the heat release rate traces for both nozzles (Figure 6.22) show combustion characterized by a more diffusive phase than to the premixed one for the HCN-8J, with a significant increase of the injection duration. Both causes may justify the PM result obtained, thus indicating a reduction in the permeability of the nozzle compared to HCN-J in this operating point. In these conditions, the functional characteristics of the HCN-8J cancel the benefits from the more excellent annular fuel distribution based on 8 radial jets instead of 5.

In the operating test points 2000x2 and 2000x5, the trends show further different behaviours compared to the test points at 1500 rpm.

First of all, the injection pressure effect is less marked, as well as the differences between the two nozzles. In general, it is observed a higher sensitivity to the injection pressure for the HCN-8J.

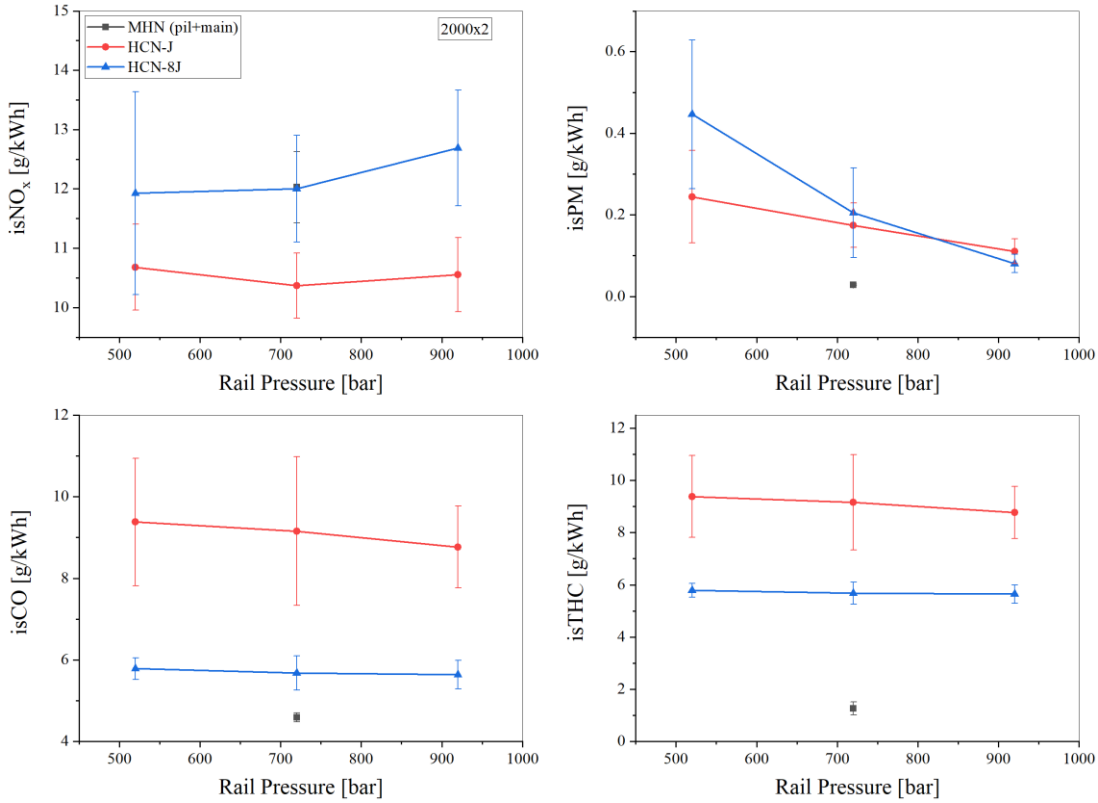

Figure 6.23 - Effect of the rail pressure variation on the specific emission for the test point 2000x2, without EGR, HC 110V.

For both of these operating points, it is observed a lower THC and CO emissions with HCN-8J (Figure 6.23 and Figure 6.24). Compared to the previous diagrams, the increase in the radial distribution of the fuel through the adoption of the HCN-8J tends

to reduce unburnt gaseous emissions. The HCN emissions are always higher than the reference injector (MHN). This result is confirmed for all operating points.

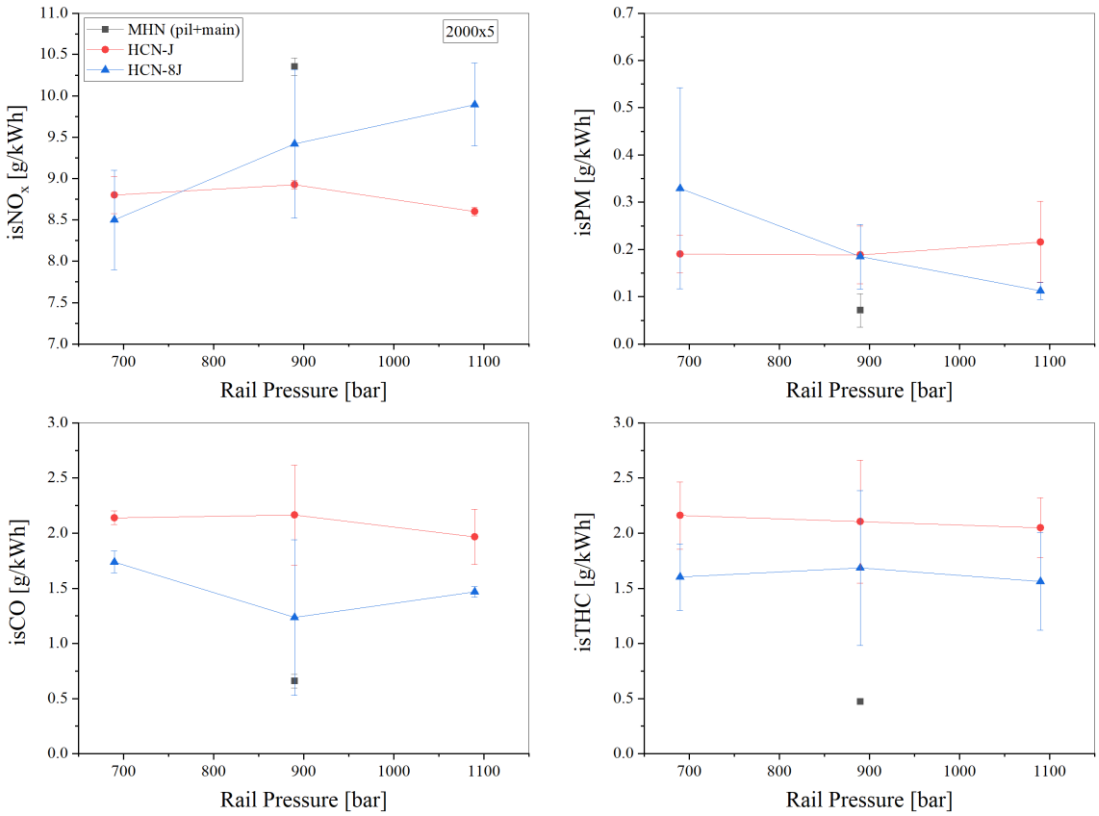

Figure 6.24 - Effect of the rail pressure variation on the specific emission for the test point 2000x5, without EGR, HC 110V.

In general, the injection pressure effect on emissions can be concluded that the NOx emissions increase with the rail pressure due to higher premixed combustion at lower engine speed, while it remains almost constant at a higher speed. THC and CO are quite insensitive to the rail pressure variation but more to the load conditions [9]. They are lower for the lower load points. For the sake of brevity, the results at 2000 rpm and 2 and 5 bar of BMEP will be illustrated in the following chart (Figure 6.25) compared with the reference MHN traces.

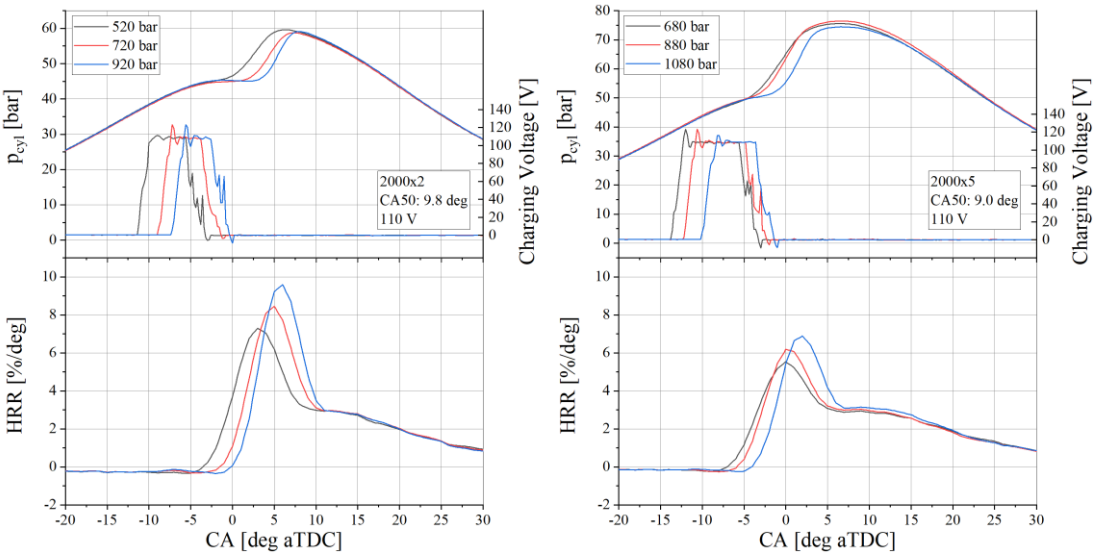

Figure 6.25 - Effect of the rail pressure variation on the in-cylinder pressure and heat release rate at 2.0 and 5.0 of BMEP and 2000 rpm.

Looking at the in-cylinder pressure and HRR traces in Figure 6.25, increasing the injection pressure, the peak of HRR increases for both engine loads (2.0 and 5.0 bar of BMEP). More heat is released before the TDC with higher p_{rail} values, and then penalties on the efficiency (higher heat transfer loss) for both tests point.

6.7 Medium load analysis

The maximum load performed was the 2500x8 operating point because the constrain imposed for the particulate emissions of 2.5 FSN (see paragraph 2.11.4) was exceeded, with both prototypes. This is the limit imposed by OEM companies to guarantee the optimal functioning of the DPF installed on the after-treatment systems.

The smoke level obtained in the engine-out for both prototypes is shown in the following figure.

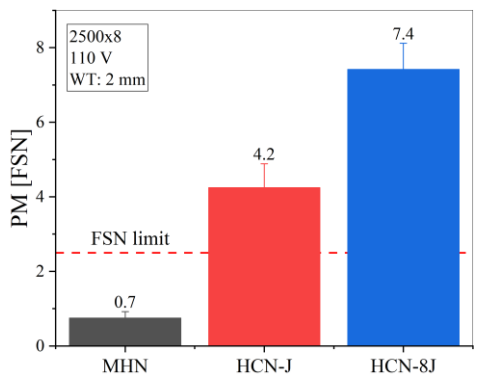

Figure 6.26 - Particulate emissions [FSN] for the three injectors compared.

However, the test points were only carried out with the nominal calibration Euro 5 of the engine, and the parametrization was not performed, since, for this operating point, there would be problems of oil's lubricating and of excessive particulate emissions.

In-cylinder pressure, HRR, and current injection profiles are shown in Figure 6.27, compared to the MHN reference calibrations point.

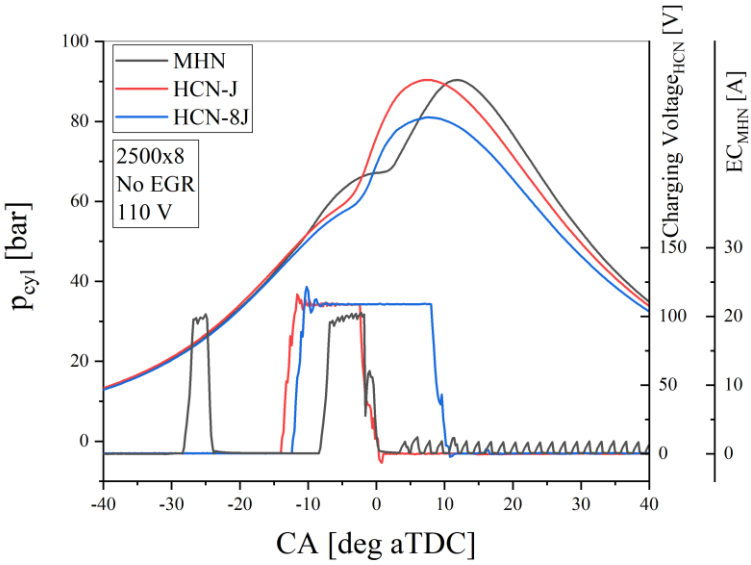

Figure 6.27 – In-cylinder pressure and energizing current comparison at 2500x8 for both injectors (HCN-J and HCN-8J).

For this test point at 1230 bar of rail pressure (Figure 6.27), the HCN-8J behavior is very different in terms of injection duration compared to the other prototype. The energizing current profile for HCN-8J is more prolonged, approximately 20 deg (8 deg more), than the other one. Therefore, the HCN-8J injection phase is characterized by a lower flow rate (as already observed in 1500x5). This lower instantaneous flow rate, which therefore requires a longer injection duration, is undoubtedly one of the characteristics that, beyond the spray evolution, contributes to increasing the smoke emission.

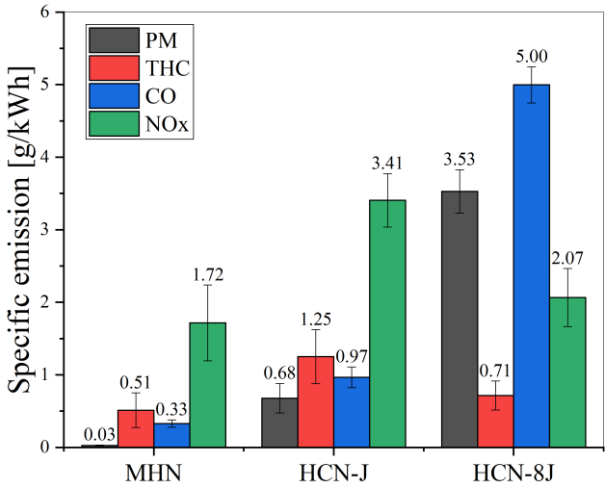

Figure 6.28 - Emissions comparison at 2500x8.

Beyond the smokiness values, much higher than the imposed limit, also the other engine-out emissions (Figure 6.28), in particular, CO emission, are much higher than the MHN reference. In this operating point, a reduction of the number of jets would seem to have more considerable advantages, although it is not possible to reach comparable values with respect to the conventional injector.

The experimental test campaign has undoubtedly shown the positive effects on the radial distribution of the spray with HCN-8J, but at higher loads, it has observed a reduction of the instantaneous flow of the injector, resulting in longer injection duration and a noticeable increase in smokiness.

REFERENCES

[1] C. Beatrice, G. Belgiorno, G. Di Blasio, E. Mancaruso, L. Sequino, and B. M. Vaglieco, 'Analysis of a Prototype High-Pressure "Hollow Cone Spray" Diesel Injector Performance in Optical and Metal Research Engines', SAE Technical Paper, 2017.

[2] G. Di Blasio, G. Belgiorno, and C. Beatrice, 'Effects on performances, emissions and particle size distributions of a dual fuel (methane-diesel) light-duty engine varying the compression ratio', *Applied energy*, vol. 204, pp. 726–740, 2017.

[3] G. Di Blasio, G. Belgiorno, C. Beatrice, V. Fraioli, and M. Migliaccio, 'Experimental evaluation of compression ratio influence on the performance of a dual-fuel methane-diesel light-duty engine', *SAE International Journal of Engines*, vol. 8, no. 5, pp. 2253–2267, 2015.

[4] J. Jeon and S. Moon, 'Ambient density effects on initial flow breakup and droplet size distribution of hollow-cone sprays from outwardly-opening GDI injector', *Fuel*, vol. 211, pp. 572–581, 2018.

[5] L. Sequino, G. Belgiorno, G. Di Blasio, E. Mancaruso, C. Beatrice, and B. M. Vaglieco, 'Assessment of the New Features of a Prototype High-Pressure "Hollow Cone Spray" Diesel Injector by Means of Engine Performance Characterization and Spray Visualization', SAE Technical Paper, 2018.

[6] Z. A. Kuensch, S. Schlatter, K. Keskinen, T. Hulkkonen, M. Larmi, and K. Boulouchos, 'Experimental investigation on the gas jet behavior for a hollow cone piezoelectric injector', SAE Technical Paper, 2014.

[7] J. A. Badra *et al.*, 'Numerical simulations of hollow-cone injection and gasoline compression ignition combustion with naphtha fuels', *Journal of Energy Resources Technology*, vol. 138, no. 5, p. 052202, 2016.

[8] J. B. Heywood, 'Internal combustion engine fundamentals', 1988.

[9] K. G. Johnson, K. Mollenhauer, and H. Tschöke, *Handbook of diesel engines*. Springer Science & Business Media, 2010.

CONCLUSIONS

This thesis presents the results of a numerical and experimental investigation of different prototype hollow cone nozzles for diesel injectors in terms of engine performance, emissions, and spray structure. The main peculiarity of the employed HCN injectors is the higher fuel injection pressure in comparison to the conventional hollow cone injectors for gasoline direct injection applications. The tests were conducted in a constant-volume pressurized vessel and on a single-cylinder compression ignition engine. In particular, the tested outwardly opening pintle type nozzles are characterized by:

- HCN, it can generate a hollow cone spray,
- HCN-J has five guiding walls on the pintle, and they have been added to generate both the conical liquid sheet and five compact jets.
- HCN-8J has eight guiding walls on the pintle and they have been added to generate both the conical liquid sheet and eight compact jets.

A comparison is made with the conventional MHN injector. The main results are presented and listed in two sections.

Hollow-Cone Diesel Spray Characterization

The spray behavior of an outwardly opening piezo injector over a broad range of injections and ambient conditions was investigated by imaging methods using Mie scattering and Schlieren techniques. The tests were conducted injecting n-heptane in a heated constant-volume pressurized vessel with high injection pressures, in engine-like conditions.

The high-pressure hollow cone nozzles were evaluated under evaporative and non-evaporative conditions to assess the spatial-temporal evolution of the global spray morphology as well as of the liquid and vapor phases. The combined optical technique was well suitable to capture the peculiarities of the diverse thermodynamic phases of the fuel and was sensitive to the governing parameters (ambient temperature and injection conditions). Even though the geometry of the injectors differs completely from the classical diesel multi-hole nozzle. The shape of the penetration curves showed

that the physical processes seem to be quite similar with a primary and a secondary breakup mechanisms that break up the liquid core exiting to the nozzle into ligaments, blobs, and final droplets, but both guarantee a slightly higher penetration compared to the MHN, except for the first HCN (old version) prototype characterized by a lower cone angle compared to the classical diesel one. The direct-drive piezoelectric system allows accurate control of the needle lift even if the needle closure still has bounce problems, in particular when the nozzle is clean, i.e., it has no carbon residue on the pintle.

An exhaustive experimental and numerical campaign, both hydraulic and optical, was conducted with HCN injectors. The optical analysis showed a high spray evaporation rate; this aspect will be better highlighted in the engine analysis, which is not a symptom of combustion optimization. Concerning hydraulic characterization by Bosch tube meter, a high flow rate with small needle lift and reduced hydraulic delay, compared to MHN, are the main characteristics highlighted. The injection rate curves show a quite linear increment with respect to time and a well-scaled behavior with injection pressure. The small error bars denote a stable and repetitive behavior of the injection system for a range of injected fuel mass from 5.0 to 80.0 mm^3/stroke. A non-perfect pintle closure was observed and confirmed through optical analysis. It causes an increase in PM emissions, found in engine analysis.

Further optical analysis in non-evaporating conditions using only the Mie-scattering technique was carried out for all the prototypes considered. This analysis allowed us to evaluate the charging voltage effect on the spray penetration and shape. A different charging voltage, in particular for HCN-J, causes a significant variation for the jets' shape. A lower voltage determines a lower needle lift and therefore a reduction of the spray penetration. Finally, an analysis of the nozzle deterioration effect, due to carbon residues on the pintle, was evaluated for HCN-8J. Fouling of the injector improves the performance of the injector. This soot allows for reducing the rebound effect in the closing phase.

Undoubtedly, the hybrid versions of HCN (HCN-J and HCN-8J), have reached quite similar performance to those of the MHN, but there are still problems in the closing phase, as previously discussed. Indeed, the activity on the engine allowed to characterize the prototypes better, and therefore verify the performance to the conventional injector.

The numerical investigation has permitted to describe the rapid breakup process immediately after the fuel discharge with a final circumferentially finely atomized spray for the HCN injector. Nevertheless, the acceptable agreement between numerical

and experimental results has permitted to assess the HCN spray behavior in a combustion chamber.

Engine characterization

The experimental activities were carried out on a prototype single-cylinder CI engine. In particular, the injector behavior and the engine response in terms of performance and emissions were analyzed and compared with the conventional multi-hole injector, considered the reference of the technology state of the art.

This study presents the results of two different prototype hollow cone nozzle diesel injectors on engine performance, emissions, and spray and flame structure. A preliminary parametric analysis on nozzle tip protrusion, charging voltage, and current injection profile is assessed for the nozzle type characterized by five compact jets and a circular area, HCN-J. Subsequently, a secondary parametrization was performed in terms of the start of injection (only for HCN-J) and rail pressure for two-hybrid nozzles (HCN-J and HCN-8J) adopting the same washer thickness and injector command. The analysis, for both parametrizations and injectors, concerns the combustion process, emission formation, and engine performance.

From the preliminary study on HCN-J emerges that the washer thickness influences the ISFC, then the washer thickness value of 2 mm minimizes the soot and ISFC. The highest injector command opening current value (8 A) of the nozzle needle lowers the smoke and ISFC values of about 25 % and 2.7 %, respectively, compared to the lower current value (2A). The highest tested charging voltage (HV 150), correspondent to the highest needle lift, produces a high level of soot.

Through the p_{rail} sweep, it has been observed for this type of injectors that the injection pressure increase keeps going a strong influence on PM emissions, similar to MHN. Therefore, this implies that operating with high injection pressures would allow reaching PM emission levels comparable to the conventional one. In general, the results for both nozzles show a tendency to shift the combustion mode towards diffusive combustion compared to the multi-hole combustion system, and, in some operating points, it has also been observed a longer combustion duration, getting worse the thermodynamic efficiency. The longer combustion duration is due to a slower air-fuel mixing as demonstrated by optical images. Indeed, through the optical engine, a different flame distribution compared to the conventional one has been observed. These are located close to the nozzle, due to the presence of the crown spray and near the chamber wall. The SOI sweep did not lead to any advantage in terms of emissions and performance.

In terms of emissions, the HCN injectors showed an increase in PM due to the poor air-fuel mixing and also high values of THC and CO emissions, attributable again to the increase of the combustion duration. At the same time, the combustion temperatures were generally lower with a lower NOx production rate.

For the sake of completeness, the results of the first prototype (HCN-old version) are presented.

The HCN-old version injector exhibits worse performance in terms of emissions and efficiencies. Higher levels of soot have been observed for higher needle lifts, likely due to the lower fuel atomization. In particular, the soot output is a combination of the presence of bigger fuel droplets and the more prolonged soot oxidation phase. The results suggest that the soot production process is more prominent than the oxidation phase.

Based on the results obtained, the newest version of the HCN injector does not yet guarantee the performance of the conventional one. Therefore, there is still room for further improvements. The worse results are mainly linked to the non-optimal exploitation of HCN spray characteristics. Indeed, they have been tested in a combustion chamber adequately designed for a conventional MHN spray. For this scope, an adequately designed numerical and experimental campaign, aimed to optimize the combustion chamber, is needed. However, the latest version of HCN (8 jets) still under investigation, based on the results of the previous injector, has the potential to provide better results. Indeed, in some operating key points, positive effects on combustion and emissions, by increasing the number of jets, have been observed.